UNIVERSITY OF CALIFORNIA, MERCED

Understanding the Microstructure and Interaction Between Nanoparticles and Polymers Through the Study of Precursor Complex Fluid in a PEMFC

A dissertation submitted in partial satisfaction of the requirements
for the degree of Doctor of Philosophy

in

Environmental Systems

by

Shirin Mehrazi

Committee in charge:

Professor Po-Ya Abel Chuang, Advisor
Professor Gerardo C. Diaz
Professor Sarah Kurtz
Professor Min-Hwan Lee

2022

This dissertation of Shirin Mehrazi is approved, and it is acceptable in quality and form for publication on microfilm and electronically:

Po-Ya Abel Chuang, Advisor Date

Gerardo C. Diaz Date

Sarah Kurtz Date

Min-Hwan Lee Date

University of California, Merced

2022

To

My parents, my sister and my beloved husband for their enduring support.

ACKNOWLEDGEMENTS

Many thanks to my advisor Professor Po-Ya Abel Chuang, for giving me the opportunity to start my journey in fuel cell materials research. I appreciate his support, suggestions, and mentorship.

I would like to express my appreciation to the department of Environmental Systems for awarding me several fellowships to support my education and research. Also, the Philippine-California Advanced Research Institutes (PCARI) for supporting our research projects.

I would like to thank my former and current committee members, Prof. Martha Conklin, Prof. Yue Wang, Prof. Sarah Kurtz, Prof. Min Hwan Lee, and Prof. Gerardo Diaz, for all their support and constructive suggestions.

I would like to thank my incredibly supportive labmates and friends who helped me through this journey. Great thanks to Mrittunjoy Sarker for his contribution to this study. Thank to Felipe Mojica, Dr. Nitul Kataki, Dr. Marc Labata, and Dr. Donglei Yang for their support and friendship. I want to thank our collaborator Philip Rolfe from NETZSCH corporation.

Last but not least, I want to express my profound appreciation to my beloved husband, Dr. Taymaz Homayouni, for his support, love, and contribution to my work.

ABSTRACT

Limited resources of fossil fuels and climate change left human beings with no choice but to seek alternate clean energy providers. Green hydrogen is one of the strong candidates toward electrification. Proton exchange membrane fuel cell (PEMFC) is a device that converts chemical energy stored in hydrogen to electricity with water and heat as the only byproducts. PEMFC is a multi-component system with all kinds of mass, heat, electron, and ion transport physics included in its operation. Diffusion through porous media, mainly when liquid water is generated at high current densities, is challenging. A porous carbon-based gas diffusion media (GDM) is in charge of reactant transfer to the catalyst layer to fulfill electrochemical reactions and electron generation. Precise control of the heterogeneous microstructure of the porous media is one of the major materials engineering challenges to enhance mass transport in the fuel cell. Two porous components in PEMFC with the most heterogeneous microstructures are built upon assembly of carbon or catalyst supported on carbon agglomerates. These components are the micro-porous layer (MPL) in the diffusion media and the catalyst layer. MPL and catalyst layers are fabricated by deposition of a thin film of their precursor slurry (ink), which is a complex fluid. Significant interactions occurring during the formulation, mixing, and deposition of the precursor materials dictate the final properties and microstructure of the porous structure. Regarding the catalyst layer, optimization of the microstructure through ink materials engineering could lead to more catalyst utilization. Hence, a lower amount of precious platinum (catalyst) is needed to reach a particular performance in the PEMFC. This study employs a bottom-up approach to study the microstructure of the carbon network formed in ink as a function formulation and its evolution during the high shear deposition process. Finally, the findings are correlated to the in-situ fuel cell performance and oxygen transport resistance of the components in the PEMFC. For MPL, optimum formulation parameters and novel porous media using additives are introduced. A new approach is used to elucidate interparticle interactions in catalyst ink from the simultaneous response of the structure to mechanical shear forces and small alternating current (AC) perturbation.

TABLE OF CONTENTS

LIST OF FIGURES

LIST OF TABLES

LIST OF ACRONYMS

AB	Acetylene black
BET	Brunauer–Emmett–Teller
CL	Catalyst layer
CNF	Carbon nanofiber
CNT	Carbon nanotube
CPE	Constant phase element
CV	Cyclic voltammetry
DLS	Dynamic light scattering
ECSA	Electrochemical active surface area
EIS	Electrochemical impedance spectroscopy
GDM	Gas diffusion media
GNP	Graphene nanoplatelet
HFR	High frequency resistance
HOR	Hydrogen oxidation reaction
I/C	Ionomer to carbon ratio
LVER	Linear viscoelastic region
MEA	Membrane electrode assembly
MPL	Microporous layer
MPS	Macroporous substrate
MWCNT	Multiwall carbon nanotube
ORR	Oxygen reduction reaction
OTR	Oxygen transport resistance
PDI	Polydispersity index
PEMFC	Proton exchange membrane Fuel Cell
Pt	Platinum
Pt/C	Platinum supported by carbon
PTFE	Polytetrafluoroethylene
RH	Relative humidity
SEM	Secondary electron microscopy
TEM	Transmission electron microscopy
TPB	Triple phase boundary

Chapter 1

INTRODUCTION

Transportation section accounts for 27% of the total greenhouse gas emission in the US [1]. By moving toward sustainable clean energy-supplied society, there is a need for the internal combustion engine (ICE) and fossil fuel to be replaced with zero-emission technology. Hence, lithium-ion batteries are successfully employed in light-duty vehicles. However, due to the low gravimetric energy density, Li-ion batteries cannot support the long-range power supply of heavy-duty vehicles. 20% of transportation emission is produced by medium and heavy-duty vehicles, while they account for less than 5% of the total vehicles on the road [2]. The growing hydrogen economy is a key solution to address long-range scaled-up transportation challenges by means of hydrogen-powered fuel cells with high energy per mass. Unlike batteries and similar to the conventional ICE vehicles, energy storage and generation units are separated in fuel cell cars. This feature provides the advantage of size and range adaption as well as fast refueling. The proposed technology for fuel cell electric vehicles (FCEV) is supported by proton exchange membrane fuel cell (PEMFC). The current dissertation is aimed to address critical material related operational challenges that hinder PEMFC from vast commercialization.

1.1 Proton exchange membrane fuel cell

PEMFC is a device that converts chemical energy stored in hydrogen to electricity via electrochemical reactions, with water and heat as the only byproducts. General working principle of PEMFC is shown in Figure 1.1. Hydrogen enters the cell from anode inlet and splits into proton (H^+) and electron (e^-) via hydrogen oxidation reaction (HOR, Equation 1.1). Proton and electron are transported from anode to cathode through the membrane and an external circuit, respectively. On the cathode side, oxygen enters the cell and participates in the oxygen reduction reaction (ORR, Equation 1.2) to finish the cycle and generate heat and water. The net reaction is shown in Equation 1.3.

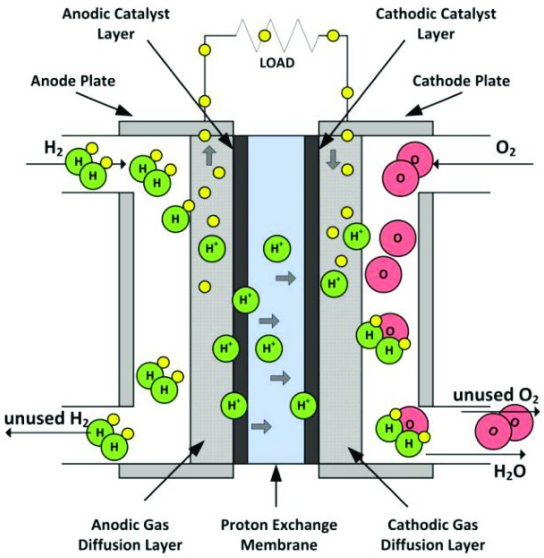

Figure 1.1: Schematic drawing of PEMFC working principle[3].

$$\mathrm{H_2(g)} \longrightarrow 2\,\mathrm{H^+} + 2\,\mathrm{e^-}\,,\mathrm{HOR} \tag{1.1}$$

$$\frac{1}{2}\,\mathrm{O_2(g)} + 2\,\mathrm{H^+} + 2\,\mathrm{e^-} \longrightarrow \mathrm{H_2O(l)}, \mathrm{ORR} \tag{1.2}$$

$$\mathrm{H_2\,(g)} + \frac{1}{2}\,\mathrm{O_2\,(g)} \longrightarrow \mathrm{H_2O\,(l)}, \mathrm{Net\ reaction} \tag{1.3}$$

PEMFC is composed of several components sandwiched together to provide operation requirements, which are mass, heat, and electron transfer. Detailed structure of PEMFC is shown in Figure 1.2. Anode and cathode components are symmetrical with respect to a proton exchange membrane at the center. Next to the membrane on each side, there is a catalyst layer followed by gas diffusion media (GDM), and flow fields. Both catalyst layer and GDM have porous carbon-based structures to regulate mass transport in PEMFC. The ultimate goal of a PEMFC is to generate high current with low voltage loss penalty. In order to achieve this goal optimization of the porous structure (catalyst layer and GDM) in the fuel cell have been one of the main research targets and focus of this dissertation.

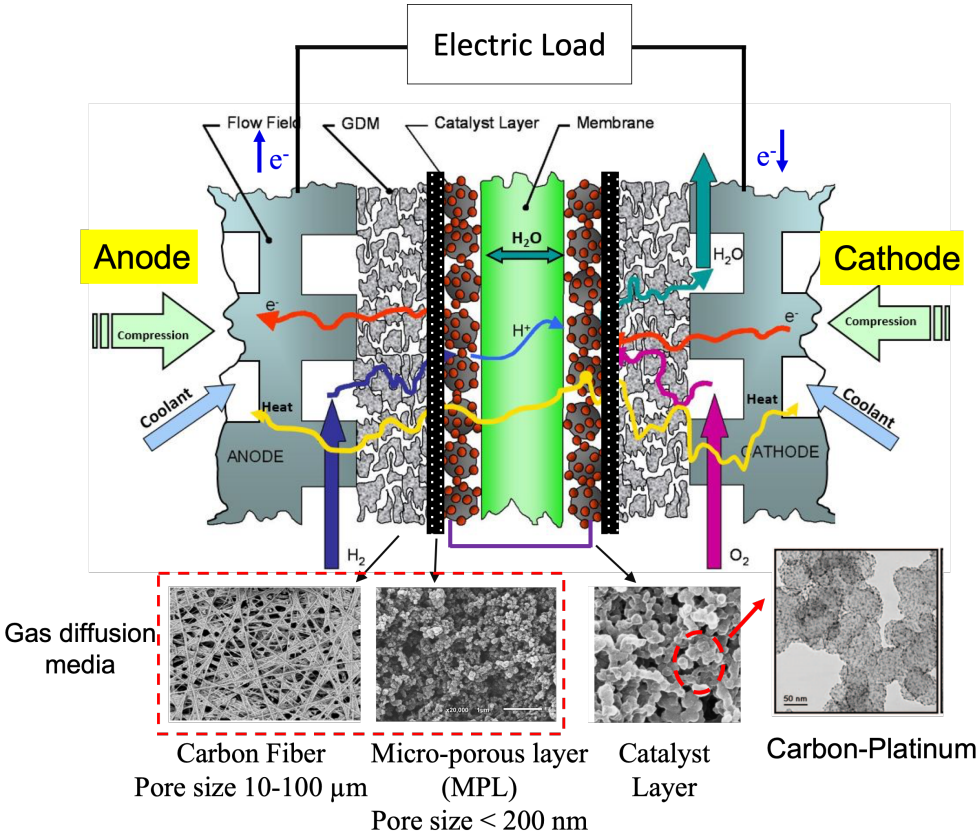

Figure 1.2: Detailed schematic of proton exchange membrane fuel cell components. Figure is generated from references [4–6].

1.2 Porous structure in the PEMFC

1.2.1 Gas diffusion media

Gas diffusion media has a double layer structure where a fibrous macroporous substrate (MPS) is coated by a carbon-based microporous layer (MPL). GDM's main functions are: 1) Diffusive transport of reactant gas to the catalyst layer, 2) discharge of the excess water, 3) mechanical support against compression force from cell assembly, and 4) heat and electron conduction. One of the main obstacles in the way of high power generation by the fuel cell is cell flooding due to water accumulation in the catalyst layer and diffusion media, which hinders reactant gas supply and available electrochemically active surface area. Enhancement of GDM mass transport management requires a fundamental understanding of its microstructure's morphology and physical properties, which are governed by its material and design parameters [7, 8]. MPS has large pore size (10-100 μm) [9] , which results in low capillary pressure (Equation 1.4) and water can easily accumulates in the pores. Thus MPL with an intermediate pore size (50-200 nm)[10] is implemented between catalyst layer

(pore size < 50 nm) and MPS to improve water management[11–14]. Capillary pressure is calculated using Young–Laplace equation (Eq.1.4), where P_c is the capillary force, γ is liquid gas surface tension, θ is the contact angle ($> 90^{\circ}$ for hydrophobic surfaces), and r is the pore radius.

$$P_c = -\frac{2\gamma Cos(\Theta)}{r} \tag{1.4}$$

Both MPS and MPL are wet-proofed to some degree by using polytetrafluoroethylene (PTFE) impregnation. Research on material and design improvement of MPS is advanced, and several reliable commercial products are available. Hence, MPL optimization is a key to improving the overall GDM's water management. Heterogeneous microstructure of MPL regulates water by limiting its intrusion into specific locations at the MPL-CL interface while keeping the rest of the pores open for gas transport [11, 15]. Other functions of the MPL include: 1) providing support to the membrane and catalyst layer [16], 2) preventing catalyst penetration into the MPS macropores for catalyst coated diffusion media [17], 3) protecting the membrane from the carbon fibers in the MPS, and 4) decreasing electrical and thermal contact resistance between the catalyst layer and MPS [18]. MPL properties such as porosity, pore size distribution, hydrophobicity/hydrophilicity, and thickness have been optimization targets to address water management in this layer. Most of these properties stem from the material and formulation of the MPL ink, a complex fluid composed of carbon black, PTFE, and solvent. Assembly of agglomerates formed in the MPL ink and their shrinkage determines pore morphology of MPL [19]. Ink deposition methods, including coating, spraying, and screen printing [20] apply high shear forces to the agglomerates, which can affect the state of structure percolation in the final MPL. Further, carbon agglomerates in the MPL ink can be less than 1 micron and penetrate through the macro pores of MPS to form a transitional layer. The depth and amount of MPL penetration, which is a function of the MPL carbon type, hydrophobic agent, ink flow properties, and manufacturing process, has a significant effect on the transport properties of the GDM [7]. Both MPLs agglomerate size and its ability to penetrate the MPS can drastically affect mass transport properties of the GDM. Kinetics of aggregation, which is mainly driven by ink materials and mixing method, can be quantified through the study of flow properties of matter or rheology. Further, ink formulation variables like the total solid content or PTFE loading need to be optimized through a systematic understanding of the influence of these parameters on the kinetics of aggregation.

1.2.2 Catalyst layer

Membrane electrode assembly (MEA) is attributed to the combination of the anode and cathode catalyst layer with a membrane in between. MEA is the heart of the PEMFC, where all electrochemical reactions take place. Similar to the MPL, the catalyst layer is fabricated through ink casting. Agglomerates of platinum-carbon (Pt/C, catalyst) covered by a proton conductive polymer (ionomer) are the catalyst ink's main components, forming the catalyst layer. Catalyst itself is a powder of nano size (2-5 nm) platinum (Pt) distributed on the carbon surface (70 nm particles). High cost of Pt is known as one of the major barriers to fuel cell commercialization [21]. Among the two reactions that occur in PEMFC, HOR and ORR (Equations 1.1 & 1.2), ORR has the slowest kinetics, which requires more catalyst to retain acceptable performance [22, 23]. One approach to reducing electrode cost is to understand and optimize microstructure of the catalyst layer such that maximum platinum usage and low mass transport resistance are gained. In that case, high performance can be achieved by low loading of catalyst. It is essential to express that not all the catalysts utilized in ink and the final catalyst layer will be available for electrochemical reactions. Electrochemical reactions take place only in specific locations where three pathways of electron, proton, and gas transport are available. These locations are named triple phase boundary (TPB, Figure 1.3).The electronic conductivity is provided by the agglomerated network of carbon support as well as Pt. A layer of ionomer, in contact with Pt, provides the proton (H^+) conductivity. Reactant supply is through the porous microstructure of the catalyst layer.

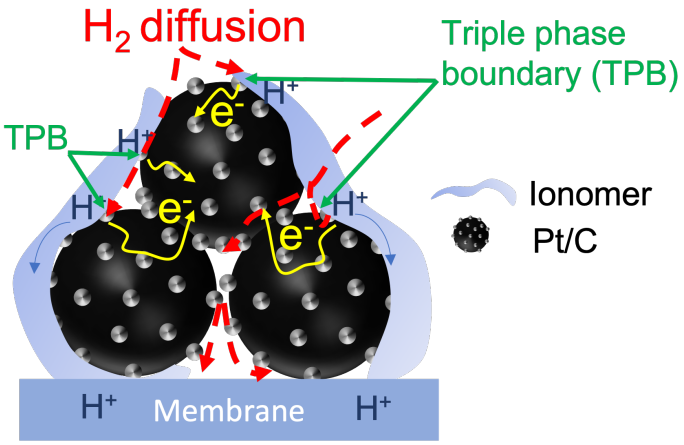

Figure 1.3: Schematic drawing of the triple phase boundary, where three pathways of proton, electron, and gas transport are available.

In order to tune up catalyst layer microstructure, a fundamental understanding of the interactions between its constituent material is required [24–26]. Most important interactions such as catalyst agglomerate formation, ionomer-Pt, and ionomer-carbon interactions take

place in catalyst ink formulation and processing all the way to its casting as a thin film [27, 28]. Formulation participating factors in the formation of ink's microstructure are: 1) solvent formulation, 4) total solid content, 5) carbon/solvent weight ratio, and 6) ionomer/carbon weight ratio. The most common solvents used in catalyst ink formulation are water, isopropyl alcohol, and n-propanol (NPA), which in most cases, a mixture of water and alcohol is used. Catalyst and ionomer have different interactions and conformation in water-rich versus alcohol rich solvents [29–32]. Ionomer is a polymer with a hydrophobic PTFE backbone and side chains of hydrophilic sulfonic acid [33], which can get various conformations in water-rich versus alcohol-rich solvents. Carbon support of catalyst is hydrophobic and can be dispersed to smaller agglomerate sizes in alcohol rich environment. On the other hand, ionomer tends to interact with carbon support from its hydrophobic backbone and the solvent through its hydrophilic tails. Besides solvent formulation, the total amounts of solid particles (Ionomer + Pt/C) in the solvent greatly impact the kinetics and state of agglomerate formation. Most of the catalyst aggregation is due to the attractive forces among carbon particles that can managed by the dispersing ability of solvent and the carbon concentration. At last, ionomer/carbon ratio was found to be one of the most impactful interactions that affects both the ionomer and Pt/C network in the ink as well as mass transport, proton conductivity, and performance of the catalyst layer in the fuel cell. Thus, it can be inferred that reaching an optimum condition where small coherent agglomerates of Pt/C, surrounded by a uniform and yet not a thick layer of ionomer coverage, is challenging. On top of all the ink formulation complexity, the shear forces from the coating process should be considered in determining the final microstructure of the thin film.

1.3 Scope of research

Two of the most critical components in a PEMFC, microporous layer and catalyst layer, have heterogeneous microstructure built upon assembly of carbon-based agglomerates. Oxygen transport resistance in the cell is induced by either the porous structure itself or water accumulation in the pores. An increase in mass transport resistance hinders high current density generation of the cell due to the lack of reactant supply. Thus, engineering the heterogeneous porous structure in PEMFC is of great importance. Since most of the agglomerate and microstructure formation occurs in the precursor ink, formulation variables can be the key to designing optimum catalyst and microporous layers. Regarding MPL, the main goal of the microstructure is to minimize oxygen transport resistance, especially under highly humidified conditions. On the other hand, understanding and engineering the catalyst layer microstructure is much more complicated than the MPL due to its multi-functional properties to enhance gas, liquid, electron, and ion transport. Thus, interparticle interactions

in the catalyst ink not only can affect the porous structure but also the available reactive sites and charge transport. For instance, thick ionomer coverage on the catalyst agglomerates can significantly affect the local mass transport resistance and catalyst activity. We hypothesize that an excess amount of ionomer can interfere with the formation of the interconnected carbon network and increase local electron transport, consequently reducing available triple phase boundaries. Fortunately, any change in the formulation of the precursor material reflects in its flow properties. Therefore, we employed a rheological study of suspensions to deconvolute microstructure properties of the catalyst layer and MPL as a function of their precursor ink formulation and applied shear forces from coating process. Since fuel cell is a multi-component system, understanding microstructural properties of the MPL and catalyst layer requires a bottom-up investigation from ink properties to the product performance in the cell and its oxygen transport resistance. Hence, the findings of three main projects are presented in this dissertation, focusing on microstructural understanding and optimization of the MPL and catalyst layer.

The first project is a fundamental study to understand the impact of MPL ink formulation parameters on the state of aggregation and final properties of the fabricated GDM. As mentioned, solid particles in MPL ink are carbon nanopowder and PTFE. Two formulation variables, ink total solid content and PTFE loading, were studied for the impact on the state of agglomeration in the MPL. The study aims to 1) introduce flow properties as reliable ex-situ characterization for microstructural analysis of complex fluids and 2) find the optimum formulation of the MPL in terms of solid content and PTFE loading to achieve the lowest mass transport resistance in PEMFC.

In the second project, formulation of the optimum MPL identified in the first project was even more enhanced in terms of mass transport properties. Carbonaceous additives with a high aspect ratio were employed to introduce pore size gradient to the MPL. The idea is that by adding multiwall carbon nanotube or graphene particles to the regular spherical carbon black, pore sizes in the range from macro to nano would form. The nanopores formed by agglomerates of carbon black would enforce high capillary pressure, so water cannot intrude. On the other hand, large pores created by the additives result in low capillary pressure, which turns them into potential preferential water pathways. It is imperative for the diffusion media to separate water and gas transport pathways such that oxygen can diffuse easily and reach the catalyst layer.

The third project is focused on catalyst ink microstructure and study of the fabricated MEAs in the fuel cell. For the first time, a new in-house setup was designed to enable simultaneous rheological analysis and electrochemical impedance spectroscopy of the catalyst ink as indicators of the state of aggregation and ionomer coverage. Ionomer-Pt-carbon

interaction is one of the most complicated interplays among catalyst ink components, and it is still not well understood. Typically carbon particles tend to attract each other and form agglomerates. However, when a layer of ionomer either fully or partially covers particles, the attractive force is replaced by a repulsive force, and less interconnected agglomerates will form. If the ionomer coverage gets thick or ionomer covers all catalyst particles in the extreme case, no carbon network can form, which reduces the available triple phase boundary. With the new methodology, named "Rheo-Impedance analysis", coherency of the carbon network can be evaluated through its conductivity and response to the applied shear forces. Hence, catalyst inks with various ionomer/carbon ratios were prepared and studied with the new technique to get a direct signal of ionomer interference with Pt/C network assembly. MEAs of the studied inks were tested in the fuel cell to gain more information regarding the effect of ionomer coverage on oxygen transport resistance in the cell.

Chapter 2

LITERATURE REVIEW

For decades scientists have studied various catalyst and microporous layer precursor ink materials. However, recent studies showed the importance of formulation parameters and processing methods on the functionality of thin-film components of PEMFC. This chapter summarizes the research background on formulation and materials of the porous thin films in the PEMFC.

2.1 Catalyst and microporous layer fabrication

Fabrication of the porous thin films in the PEMFC includes three main steps: 1) Precursor ink mixing, 2) deposition on the substrate, and 3) Drying. Steps 1 and 2 involve high shear forces that alter the agglomerated structure formed in the as-made ink. In the case of diffusion media, the slurry is deposited on a porous substrate, which further penetrates it, and the whole assembly will form the gas diffusion media (Figure 2.1). For the catalyst layer deposition can be directly on the membrane via spray coating or in the case shown in Figure 2.2, it can be via ink deposition on a nonporous decal followed by its transfer to the membrane with a hot press. The former method is used in the current study, and the final MEA is shown in Figure 2.3. Carbon slurries used in electrode and microporous layer fabrication are counted as sol-gel material. Sol is attributed to the colloidal solution of the agglomerates in a solvent, and gel is the cross-linkage formed among particles during solvent removal [34]. Surface charges on the colloid surface inhibit sedimentation of particles as large as 1 μm [35]. Thus, the microstructure of the porous media forms in multiple stages such as: 1) Sol formation via dispersing solid components in the relevant solvent [34, 36], 2) sol deposition and evolution of the network formed in ink with response to the deposition shear force, and 3) linkage of clusters and gel formation [37, 38], and 4) gel shrinkage and structure solidification with solvent evaporation [39]. Understanding effect of formulation and processing variables on the final properties of the porous media in the PEMFC, requires tracking the microstructure from ink to deposition, drying, and finally, in situ fuel cell performance. In most ink studies, effect of external shear forces on the product's physical properties is overlooked. However, Hatzell et al. quantified the shear-thinning property of

the catalyst ink in a study of the ink's viscosity evolution as a function of the deposition method. For instance, viscosity of ink during spray coating drops to $\leq$0.5 Pa.s, 100-1000 Pa.s for blade coating, and 0.001-25 Pa.s for slot die coating [40].

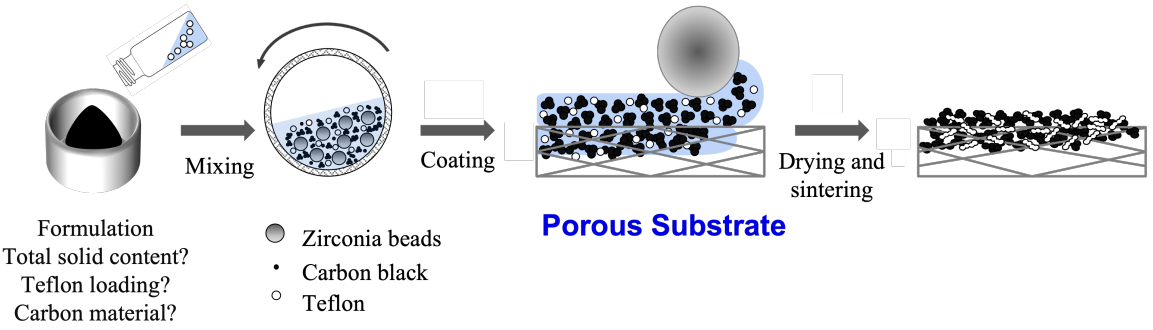

Figure 2.1: Schematic of the microporous layer fabrication using a carbon fiber porous substrate.

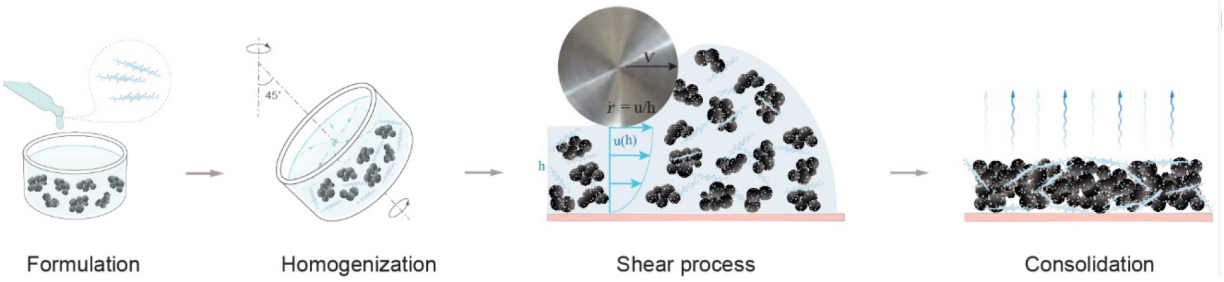

Figure 2.2: Schematic of the catalyst ink fabrication and casting on a non porous decal (image obtained from reference [41]).

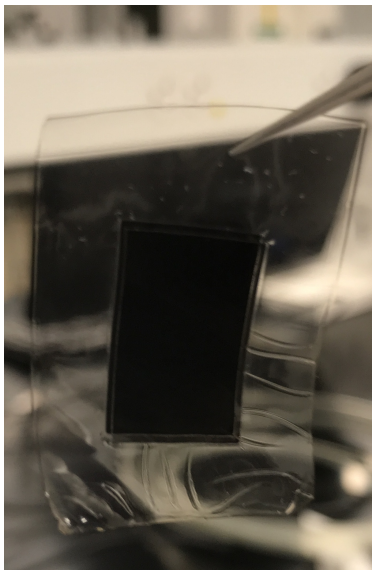

Figure 2.3: Membrane electrode assembly prepared by decal transfer of the catalyst layer coated on the nonporous decal.

2.2 Structure evaluation of the microporous layer

Standard MPL consists of a mixture of carbon powder and PTFE to provide electrical and thermal conduction paths as well as gas and liquid transport paths. The fine hydrophobic pores in the MPL have high water capillary pressure, which prevents liquid water in the MPS from flooding the catalyst layer [11, 15]. Due to the complexity of the multi-stage processing steps and ill-defined desirable properties, there is a lack of fundamental understanding of the MPL design criteria. To investigate the MPL properties and enhance its water management ability, most efforts have been devoted to its ink formulation, and material composition [42]. The majority of the MPL studies focused on the type of carbon black [43–45], carbon loading [13, 46], PTFE content [13], and the use of additives like pore formers [47] and hydrophilic agents [48, 49]. Among the various carbon materials investigated, Acetylene Black (AB) has been most widely used due to the small pore size and high pore volume provided by its low surface area ($80 m^2/g$) [43, 44]. Additionally, Wang et al. [45] proposed that an optimal MPL microstructure should include a range of micro, meso and macro-pores, which can be obtained by adding carbon black with different surface areas. Besides material composition, different levels of PTFE content in the MPL ranging between 10 and 40 wt.% have also been studied in the literature [12, 49–51]. Besides the choice of materials and porosity, another important and yet challenging design parameter of the MPL is its thickness [52, 53]. The MPL thickness is tough to measure accurately because of the high surface roughness of the carbon fiber topography. In addition, the MPL ink can penetrate into the MPS porous substrate and form a transition region. Therefore, the MPL thickness is also governed by

the MPS pore size and the MPL ink flow properties [49]. Spernjak et al. [48] employed micro x-ray computer tomography and found that around 50% of the total MPL thickness falls within the penetrated transition region. However, this observation was not coupled with ink flow properties and cannot be generalized to all MPL ink compositions.

As mentioned previously, deposition of carbon slurries on a substrate is a shear-induced process. Due to its viscoelastic properties, the MPL ink is prone to microstructural deformation as a result of the applied shear force [54, 55]. Hence, MPL properties such as pore morphology, thickness, and coating quality are influenced by the flow properties, and shear-history of the ink [56, 57]. Moreover, the agglomerate microstructure is a function of the interparticle and solid-liquid interactions within the ink [27, 57], which may continue to evolve during and after fabrication steps [58]. Thus, the state of agglomeration and particle rearrangement after the application of shear force could vary with the ink material, solid/liquid, and solid/solid volume ratios. A few studies attempted to quantify the flow characteristics of the MPL ink through steady shear viscometry. Stampino et al. [59] proposed that, at a constant carbon/Water ratio, increasing the PTFE content of the ink does not affect the viscosity of the ink at high shear rates. Latorrata et al. [60] investigated the properties of MPL fabricated with various fluorinated polymers and measured their viscosity to yield similar MPL thickness for all samples. Their results revealed a higher viscosity for the inks made with PFPE, FEP, and PFA compared to the one made with PTFE. Since the agglomeration in ink is a dynamic behavior, steady state results provide limited information about the correlation between an MPL ink formulation and its flow properties, which in turn hinders optimization of the MPL.

Based on the literature, MPL materials and microstructure significantly affect fuel cell performance. However, the current understanding is mostly based on empirical methods correlating the MPL ink formulation with fuel cell performance. In addition, ex-situ characterization, such as porosimetry and gas permeability, are typically performed on the entire GDM, which is dominated by the MPS [7]. These ex-situ methods do not directly measure the MPL properties or evidence of MPL effectiveness in enhancing water management capability. Therefore, there is a lack of understanding of the connection between the MPL ink properties and the final pore structure of the MPL that governs the transport properties. In the literature, Cryo-SEM images of the carbon inks showed that the agglomerate microstructure highly resembles the morphology in the dried film [27].

2.3 Pore modifications in the microporous layer

Various studies are devoted to the porosity and pore size evaluation of the MPL. Graded porosity is found to be beneficial for water and gas transport regulation [61, 62]. For

instance, pore formers [47], carbon additives of various surface areas [45] and particle sizes such as thermal expandable graphite [63], carbon nanotubes (CNT), and carbon nanofibers have been introduced to the conventional carbon black-based MPL [64–66]. Recently, carbon nanotubes and graphene gained attention as potential MPL materials due to their higher electrical and thermal conductivity as well as mechanical stiffness compared to carbon black [67–69]. Ohmic performance enhancement was observed in an MPL with 10 wt% CNT, and an FEP binder [70]. Some studies focused on higher air permeability as well as larger mean pore size of MPLs containing vapor-grown CNT and carbon nanofiber (CNF) [67, 71, 72]. Lee et al. [66] observed lower mass transport resistance for multiwall CNT (MWCNT) composite MPL compared to a commercial diffusion media. While some researchers reported higher porosity of the CNT containing MPLs, others found that the main impact of this additive is an increase in the mean pore size while the total porosity remains constant[65, 73]. Lin et al. [73] studied effect of various CNT weight ratios in the MPL with the maximum of 15 wt% CNT. It was found that the effect of carbon black type is more significant than the additive content. It should be noted that the fuel cell performance was only evaluated at the maximum relative humidity of 75%. Surface-modified CNTs like hydrophilic [48, 74, 75], and nitrogen-doped CNTs [76] have been proposed as potential additives that can enhance water transport in the diffusion media. In the work of Kitahara et al., the optimum amount of a hydrophilic MWCNT was reported as 4 wt%. Spernjak et al. [48] employed neutron radiography and in situ nano X-ray computed tomography to prove the existence of preferential water pathways and less flooding in the MPLs with hydrophilic MWCNT additive.

Few studies have focused on graphene-based MPLs. Leeuwner et al. [77] incorporated a graphene foam without any hydrophobic agent as the MPL to reduce contact resistance. However, the lack of hydrophobicity resulted in higher mass transport resistance in this MPL compared to a commercial one. Pure graphene was used as MPL and provided a packed microstructure, improving electrical conductivity and performance under dry conditions [78]. Lab-made electrochemically exfoliated graphene was incorporated in the MPL by Najafi et al. [68] and resulted in higher water retention under dry conditions. In a study by Mriani et al., various particle sizes of graphene in composite with carbon black showed higher mass transport resistance at high relative humidity compared to MPL of pure carbon black [79]. Reduced graphene oxide, graphene, and their composite with carbon black were employed as MPL, resulting in lower ohmic resistance but higher mass transport resistance [80].

2.4 Catalyst layer microstructure

Main functions of the catalyst layer microstructure are 1- effective transport of proton from membrane to the catalyst surface, 2- reactant transport to the catalyst surface through the porous structure, 3- water management, 4- ability to provide electron-conductive network, and 5- establishment of the triple phase boundary. Micorstructure of the catalyst layer is built upon the assembly of catalyst-supported carbon primary particles (10-100 nm), aggregates (>100 nm), and agglomerates ($\sim$ 1μm) [57, 81]. These particles can stack up to form micro, meso and macro pores in the size range of <2 nm, 2-50 nm, and >50 nm, respectively [57]. Thus, it can provide mass transport pathway through its porous structure. Internal percolation of agglomerates, due to the attraction of carbon particles, provides electronic pathways. Finally, by introducing an ion conductive polymer to the catalyst, proton conductivity is feasible through a web-like coverage of it around catalyst particles [82–84]. Critical properties of the catalyst layer for optimal functioning are stemmed from its microstructure, which in turn is a function of the precursor material formulation, and coating processing [28, 85–87].

Four types of interactions occur during the formulation of catalyst ink that can impact all functions of the resulted catalyst layer. The interactions are between: 1- Pt/C | solvent , 2- Pt | ionomer, 3- carbon support | ionomer, 4- ionomer | solvent. It is reported in several studies that Pt/C can have different aggregation kinetics in different dispersing media [88]. Dispersion media of the catalyst ink has gained a lot of attention due to its impact on ink properties such as: agglomerate size distribution, viscosity, and drying rate, which all affect mass transport and physical properties of the catalyst layer [40, 83, 89]. In ink without ionomer, the carbon support of the catalyst tends to form smaller agglomerates in alcohol-rich solvents compared to water-rich. However, the interplay between ionomer, Pt/C, and solvent has not yet been clarified by the researchers. For instance, Balu et al. [90] reported that in a mixture of IPA- water as the dispersing media, decreasing alcohol results in dissociation of nafion followed by its thinner coverage around Pt/C agglomerates and consequently smaller agglomerate size. However, Takahashi et al. [27] had an opposite finding, where larger agglomerates and even agglomerates of free ionomer can form in water-rich solvents.

One of the most common ionomers used in the PEMFC industry is Perfluorosulfonic acid (PFSA), with a hydrophobic backbone and hydrophilic side chains. Ionomer-solvent and Ionomer- Pt/C interactions are the most challenging unknowns of the catalyst ink formulation. Several studies found dielectric constant of the solvent has the most impact on ionomer conformation, where ionomer precipitation, colloidal, and a complete solution is when the solvent dielectric is <3, between 3 and 10, and >10, respectively [91]. Small angle spectroscopy and cryogenic observations recorded rod-like configuration of ionomer in polar

solvent like water [92]. There is still discrepancy among findings on which configuration of ionomer can enhance both its proton conductivity and oxygen diffusivity within the catalyst layer microstructure[86, 91, 93]. Ionomer-Pt/C interaction is one the most important interactions in the ink since the electrochemical reactions occur at the ionomer-catalyst interface and oxygen diffusivity depends on the thickness of the ionomer coverage. Ionomer coverage was found to be non-uniform around the catalyst layer [27] with thickness variation in the range of 4-10 nm [25, 94]. Further, coexistence of free ionomer aggregates (rod-like, diameter=3 nm, length = 20nm) with Pt/C agglomerates have been reported [95, 96]. However, how free ionomer stack up with the rest of the structure is unknown. Ionomer to carbon ratio was known as the design criterion responsible for the interactions between Pt/C and ionomer. Low ionomer coverage reduces fuel cell performance by low proton conductivity, while a thick ionomer coverage blocks oxygen accessibility to the catalyst surface. Some studies reported ionomer loading in the range of 30-36% as an optimum amount to achieve high proton conductivity in the microstructure [97]. However, the optimum amount of ionomer can vary by type of carbon support (high surface area versus low surface area carbon black), testing condition, and catalyst loading [98]. Ionomer interaction with carbon support is via van der Waals forces, while it has much higher absorption on the platinum surface [99]. Multi-level interactions in the catalyst ink make distinguishing its properties from in situ fuel cell performance or ex-situ microscopy very challenging. Thus, a technique that can evaluate bulk responses of the catalyst ink microstructure as a function of formulation variables is needed.

2.5 Oxygen transport resistance in the porous media

Sluggish kinetics of the oxygen reduction reaction and lower effective diffusivity of oxygen compared to hydrogen, make diffusion in the cathode more problematic and critical than anode. Depending on the size of the gas molecule and available pore size, there exists two types of diffusion mechanisms: Fickian and Knudsen diffusion. If pore size is larger than the gas molecule (pore size > 50 μm), the only diffusion control parameter is an intermolecular collision. Therefore, concentration of the reactant can affect the Fickian diffusion. Knudsen diffusion is attributed to the diffusivity in pores with a smaller pore size (< 100 nm) than the gas molecule. In this case, molecule collision to the solid walls of the pore is the limiting factor. Thus, pore geometry can significantly impact Knudsen diffusion [100, 101]. In a PEMFC, Fickian diffusion is attributed to the large pores of the macroporous substrate in the GDM, while Knudsen diffusion occurs in small pores of the MPL, and catalyst layer. In the case of the catalyst layer there is a third diffusion barrier caused by its microstructure, which is oxygen diffusion within the ionomer. Three resistances are on the

way of this diffusion mechanism 1- diffusion in the void-ionomer interface, 2- diffusion inside the ionomer (not a porous material, and oxygen diffusion is via water molecules absorbed into the ionomer structure [102–104]), and 3- diffusion in the ionomer-catalyst interface [24, 105, 106]. On top of all of the diffusion mechanisms mentioned above, there is oxygen diffusivity in presence of liquid water in the porous media, which makes the overall diffusion even more challenging. Considering all oxygen transport resistances in the cell, achieving high fuel cell performance requires precise control of the hierarchy microstructure of the MPL and catalyst layer.

Chapter 3

OVERVIEW OF EXPERIMENTAL METHODES

This chapter contains information on the major characterization tools used in this study. Detailed testing conditions and other characterizations are provided in the relevant chapter of each study, in the experimental section.

3.1 Dynamic light scattering

Dynamic light scattering is a method to evaluate colloid particle size distribution, using diffusion coefficient of the particle under Brownian motion. The force applied from the surrounding solvent causes the Brownian motion in particles. Since MPL and catalyst inks are both colloids containing carbon-based agglomerates, this method can be used to get some information on the primary aggregate size formed as a result of ink formulation. The Stokes-Einstein equation (Equation 3.1) correlates particle diffusion coefficient in the solvent with the media temperature, particle size, and dispersion viscosity. In the following equation, d_H is the particle's hydrodynamic diameter, K is the Boltzmann's constant, T is the temperature, η is the dispersing media's viscosity, and D is the diffusion coefficient.

$$d_H = \frac{KT}{3\pi\eta D} \tag{3.1}$$

The instrument operation includes shedding a laser beam to the sample and detecting intensity of the scattered light due to the particle motion. The output of this measurement is a plot of intensity versus particle size. The higher the intensity, the more is the population of the respective particle size. In this study, the average particle size and broadness (polydispersity index (PDI)) of peaks in the intensity versus particle size plot are considered in data interpretation. PDI clarifies whether the particle size distribution is uniform, broad, or bimodal. PDI>1 is out of the measurement limits of the instrument, and DLS is not a proper characterization for such dispersion.

Concentration of the diluted inks for DLS measurement is reported in the experimental section of each chapter. Usually, dilution is to the point that large agglomerates with weak Van der Waals bonding may not exist. However, the primary aggregates will remain

intact due to the strong bonding. Thus, we can have a qualitative understanding of the effect of formulation on the primary aggregate size distribution in ink.

Besides aggregate size distribution, stability of the catalyst and MPL inks can be measured by DLS, using particle surface charge (Zeta potential). A dip cell with positive and negative electrodes is inserted into the solution. Particles' movement in a solvent and under the influence of an applied electric field is known as electrophoresis, which is a function of the electrode distance, dispersing medium viscosity, electric field strength, and zeta potential. Particle mobility in the presence of an electric field can be calculated via Equation 3.2, where U_E is the electrophoretic mobility, V_f particle velocity, d electrode distance, E applied voltage, ϵ dispersing media dielectric constant, Z zeta potential, f(Ka) Henry's constant, and η is the dispersing media viscosity. The greater the positive or negative zeta potential, the higher the dispersion stability.

$$U_E = \frac{V_f d}{E} = \frac{2\epsilon Z f(Ka)}{3\eta} \tag{3.2}$$

3.2 Rheology

Rheology is the science of material flow and is one of the essential properties of colloids like catalyst and MPL inks. Regarding the inks used in PEMFC thin film fabrication, resistance to flow comes from the carbonaceous network. Thus, rheological properties of the inks can be used as a guide on how the agglomerated microstructure forms as a function of ink formulation and shear forces from coating process. To perform rheological measurements, an ink sample was loaded between two parallel plate geometries (40mm in diameter) of a rotational rheometer (Netzsch). The desired gap should be a least ten times larger than the estimated largest particle in ink. In each chapter, the plate gap used in the study is mentioned. Four measurements have been performed, including viscosity, small amplitude oscillation test, three-phase rebuilt, and finally, a novel homemade setup is prepared to measure the electrical conductivity of the ink simultaneous to the rheological measurements. To measure viscosity, shear rate is controlled, and the corresponding shear stress is recorded. By dividing shear stress by shear rate, viscosity can be calculated and plotted versus shear rate. If sample's viscosity does not change with shear rate, its behavior is called Newtonian. However, if viscosity is either reduced or increased with increasing shear rate, sample is categorized as non-Newtonian fluid. MPL and catalyst inks are non-Newtonian shear-thinning fluids, so their viscosity reduces with increasing shear rate. The other characteristic of carbonaceous inks is the viscoelastic behavior, which includes both features of elastic behavior from the solid carbon network and viscous behavior from the dispersing media. Small amplitude oscillation test helps distinguish the elastic and viscous behavior. A small sinusoidal

displacement is applied so the carbon network is not disturbed and the resulted stress is measured, which due to the viscoelastic nature of the material, has a phase angle compared to the applied displacements. Elastic modulus is calculated via dividing shear stress by the applied shear strain, and is a property to evaluate the strength and compactness of the carbon network in the studied samples.

A three-step shear rate ramp up and down was performed to study ink's behavior under applied shear forces from the coating process. The test is known as three-phase rebuilt, and its goal is to compare ink microstructure as a casted thin film versus the as-made ink. Thus, impacts of processing on the ink can be evaluated.

3.3 Parallel rheological measurement and electrochemical impedance spectroscopy

Due to the complex nature of the interparticle interactions in the catalyst ink, rheology alone is insufficient to understand ink's microstructure as a function of formulation parameters and external shear forces. Thus, a homemade setup is designed to assess electrical conductivity of the ink as a function of its ionomer/carbon ratio. Ionomer coverage around Pt/C particles can affect the integrity of the carbon network, which can reflect in the ink conductivity. The new Technique is employed to understand ionomer-carbon-PT interactions. Details of the setup design and measurement criteria are provided in Chapter 6. Two types of Rheo-Impedance studies have been proposed: 1) simultaneous three-phase rebuilt and single frequency impedance measurements and 2) full frequency range impedance measurement before and after applying a high shear force to the sample.

3.4 Electron microscopy

Both secondary and transmission electron microscopy (SEM and TEM) were used to visualize porous media's structure and primary aggregate configuration, respectively. To observe cross-sectional microstructure of the fabricated MPL, diffusion media was freeze fractured in the liquid nitrogen. Zeiss Gemini was used for cross-section and surface SEM imaging. Cryogenic-TEM imaging of the primary aggregates in the catalyst ink has been performed in the liquid form by forming vitreous ice of the diluted ink on a TEM grid and in a Talos F200C G2 instrument.

3.5 Fuel cell tests

Fuel cell performance is usually reported as a plot of voltage versus the current density, and in this study is performed for both diffusion media and catalyst layer investigations. An assembly of MEA, diffusion media, straight-parallel channel flow field, and gold current collector was installed on a Greenlight G20 Fuel Cell Test Station. The testing protocol is

shown in Table 3.1. In this study, all the fabricated MPLs and catalyst layers are used on the cathode side due to the significant kinetics and mass transport limitations caused by the sluggish oxygen reduction reaction, water generation, and oxygen diffusivity. The characterizations include electrochemical active surface area measurement via cyclic voltammetry, electrochemical impedance spectroscopy to measure high-frequency resistance, polarization curve, and limiting current test. More detail is provided in each chapter for the relevant study.

Table 3.1: Fuel cell testing protocols.

Test	Temperature (°C)	RH (%)	Pressure(kPa abs.)	Flow rate(An/Ca) (NLPM)	Load control(V)	Step hold time(sec)
Break-in	70	100	50	10/10 (Stoich)	OCV-0.60	900
Dry limiting current	80	64	100, 150, 200, 300	0.40/2.0	0.30-0.09	130
Wet limiting current	70	80	300	0.40/2.0	0.30-0.09	130
Dry polarization	70	64	100	0.40/2.0	OCV-0.20	720
Wet polarization	70	100	300	0.40/2.0	OCV-0.20	720
RH-Sweep	80	40-100	100	0.40/2.0	0.30	600

3.6 Oxygen transport resistance measurement using limiting current test

In-situ limiting current experiments are performed for quantifying different oxygen transport properties from the channel to the electrode layer. Under limiting current conditions, the overall oxygen transport resistance (OTR), $R_{O_2}^{Total}$, is calculated using the Fick's law of diffusion and Faraday's law as following:

$$N_{O_2}^{''} = \frac{i_{lim}}{4F} = \frac{1}{RT} * \frac{P_{O_2}^{Channel}}{R_{O_2}^{Total}} \tag{3.3}$$

where $N_{O_2}^{''}$ is the through-plane oxygen molar flux in mol/cm^{2}sec, i_{lim} is the limiting current density in A/cm^2, F is the Faraday's constant, R is the universal gas constant in J/molK, T is the cell operating temperature in K, and $P_{O_2}^{Channel}$ is the channel oxygen partial pressure in kPa.

The oxygen partial pressure at the channel is controlled by the dry mole fractions of the oxygen, x_{O_2}, therefore the overall OTR can be expressed as:

$$R_{O_2}^{Total} = \frac{4F}{RT} * \frac{(P_T - RH * P_s)}{(i_{lim}/x_{O_2})} \tag{3.4}$$

where P_T is the cell operating pressure in kPa, P_S is the saturation pressure in kPa. A fuel cell can be assumed as a series circuit and the overall OTR can be broken down into different components of the circuit as following:

$$R_{O_2}^{Total} = R_{O_2}^{Channel} + R_{O_2}^{MPS} + R_{O_2}^{MPL} + R_{O_2}^{Electrode} \tag{3.5}$$

where the channel OTR, $R_{O_2}^{Channel}$, is coming from both inter-molecular diffusion and convection [107]. OTR in the gas diffusion layer, $R_{O_2}^{MPS}$, is pressure-dependent since Fickian or inter-molecular gas diffusion is dominant in the large pores (pore sizes greater than 50 µm) of the carbon fiber paper or gas diffusion layer [108]. OTR in the MPL, $R_{O_2}^{MPL}$, is governed by both Fick's diffusion in the larger pores and pressure-independent Knudsen diffusion in the smaller pores (pore sizes less than 50 nm) [109]. OTR in the catalyst layer, $R_{O_2}^{Electrode}$, can be occurred due to the pressure-independent diffusion through liquid water, ionomer, and porous electrode structure. The overall dry OTR can also be broken into pressure-dependent and pressure independent parts by running the cell under four different pressures. Limiting current experiments under wet conditions were also ran to quantify the overall OTR in the presence of liquid water.

Chapter 4

A RHEOLOGICAL APPROACH TO STUDYING PROCESS-INDUCED STRUCTURAL EVOLUTION OF THE MICROPOROUS LAYER IN A PROTON EXCHANGE MEMBRANE FUEL CELL

Dispersions of carbon black and polytetrafluoroethylene (PTFE) are precursors of the microporous layer, which serve as a component of the gas diffusion media in a proton exchange membrane fuel cell. To optimize the function of the microporous layer, it is essential to develop a fundamental understanding of its microstructure, which depends on the ink formulation and coating shear forces. Here, the relationship between the primary agglomerate structure in the ink and the morphological and surface properties of the dried layer is studied based on the rheological properties. The ink formulation variables in this study are the solid content (5, 10 and 15 wt.%) and the PTFE loading (15, 25 and 35 wt.%). The results indicate that samples with higher PTFE loading have a more inhomogeneous microstructure and form highly percolated agglomerates after coating. Most of the bulk flow properties of the inks are dominated by the carbon mass fraction and exhibit a power-law relationship as a function of the carbon mass fraction. The microporous layer with a solid content of 10 wt.% and a PTFE loading of 25 wt.% is found to have an optimal morphology for oxygen transport under both dry and wet conditions due to the fact that it is not overly flocculated and has a wide distribution of carbon agglomerates sizes. The findings from this study provide new insight into the optimization of microporous layer design and development.

4.1 Experimental

4.1.1 MPL ink preparation

The MPL ink used in this study consisted of Acetylene black, 60 wt.% PTFE suspension (DISP. 30, Chemours), water, and surfactant (Triton X-100). A fixed carbon to surfactant weight ratio of 13.5, determined empirically, was used for all of the ink studied in this work to ensure consistency. Water and surfactant were mixed to obtain a homogeneous solution followed by adding PTFE suspension and sonication for two minutes. Acetylene

black and the PTFE contained solvent were then added together in a ball milling container with zirconia beads of 5 millimeters in diameter. The solid components were dispersed in the liquid media using a centrifugal ball milling mixer (Thinky-AR100) at a rotation rate of 500 rpm for 10 minutes. The MPL formulations consist of three levels of solid content (5%, 10%, 15%) and three levels of PTFE loading w.r.t. the solid content (15%, 25%, and 35%) as listed in Table 4.1. The solid content was evaluated by the mass of carbon and PTFE divided by the total mass of the ink and the PTFE loading was determined by the mass of PTFE divided by the total mass of the solids. To simplify the discussion, each sample was named based on the level (high, medium, and low) of solid content (first letter) and PTFE loading (second letter).

Table 4.1: MPL formulation design criteria (S.C. stands for solid content).

Sample	S.C. (wt.%)	PTFE loading (wt.% of S.C.)	MPL ink carbon concentration (wt.%)
HL	15	15	12.6
HH	15	35	9.70
MM	10	25	7.10
LL	5	15	4.20
LH	5	35	3.20

4.1.2 Gas diffusion medium fabrication

The MPS was made from the commercially available carbon fiber paper (TGP-H-060) impregnated with a diluted PTFE suspension to reach 8 wt.% of PTFE content and dried in the oven at 100°C for 1 hour. Then the MPL inks were coated onto the MPS using Meyer rods, which is considered a contact coating method [110].Based on the solid content and viscosity of each ink sample, different size number of Meyer rods were used to yield similar MPL thickness of 25±5 μm for all samples (Figure 4.1). The MPL coated GDM samples were transferred to a needlepoint holder and dried in ambient conditions. To remove the surfactant and sinter the PTFE, the GDM samples were heat treated by the following temperature profile: (1) ramp-up to 300°C at the rate of 7°C/min, (2) hold at 300°C for 45 minutes, (3) ramp up to 380°C at the rate of 19°C/min, (4) hold at 380°C for 20 minutes and (5) cool-down to the room temperature at the rate of 0.5°C/min. The final MPL thickness is defined as the thickness difference between the GDM and MPS, which was measured using a material thickness gauge manufactured by CheckLine with a resolution of 2 μm.

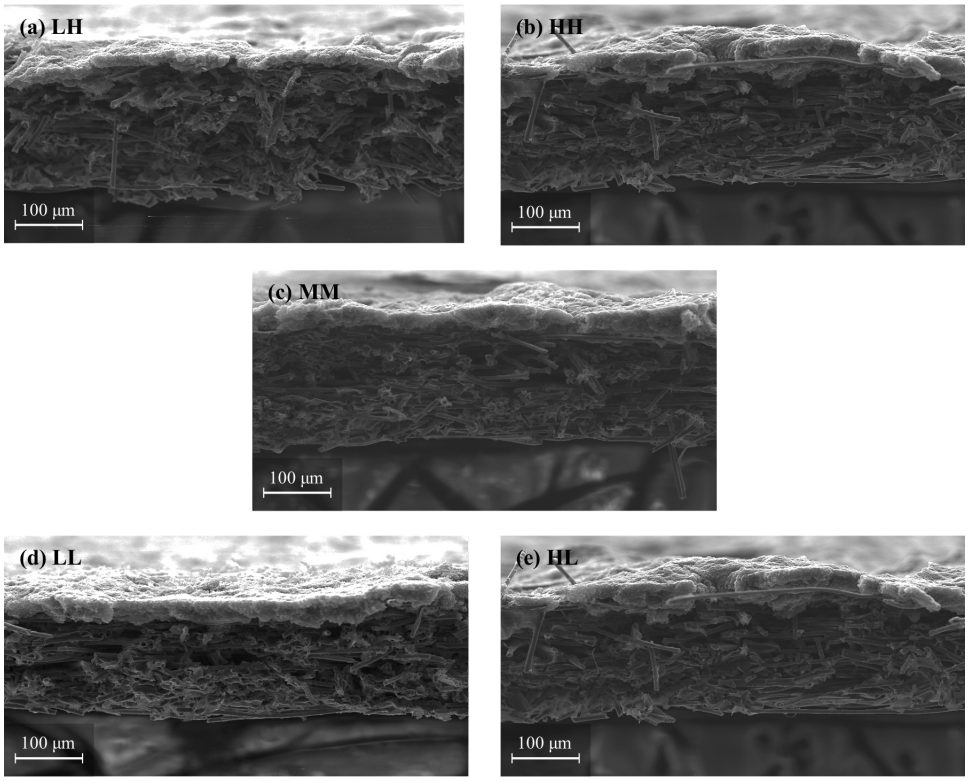

Figure 4.1: Low magnification SEM cross-sectional images of all GDM samples.

4.1.3 Particle size distribution and ink stability measurements

The hydrodynamic diameter of the dispersed particles can be estimated through their Brownian motion in the liquid medium using dynamic light scattering (DLS) technique [111]. To meet the requirements of DLS analysis, ink sample was diluted to 0.02 wt.% solid content with its respective solvent, followed by 10 minutes of low power sonication in a water bath. It was assumed that the dilution and sonication processes might break the large agglomerates connected by the weak Van der Waals force, but not the primary aggregates due to the stronger bonding [112]. Therefore, the particle size analysis in this study was used to evaluate the primary carbon network in the concentrated MPL slurry. Further, due to the uncertainties of measuring non-spherical particles, like fractal structures of carbon black, the particle size results are only considered qualitatively in this study [57, 112, 113]. To better understand the MPL ink components' contribution to the DLS results, the measurements were performed on the pure PTFE suspension and pure carbon inks to be compared with the results from the MPL ink. Another capability of DLS is to quantify particles' surface charge, Zeta (ζ) potential, based on their mobility in the medium that is exposed to an external electric field [111]. A higher absolute value of ζ-potential indicates greater repulsive forces among particles, which results in a more stable suspension [112]. Malvern Zetasizer Nano

ZS90 was used to perform DLS measurements. Three repeats, each has three measurements, were conducted on each sample to ensure data reproducibility.

4.1.4 Rheological characterizations

Rheological measurements were carried out using a rotational rheometer from NETZSCH Instruments Inc. with a roughened 40 mm parallel plate geometry. After the initial evaluation based on the particle size and flow properties, the working gap was set to 0.5 mm and the temperature was maintained at 25°C for all measurements. Multiple rheology tests were conducted to evaluate the general flow properties, shear-history dependent properties and the microstructural evolution of the MPL ink in response to the shear force. A pre-shear of 1 s^{-1} was applied before each test for 30 s followed by a 2-minute rest to standardize the initial condition. Firstly, viscosity was measured as a function of shear rate with a logarithmic ramp-up rate from 0.001 to 1000 s^{-1}. The second test was a three-step shear rate measurement, which simulates the actual coating condition and monitors the time-dependent flow behavior, also known as thixotropy, of the inks. There three steps are: (1) shear rate of 0.001 s^{-1} for 1 minute, which simulates the ink at storage condition, (2) step increase of shear rate to 500 s^{-1} for 10 seconds, which simulates the coating process and (3) step decrease of shear rate to 0.001 s^{-1} for 10 minutes, which simulate the coated thin film at rest. The third test consisted of a series of oscillatory amplitude strain (OAS) measurements, which further investigates the microstructure elasticity of the inks [114]. OAS provides information of elastic (solid particles) and viscous (dispersive medium) moduli of the ink as a function of stress/strain [115]. To study the strength of the microstructure before and after coating, OAS tests at the frequency of 1 Hz were performed with two different pre-shears of 1 s^{-1} and 500 s^{-1}, followed by three minutes stabilization. Lastly, OAS tests with a pre-shear of 1 s^{-1} were done at frequencies of 1 and 10 Hz to investigate the shear rate-dependent structural evolution.

4.1.5 Surface roughness and electron microscopy

Surface roughness was measured by a 2 μm tip stylus profiler (Bruker Dektak XT) at various locations on the GDM surface. Scanning electron microscopy (SEM) images were taken on both surface and cross-section of the GDM using Zeiss Gemini to assess the coating quality and pore structure in the MPL. The GDM prepared for the cross-section imaging was freeze-fractured after being held in the liquid nitrogen for 30 seconds.

4.1.6 Fuel cell characterization and testing protocols

The GDM samples were evaluated on the cathode side in a 2 cm^2 PEM fuel cell with straight channel flow field [116–119]. Standard PTFE impregnated TGP-H-060 with MPL was used on the anode side for all fuel cell tests to minimize the influence from anode GDM. Limiting current experiments were performed to study oxygen transport resistance in the cathode GDM [107]. Lastly, steady-state polarization curves were also obtained for all five MPL samples to evaluate overall fuel cell performance under both dry and wet conditions. To minimize the effect from anode DM, a standard Toray 060 diffusion media with MPL was placed on the anode side for all testing. PTFE gaskets with different thickness were used to control the compression of Toray TGP-H-060 to be 22±1.5%. Straight parallel flow field (as shown in Figure 4.2), made of POCO graphite, with an active area of 2 cm^2 was used to perform fuel cell experiments. Commercially available membrane electrode assembly (MEA) from Ion Power, USA, consisting of Nafion™ NRE211 membrane (25 µm thick) and Pt/C catalyst with a loading of 0.30 mg_Pt/cm^2 on each side was used in all cells for fuel cell testing. Ultra-high purity (99.999%) hydrogen, air, and nitrogen gases were used.

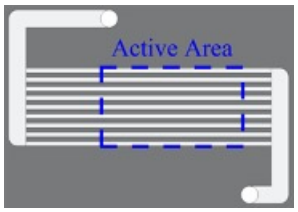

Figure 4.2: Top-view of straight-parallel flowfield.

Greenlight G20 fuel cell test station was used to run fuel cell experiments, and Gamry Reference 3000 Potentiostat/Galvanostat was used to measure HFR (High Frequency Resistance) and to perform limiting current experiments as well. Standard limiting current protocols[120–122] were used to measure oxygen transport properties under both dry (80°C and 64% RH) and wet (70°C, 90% RH and 300 kPa) conditions. Under dry conditions, limiting current experiments were ran at four different pressures: ambient, 150, 200, and 300 kPa, and the dry mole fraction of the oxygen were varied between 1 to 4%. Under wet conditions, limiting current experiments were performed at 300 kPa., and the dry mole fraction of the oxygen were varied between 1 to 21%. Steady-state fuel cell performance data were also collected under both dry (70°C, 64% RH and 100 kPa) and wet (70°C, 100% RH and 300 kPa) conditions.

4.2 Study of microporous layer ink

4.2.1 Ink stability and Primary aggregate size distribution

Interparticle attractive or repulsive forces that reflects suspension stability can be quantified through ζ-Potential, as shown in Table 4.2. The ζ-Potential data show that the PTFE suspension has the highest stability. The stability of the MPL ink is lower than that of the PTFE suspension and is close to the stability of the corresponding pure carbon inks without PTFE. The lower stability of the MPL ink could be due to the tendency of the carbon particles to agglomerate. For most of the inks, the average ζ-potential is -28 mV, indicating reasonable stability of the suspension [123]. However, the LH sample has a ζ-potential close to the threshold for agglomeration ($|\zeta - Potential| < 15$mV) [123], which makes it less stable than the other inks. Nevertheless, the LH sample did not show signs of phase separation during the coating process nor during the rheological measurements.

Table 4.2: ζ-Potential of diluted PTFE suspension and MPL inks (S.C. stands for solid content).

Diluted Sample	ζ-Potential (mV)
PTFE Suspension	-43.0 ± 3.0
HL	-30.0 ± 1.6
HH	-26.8 ± 2.0
MM	-27.8 ± 1.0
LL	-26.5 ± 1.8
LH	-17.3 ± 1.2
5 wt.% S.C, No PTFE	-27.3 ± 2.8
10 wt.% S.C, No PTFE	-26.5 ± 1.3
15 wt.% S.C, No PTFE	-26.2 ± 1.7

Figure 4.3(a) shows the particle size distributions of the PTFE suspension and five ink samples. The particle size for the PTFE dispersion was measured before and after mixing with the ink solvent using ball milling. In both cases, the PTFE suspension had a narrow size distribution, with an average particle size of 220 nm, consistent with the manufacturer specifications [124]. In the case of the five MPL ink samples, the average particle size obtained from the high intensity peak was between 250 and 350 nm with large variation of the particle size distribution. Takahashi et al. [27] obtained a bimodal particle size distribution for a complex carbon based slurry, similar to the results reported here for the HH sample. Their cryogenic SEM observations confirmed the existence of a wide range of carbon aggregate/agglomerate sizes. In this study, due to the high ζ-potential of the PTFE suspension and its low chemical affinity, the particle size distribution is expected to be determined by the carbon aggregates formed during the mixing process. The size distribution

observed in Figure 4.3(a) is the polydispersity index (PDI) and can be calculated as [125]:

$$PDI = \left(\frac{d_{std}}{d_{peak}}\right)^2 \tag{4.1}$$

where d_{std} and d_{peak} are the standard deviation and the peak value of the particle size distribution, respectively. As shown in Figure 4.3(b), the PDIs calculated from all ink samples are less than the instrument's recommending measurement threshold (< 0.7), confirming the reliability of the measurements. LL, LH, and HL have lower PDI, indicating a more homogeneous carbon aggregate size distribution than HH and MM samples. On the other hand, MM and HH have higher PDIs, with HH showing a bimodal size distribution indicating the existence of various aggregate sizes in the ink. The effect of formulation on the primary particle size distribution was more significant when the solid content was above 10 wt.%. The particle size distribution of the MPL inks are compared to their corresponding pure carbon ink without PTFE in Figure 4.4. The results show that adding less than 25 wt.% of PTFE has little effect on particle size distribution. However, for high PTFE loading (35 wt.%) MPL inks, the particle size distribution is broader than the corresponding pure carbon ink, especially at high solid content (HH). The DLS results indicate that adding high PTFE content at high solid content may interfere with the homogeneous mixing of the carbon particles, which results in the formation of a broader range of carbon agglomerate sizes.

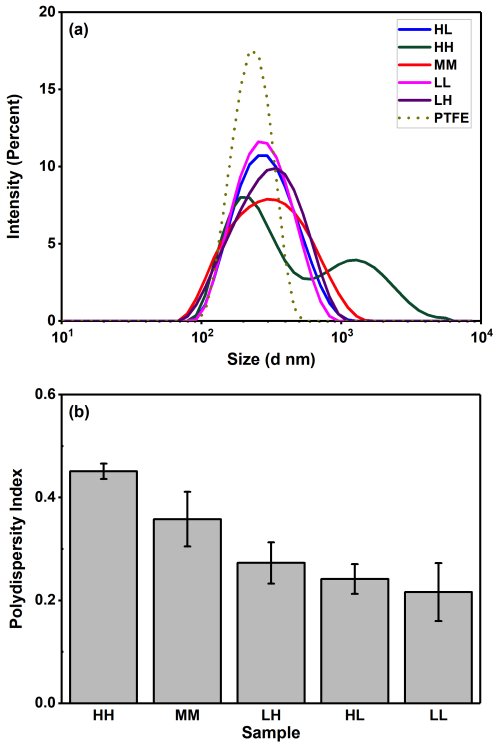

Figure 4.3: Dynamic light scattering of diluted MPL ink samples, (a) particle size distribution of the inks and the PTFE suspension used in the formulation, and (b) calculated polydispersity index of the inks.

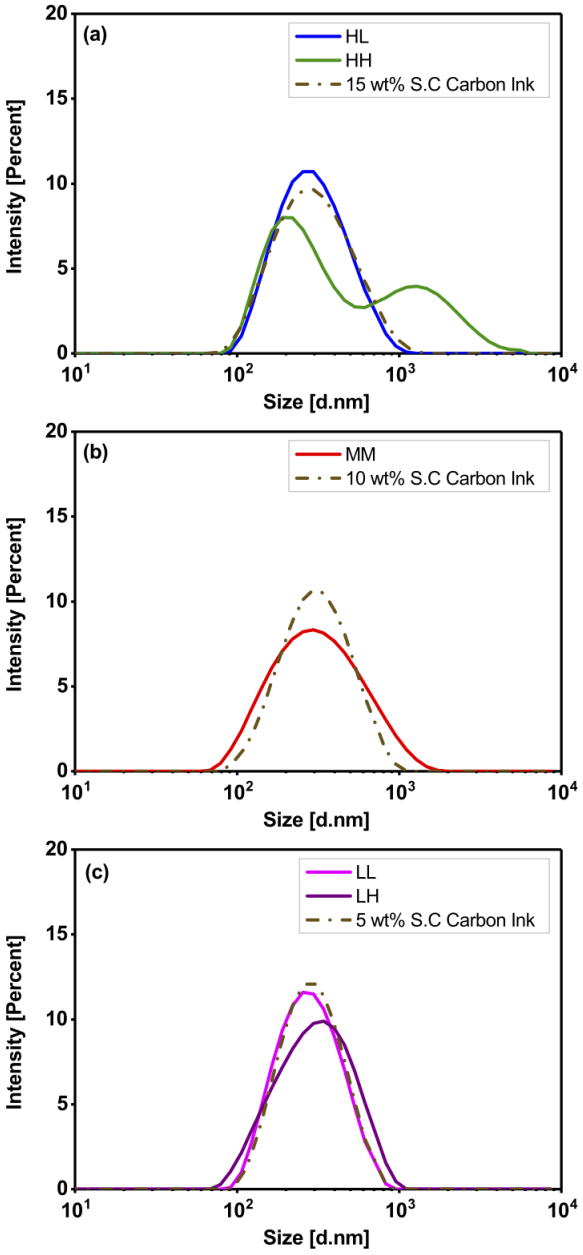

Figure 4.4: Particle size distribution of the MPL inks compared to the corresponding pure carbon inks without PTFE of a) 15 wt.%, b) 10 wt.%, and c) 5 wt.% solid content inks.

4.2.2 Flow behavior under steady shear conditions

Bulk flow behavior of the MPL inks was evaluated by measuring viscosity as a function of shear rate, as shown in Figure 4.5(a). In general, all samples exhibited shear thinning behavior. However, a transitional rise in viscosity was observed at intermediate shear rates (10-100 s^{-1}), which splits the flow curve into three regimes marked as I, II, and III in Figure 4.5(a). Similar flow behaviors have been reported previously for other suspensions of carbon black [55, 126–129]. The steep viscosity drop in region I can be attributed to the breakdown of weakly connected agglomerates and their alignment with the flow direction [127]. In addition, samples under low shear rates (region I) showed yield stresses, requiring a minimum shear stress to initiate flow [130]. The viscosity increase in region II indicates the emergence of flow resistance, which can be attributed to the formation of temporal anisotropic clusters under the dominance of hydrodynamic forces [126, 131–133]. Further increase in the shear rate can overcome this transient resistance and break the agglomerates down into even smaller particles aligned in the shear direction (region III). Upon further analysis, the viscosity at low (0.01 s^{-1}) and high (1000 s^{-1}) shear rates increases with carbon mass fraction, as shown in Figure 4.5(b). On the other hand, no specific trend was found between PTFE loading and viscosity, as also found by Stampino et al. [59], indicating that the ink viscosity is dominated by carbon concentration. Further, the yield stress, determined from steady shear viscosity test in Figure 4.5(b), increases with carbon concentration suggesting a more solid-like gel at resting condition [55, 134].

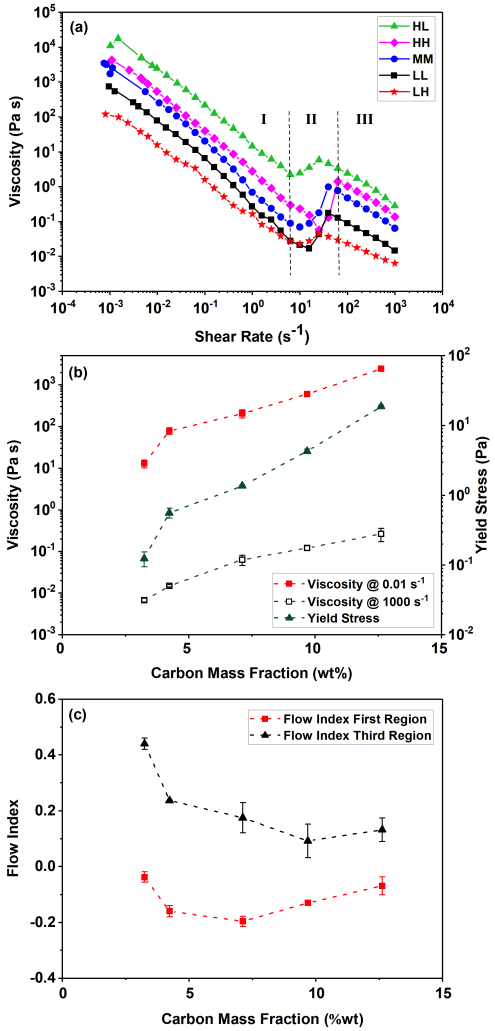

Figure 4.5: (a) viscosity (b) low-shear viscosity (0.01 s^{-1}), high-shear viscosity (1000s^{-1}), and yield stress as a function of the carbon mass fraction, and (c) comparison of sample flow index in regions I and III.

Viscosity data in regions I and III (first and second shear thinning) can be fitted into a power-law model (fitted constants shown in Table 4.3):

$$\eta = K\dot{\gamma}^{n-1} \tag{4.2}$$

where n is the flow index, η is the viscosity (Pa.s), K is the consistency index (Pa.s^n) and $\dot{\gamma}$ is the shear rate (s^{-1}). The fluid is referred to as shear thinning when the flow index is less than one [115] and the level of shear thinning increases with decreasing flow index. It is found that for all samples, the second shear thinning region (III) has higher flow index than the first region, indicating a less shear rate dependent flow as shown in Figure 4.5(c). Thus, the agglomerates existed in the transitional region (II) were broken down into smaller particles

in region III. The flow index in region I does not show a strong correlation with carbon concentration likely due to the large scale break down of the agglomerates, which is similar for all compositions and reported previously [127]. In contrast, the flow index in the high shear region (III) first decreases, then reaches plateau with increasing carbon concentration as shown in Figure 4.5(c). Higher shear thinning for samples with carbon mass fraction greater than 5 wt.% indicates the existence of large agglomerates that can be continuously broken down with increasing shear rate [135].

Table 4.3: Power-law model ($Property = a{\phi_c}^b$ and ϕ_c: carbon mass fraction) parameters fit to the several rheological properties plotted versus carbon mass fraction of the ink.

Property	Model Parameters		R^2
	a	b	
Viscosity at 0.01 s^{-1}	0.4040	3.33	0.970
Viscosity at 1000 s^{-1}	0.0003	2.78	0.999
Yield Stress (Pa)	0.0029	3.33	0.962
Elastic Modulus at LVER (Pa)[a]	0.3240	3.30	0.969
Cohesive Energy (J/m^3)[a]	0.4540	3.20	0.963

[a] Samples at stationary condition (Pre-shear 1 s^{-1})

The degree of shear thickening in region II is defined as the ratio of the maximum to minimum viscosity ($\frac{\eta_{max}}{\eta_{min}}$) as shown in Table 4.4. No clear trend can be observed from the degree of shear thickening because the emergence and extent of this transitional flow resistance is complicated and can be influenced by multiple factors like solid mass fraction and particle anisotropy [127, 136]. Since the carbon agglomerates often show fractal shapes [137], it is difficult to differentiate the effect of carbon mass fraction and particle size distribution on the degree of shear thickening. Nevertheless, the shear rates of the actaul coating process are much higher than 100 s^{-1} [59], which is beyond this observed transitional region.

The viscosity measurement with increasing shear rate shown in Figure 4.5(a) provides general flow properties of the samples but lacks detailed microstructural information [138]. Further rheological analyses are required to investigate the microstructure of the ink under simulated coating shear rate.

Table 4.4: Comparison of the degree of shear thickening obtained from steady shear and stepped shear viscometry.

Sample Name	$\frac{\eta_{max}}{\eta_{min}}$ [a]	$\frac{\eta_{3rd}}{\eta_{1st}}$ [b]
HL	2.50	4.75
HH	24.0	7.55
MM	14.3	9.05
LL	10.4	5.01
LH	1.97	4.79

4.2.3 Flow behavior under simulated processing condition (Thixotropy)

The actual coating process involves three stages: (1) prior to the coating when ink is at the stationary or low shear condition, (2) high shear condition when a thin film is coated onto a subtract, and (3) post coating when the microstructure recovers. To simulate the coating process, three-step shear rate experiments were conducted and the sample recovery was quantified by the viscosity difference between the third and the first stages [139]. As shown in Figure 4.6, all MPL inks not only recovered quickly but also reached a higher viscosity, which is the signature of a flow property known as rheopexy or negative thixotropy [55, 128, 140]. At the first stage (stationary condition), agglomerates form a loosely bonded gel network. Under high shear conditions in the second stage, the network can be easily broken into smaller particles (potentially primary aggregates) that align with the shear stress tensor, as visualized by Osuji et al. [141]. Due to the existence of smaller particles, the total surface area increases, which in turn results in higher interparticle interactions after removal of the shear field. Consequently, a highly percolated state of gelation was formed in the third stage [142]. The ratio of the average viscosity in the first and third regions are calculated and shown in Table 4.4. For the low solid content samples, the increase in the viscosity is similar regardless of the PTFE loading. Among the samples with higher solid content (MM, HH, and HL), those with intermediate to high PTFE concentration (MM and HH) show greater increase of the viscosity between the third and the first stages. This indicates that the microstructure of the high PTFE samples is more highly percolated as a result of the applied coating shear force. In addition, the HH and MM samples also have the widest agglomerate size distribution due to the mixing in presence of high PTFE concentration. The combined results suggest that the ink with high PTFE content can form a highly percolated gelation state after experiencing the high coating shear rate condition.

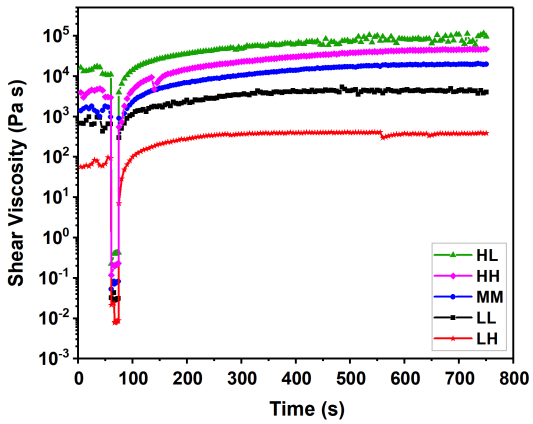

Figure 4.6: Viscosity evolution under three-step shear rate, beginning by shear rate of 0.001 s^{-1} applied for 1 minute (showing the intact ink), followed by shear rate of 500 s^{-1} for 10 s (coating condition) and relaxed at 0.001 s^{-1} for 11 minutes (recovery as a wet film).

4.2.4 Microstructure strength in response to oscillatory shear strain

Elastic modulus (G′) represents strength of the solid network in the ink dispersion and can be measured by oscillatory tests. Figure 4.7(a) shows the results of G′ as a function of shear rate and shear strain at the frequency of 1 and 10 Hz for MM sample. The interval at which G′ remains constant is called the linear viscoelastic region (LVER) [115], which is commonly used to study the ink microstructure under intact condition. Comparing the results of G′ from two frequencies demonstrates that the LVER is governed by shear strain (deformation), while the shear thickening transition is governed by the shear rate (speed). A specific amount of deformation is required to break down the structure to start the flow. At the intermediate shear rates (10-100 s^{-1}), a transitional increase in G′ represents the shear thickening behavior similar to that observed in the viscosity curves, which confirms the shear rate dependent transient cluster formation. Similar dependency of LVER and shear thickening transition can be observed for all samples as shown in Figure 4.8. The average elastic modulus within the LVER is presented in Figure 4.7(b), which shows a power-law relationship with carbon mass fraction (fitted parameters shown in Table 4.3). In the literature, similar relationship between elastic modulus and carbon mass fraction was observed from the inks made of Vulcan and Ketjen black [126, 130].

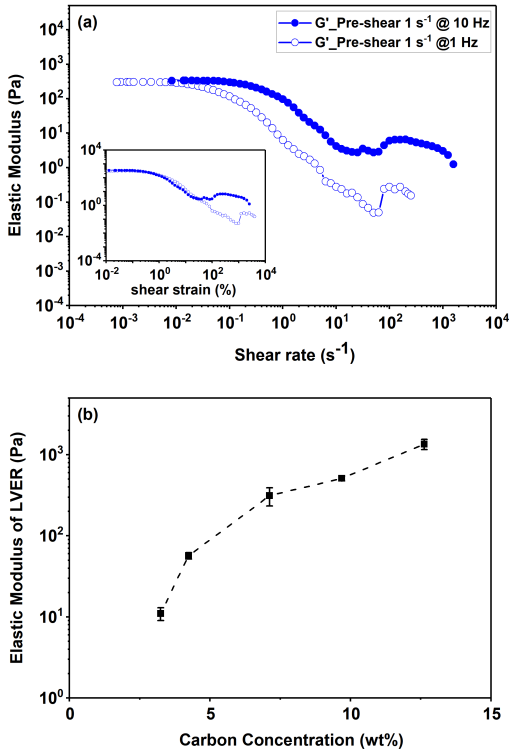

Figure 4.7: (a) Elastic modulus of the MM sample as a function of shear rate obtained from the OAS test at frequencies of 1 and 10 Hz. Inset: Elastic modulus versus shear strain, and (b) Elastic modulus of all samples, within the LVER, as a function of carbon mass fraction.

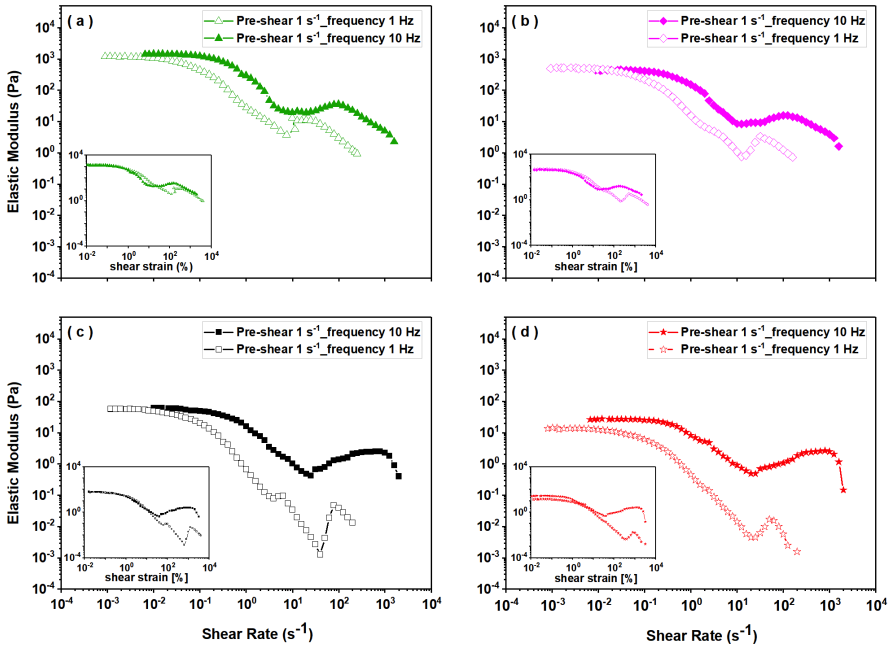

Figure 4.8: Elastic modulus of (a) HL, (b) HH, (c) LL, and (d) LH samples as a function of shear rate obtained from OAS test at frequencies of 1 and 10 Hz.

To evaluate the microstructural evolution under the influence of coating, OAS tests at a frequency of 1 Hz were performed on samples with pre-shear of 1 and 500 s^{-1} to simulate the microstructure before and after coating, respectively. Figure 4.10 shows the resulting elastic (G') and viscous (G'') modulus of each sample after both pre-shear conditions. Regardless of the pre-shear condition, G' is an order of magnitude greater than G'', exhibiting a gel-like material for all samples [143]. To focus on the carbon network, the G' of all samples are plotted in Figure 4.9(a), which shows that the LVER is extended under the influence of higher pre-shear. Higher LVER shear stain represents a stronger percolation network, which requires larger deformation (higher strain) to break down the structure. The results indicate that the MPL ink experiences a shear-induced transition from weakly connected gel to highly percolated gel after the coating process. The difference in LVER shear strain of the pre-shears of 1 and 500 s^{-1} is normalized by that of 1 s^{-1} and the ratios are shown in Figure 4.9(b). The level of microstructural percolation is lower for low solid content samples (LL & LH) compared to that of the intermediate and high solid content samples due to the presence of fewer carbon agglomerates. The increase of the LVER is found to be the greatest for the MM and HH samples. This observation is consistent with the three-step shear rate testing results. The greater LVER suggests higher level of interparticle interactions, which may be resulted from the particle size inhomogeneity of the primary agglomerates.

Cohesive energy (CE) is a more comprehensive property to evaluate the strength of the agglomerated network, considering both the magnitude of elastic modulus and the extent of the LVER. Cohesive energy can be calculated by [115]:

$$CE = \frac{1}{2} G' {\gamma_c}^2 \tag{4.3}$$

where γ_c is the critical shear strain of LVER and G' is the elastic modulus. According to Figure 4.9(c), cohesive energy increases with carbon mass fraction, suggesting a more compact microstructure by increasing carbon concentration. The cohesive energy of the gel network formed with 500 s^{-1} pre-shear is about one order of magnitude higher than that with 1 s^{-1} pre-shear.

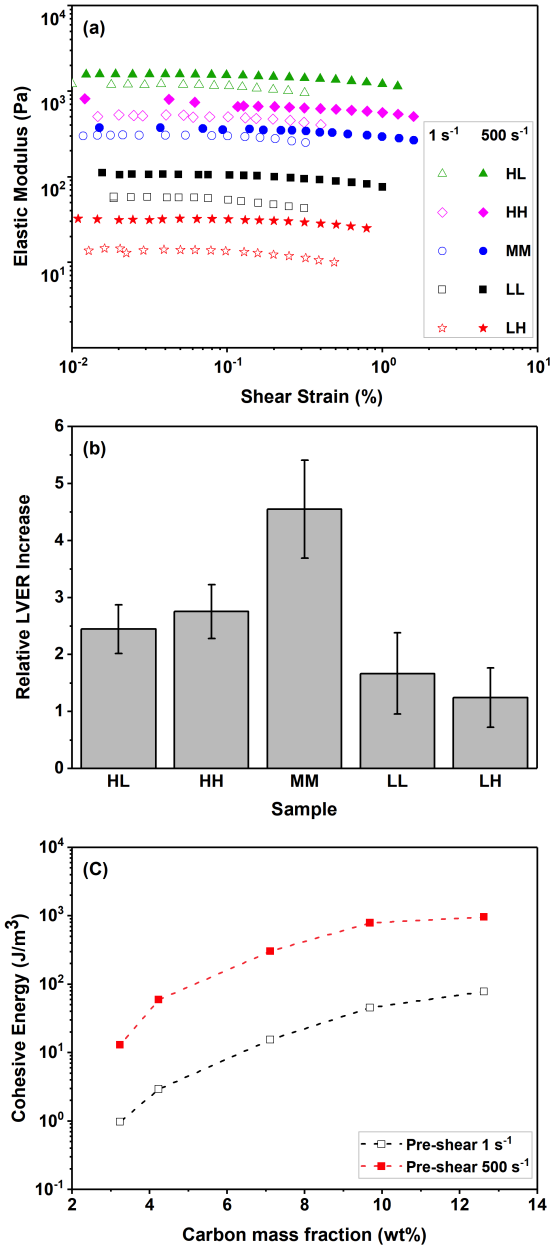

Figure 4.9: Oscillation amplitude sweep at a frequency of 1Hz for samples pre-sheared at 1 and 500 s^{-1}. (a) Elastic modulus before and after high pre-shear, (b) relative increase in LVER at high pre-shear compared to low pre-shear and (c) the cohesive energy of the gel network as a function of carbon mass fraction.

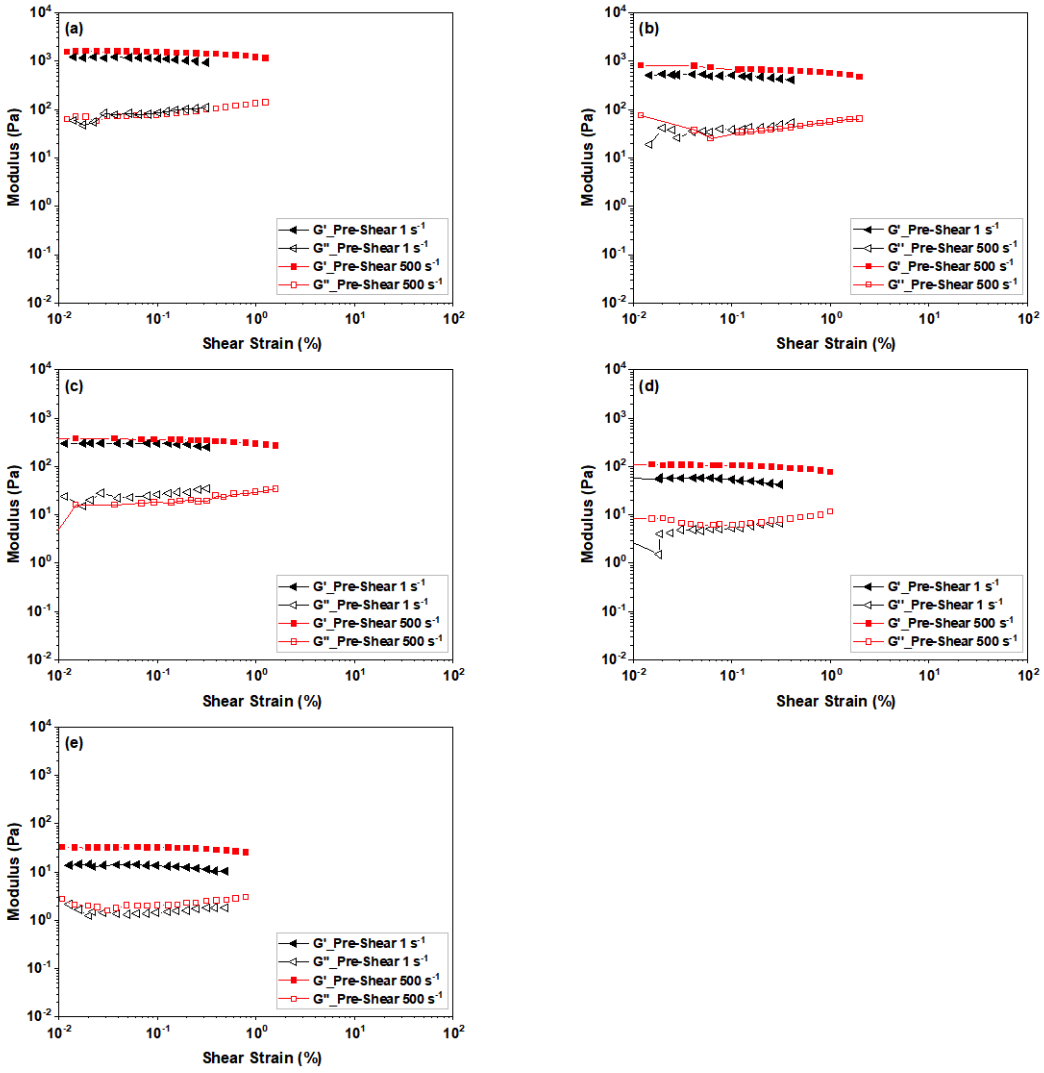

Figure 4.10: Oscillation amplitude sweep at a frequency of 1 Hz for samples pre-sheared at 1 and 500 s^{-1}. The elastic (G′) and viscous modulus (G′′) for (a) HL, (b) HH, (c) MM, (d) LL, and (e) LH.

In conclusion, the oscillation assessments reveal that the compactness of the microstructure is a strong function of the carbon concentration. Further, a broader aggregate size distribution can also result in a high level of shear-induced microstructural percolation. Therefore, an ink with lower carbon concentration but wider aggregate size distribution may experience higher percolation than an ink with higher carbon concentration but more homogeneous aggregates. Further, the key rheological properties of the ink all exhibit similar power-law relationships as a function of the carbon mass fraction, as summarized in Table 4.3.

4.2.5 Shear-induced microstructural evolution

Based on the rheological and the dynamic light scattering results, primary carbon aggregate size distribution and the shear force are two critical factors affecting the microstructure of the ink. Therefore, we have proposed a mechanism to describe the microstructural evolution of the MPL ink. Figure 4.11(a) and (b) illustrate the microstructure of the low and high PTFE loading inks, respectively, under steady condition after mixing. Both inks are composed of relaxed and loosely connected agglomerates of carbon particles. In the case of the low PTFE loading sample, in Figure 4.11(a), more interconnected carbon agglomerates are formed due to its higher carbon mass fraction, which results in higher viscosity, such as that of sample HL. During a high-shear coating process, agglomerates can be broken down to the primary aggregates and aligned with the flow, as shown in Figure 4.11(b) and (e). As observed from the DLS, the primary aggregates of the higher PTFE loading sample have a wider size distribution, while the aggregates show a more homogeneous size distribution for lower PTFE loading. After removing the shear force, the originally aligned layers are disturbed and the highly attractive aggregates form a new state of gelation, as shown in Figure 4.11(c) and (f). Based on the three-step shear rate measurement data, the stage 3 carbon network is more closely percolated than that in stage 1. For the lower PTFE loading sample, the microstructure formed in stage 3 is more compact but closely resembles that in stage 1 due to the similar hydrodynamic size of the primary aggregates. On the other hand, the higher PTFE loading sample has a wider aggregate size distribution at stage 2 compared to the initial stage, which forms a new state of gelation after coating. The post coating microstructure contains both locally flocculated carbon particles and open areas, which may result in an inhomogeneous pore structure in the MPL, such as that observed for sample HH.

4.3 Performance of microporous layer

4.3.1 Coating quality and microstructure

Different crack size and density can be observed from SEM images of the MPL surface shown in Figure 4.12. rack formation is due to the anisotropic stress distribution within the thin film thickness, which is a function of the ink formulation, microstructural features, thickness, and drying condition [144–147]. The crack size of MM, HH, and HL is greater than that of LL and LH for two possible reasons. First, the lower viscosity of LL and LH results in better distribution of the ink on the rough substrate. Second, the intermediate and high solid content inks exhibit a highly percolated gel network, which results in less microstructural flexibility during drying [145]. Among the samples with solid content above 5 wt.%, HL has the highest viscosity and yield stress, which make low fluidity a dominant

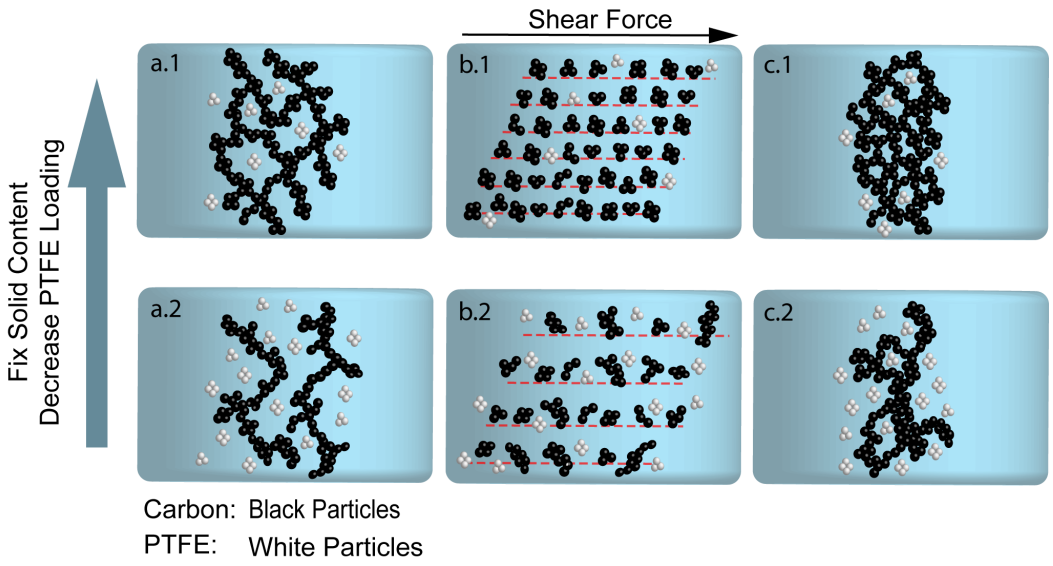

Figure 4.11: Proposed shear-induced microstructural evolution in the MPL ink for: Low (a, b, c) and high (d, e, f) PTFE content under stationary, coating and post-coating conditions, respectively.

cracking mechanism that results in the formation of surface defects like the uncoated areas identified in Figure 4.12(e). In contrast, the crack formation in MM and HH, with relatively high fluidity compared to HL, is suspected to be microstructure driven. Schneider et al. [147] found that a more homogeneous and stabilized agglomerate distribution in a suspension can minimize anisotropic stress differences during drying, which in turn reduces crack density. This also explains why MM and HH have more cracks, which are due to their inhomogeneous microstructure distribution as measured by DLS. Further, the rheological results show that the coating pre-shears induce a higher level of network percolation in MM and HH samples compared to others.

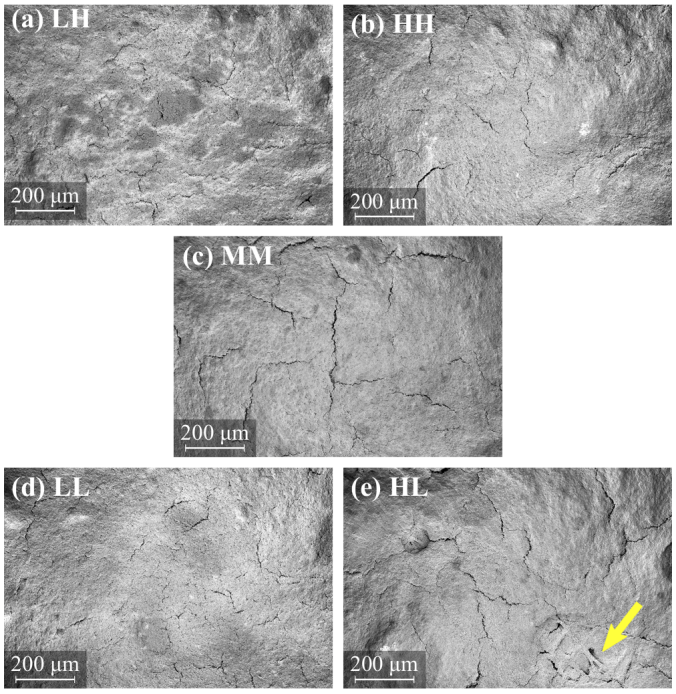

Figure 4.12: SEM images of the MPL surface. The arrow in figure (e) pointed at an uncoated carbon fiber from the substrate due to the high viscosity of the HL ink.

MPL cracks may have a positive effect on fuel cell performance through assisting the mass transport in certain operating conditions [7], but they are found to be detrimental for the catalyst layer durability [148]. Therefore, macro-cracks observed from HL, HH, and MM samples should be avoided in fabricating MPL. In addition to surface images, MPL cross-sectional images were taken from freeze-fractured samples to observe the microstructure as shown in Figure 4.13. t a fixed solid content, the samples with higher PTFE loading show more heterogeneous and open microstructure, especially at 15% solid content. The yellow line in Figure 4.13(b) highlights a highly flocculated agglomerate, which is surrounded by micro-scale pores while nanoscale pores exist in more uniformly distributed aggregates. Ito et al. [149] also reported larger pore sizes observed from an MPL with a high PTFE loading through porosimetry measurement. In the case of the MM sample, the microstructure has a morphology that has some level of heterogeneity, but the agglomerates are not as flocculated as HH. The agglomerate size distributions observed from cross-sectional images are consistent with the DLS results, and the existence of percolated agglomerates in MM and HH samples agree with the shear-induced structural evolution from rheology measurement. In conclusion, the samples with higher PTFE loading have a wider range of carbon agglomerate sizes, which result in a broader pore size distribution.

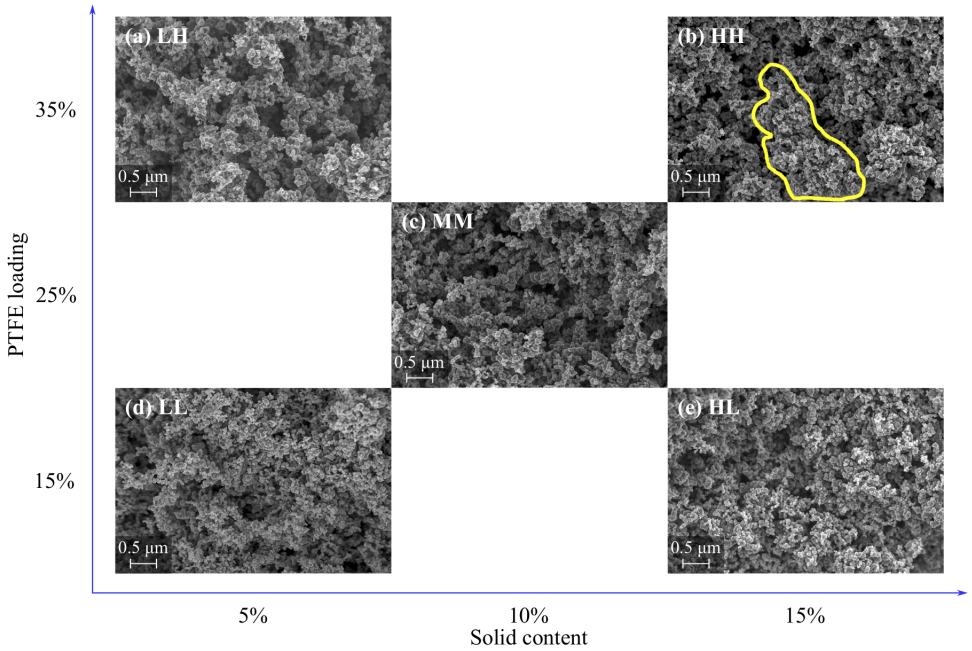

Figure 4.13: SEM images showing the through-plane MPL microstructure. The yellow line in (b) HH sample highlights a highly percolated agglomerate.

4.3.2 Surface roughness

A profilometer was used to measure the surface roughness of each sample and the raw data are shown in Figure 4.14. The average roughness from five locations on each sample is reported in Table 4.5. The HL sample has the highest roughness and the surface profile in Figure 4.14 shows a repeating pattern of peaks and valleys. This high roughness is suspected to be due to the combination of high viscosity and low flow leveling of the HL sample coated by Meyer rod. The MM sample also shows slightly higher average roughness, which could be attributed to surface cracks observed from Figure 4.12(c) since the peak and valley are more randomly distributed as shown in Figure 4.14. In general, a smoother MPL surface is preferred to promote intimate contact with the catalyst layer, which enhances cell performance and durability [150, 151].

Table 4.5: Average roughness factor for the MPL.

Sample	Average Ra (µm)
HL	13.8 ± 2.3
HH	5.50 ± 0.5
MM	9.60 ± 1.2
LL	6.70 ± 1.3
LH	6.10 ± 0.7

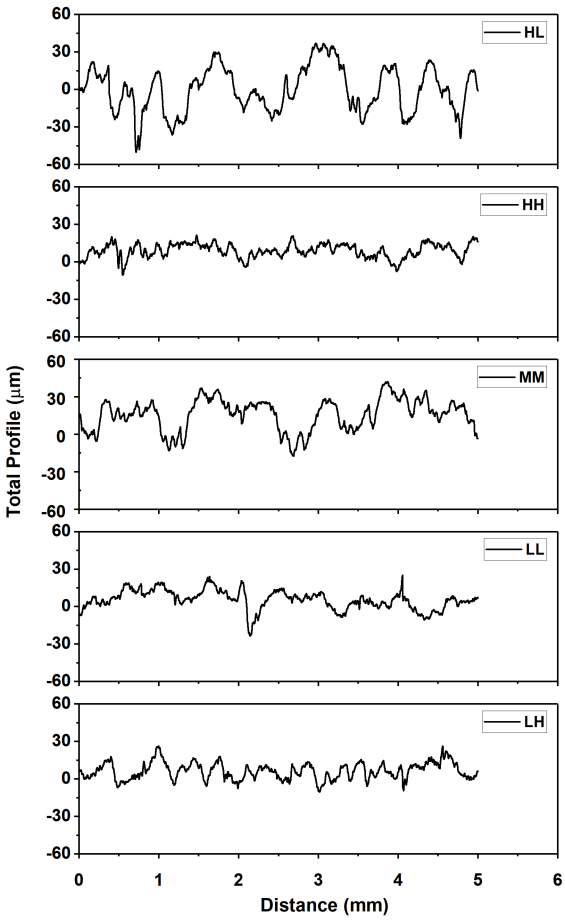

Figure 4.14: MPL surface roughness measurement of a line scanned profile.

4.3.3 Gas transport properties

The in-situ limiting current method is applied to investigate the gas diffusion properties of the GDM under both dry and wet conditions [152]. Under dry conditions, the oxygen diffusion resistance could be derived from the limiting current densities at various total pressures, as shown in Figure 4.15. Based on the slope and intercept of the results in Figure 4.15. Based on the slope and intercept of the results in Figure 4.15, the ratio of nominal diffusivity to effective diffusivity, D/D_{eff}, and the non-pressure dependent resistance, R_{others}, of the GDM can be obtained, as shown in Table 4.6 [122]. The D/D_{eff} ratio represents the intermolecular diffusion through pores greater than 50 nm and can be correlated to the ratio of tortuosity to porosity of the GDM [107]. In contrast, the non-pressure dependent resistance, R_{others}, is dominated by Knudson diffusion through pores less than 50 nm in the GDM [109]. Within the GDM, the large size pores mainly located in the MPS, while small pores exist mostly in the MPL.

Table 4.6: Oxygen transport properties under dry condition.

Sample Name	Dry D/D_{eff}	R_{others}
-	-	(s/cm)
HL	5.0 ± 0.1	0.48
HH	4.9 ± 0.1	0.67
MM	4.4 ± 0.1	0.35
LL	4.9 ± 0.1	0.72
LH	4.7 ± 0.1	0.75

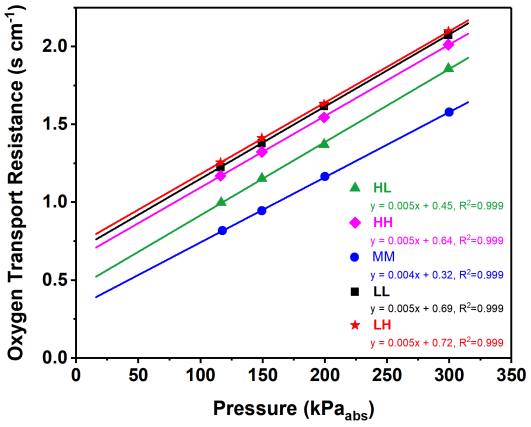

Figure 4.15: GDM oxygen transport resistance as a function of pressure under dry condition (80°C and 64% RH).

Since the same MPS was used in all fabricated GDM, a similar D/D_{eff} ratio was obtained for all samples, as shown in Table 4.6. The MM sample has slightly lower D/D_{eff} likely due to macroscale cracks in the MPL, as observed from Figure 4.12. The non-pressure dependent resistance, R_{others}, resulting from the MPL microstructure shows a noticeable difference among the samples. LL and LH GDMs have higher R_{others}, likely due to a combination of minimal cracks and higher degree of MPL penetrating into the MPS creating more nanoscale pores since their precursor inks have lower viscosity. In contrast, inks with intermediate and high solid contents have relatively higher viscosity, and so less MPL penetration into the MPS and more cracks in the MPL. Therefore, lower R_{others} can be found for HH, HL, and MM samples. The intermediate morphological features of MM and high crack density resulted in the lowest gas transport resistance in the MPL.

Figure 4.16 shows the increase of oxygen transport resistance as a function of limiting current density under wet conditions. A standard dry, transition, and wet transport regions of Toray 060 MPS [108, 121] can be observed for all samples in Figure 4.16. Under wet conditions, the porosity is decreased, and the tortuosity is increased in the GDM due to water condensation. In addition, the oxygen may need to diffuse through the liquid water film that

exists at the interface between the MPL and the catalyst layer to reach the catalyst sites. Therefore, the oxygen transport resistance increases as soon as liquid water condensation occurs in the MPS. Based on the results in Figure 4.16, the order of transport resistance in the wet region follows that of the dry region, indicating similar governing parameters. Lower transport resistance and a stable plateau in the wet region can be observed for the MM sample indicating efficient liquid water removal pathways in this sample [121]. The HL, LL and LH samples show similar wet transport resistance in the wet region, but higher than that of the MM sample. In contrast, the HH sample showed the highest oxygen transport resistance, which did not reach a stable plateau, potentially due to higher water accumulation in the MPL. According to the DLS measurement and SEM images, HH sample showed a wide range of agglomerate and pore size distribution, so the liquid water may condense and block the large pores in the MPL due to low capillary pressure under wet conditions. The oxygen transport resistance under wet conditions is difficult to deconvolute without a in-situ water visualization tool and can be influenced by highly complex and interactive phenomena. Nevertheless, our results successfully demonstrate the critical role that the MPL plays for transporting oxygen effectively under wet condition.

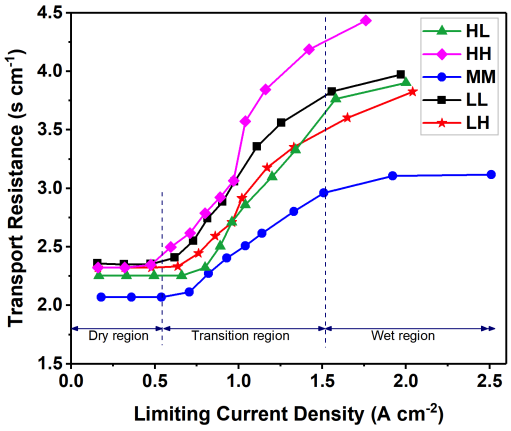

Figure 4.16: Total oxygen transport resistance as a function of limiting current density under wet condition (70°C, 80% RH and 300 kPa).

4.3.4 PEMFC Performance

To validate our measured GDM properties, fuel cell polarization curves were obtained under both dry and wet conditions. The cell voltage was determined by kinetic, ohmic, and mass transport resistances [107]. Since the same commercialized membrane electrode assembly was used for all cells, the difference in kinetic resistance is negligible. The dry fuel cell performance in Figure 4.17 agrees very well with the dry oxygen transport resistance

shown in Figure 4.15. Similarly, the wet fuel cell performance shown in Figure 4.18 also agrees with the wet transport resistance observed in Figure 4.16. Since the ohmic resistances measured by high frequency resistance (HFR) for all samples are almost identical, the performance difference for both dry and wet polarization curves can be attributed solely to oxygen transport resistance. In other words, the fuel cell performance increases with reducing oxygen transport resistance. At 0.2 V, the MM sample shows 69% (dry) and 47% (Wet) performance improvement compared to the HH sample. These fuel cell performance results further confirm the significance of MPL composition and microstructure and their effect on oxygen transport resistance.

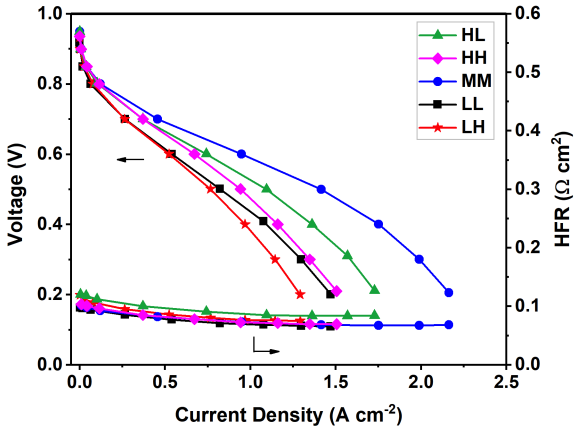

Figure 4.17: Fuel cell performance curves of the diffusion medias under dry conditions (70°C, 64% RH and 100 kPa).

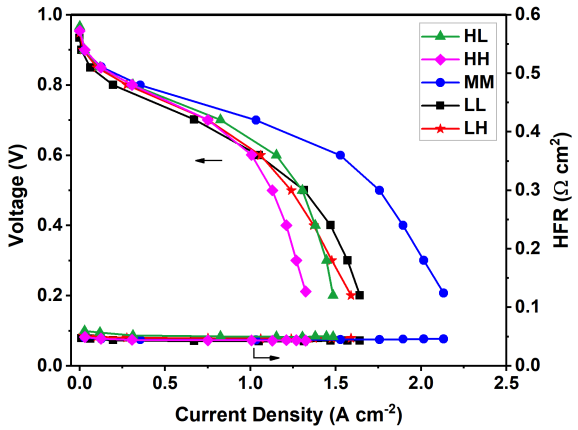

Figure 4.18: Fuel cell polarization curves of the five studied GDM under wet operating conditions (70°C, 100% RH, and 300 kPa).

4.4 Conclusions

In this study, the flow properties of the microporous layer (MPL) ink as a function of its formulation and external shear forces were investigated for the first time. Understanding the effect of formulation on the gel network in MPL's precursor ink provides critical information about the final MPL morphology and surface qualities. Dynamic light scattering results suggested a more inhomogeneous mixing of carbon particles in the presence of high PTFE concentrations, especially at high solid content (> 5 wt.%) and PTFE loading (> 15 wt.%). Viscosity results indicated that the MPL inks, similar to other carbon-based slurries, are highly shear thinning. However, at intermediate shear rates (10-100 s^{-1}), a transient shear thickening region was observed in all samples. Applying high shear rates associated with the coating process (~ 500 s^{-1}) resulted in a more percolated gel network in the thin wet film compared to that in the intact ink. The level of microstructure percolation was found to be a function of both the carbon concentration and the aggregate size distribution. Most of the rheological properties of the inks were found to be a power-law function of the ink carbon content. The coating quality of the MPLs was found to be a strong function of its flow properties, where samples with lower viscosity exhibited improved flow leveling during coating and drying and developed less cracking. The through-plane morphology of the MPLs was observed to be consistent with the projected rheological microstructure and the samples with lower PTFE loading exhibited a more homogeneous microstructure. The sample with 10wt.% solid content and 25 wt.% PTFE loading (named MM) had an optimized morphology, where the agglomerates were neither too percolated nor too homogeneously distributed. As a result, the MM sample demonstrated enhanced oxygen transport under both dry and wet conditions, which enabled high current density operation of a fuel cell. The findings of this study provide new MPL design guidelines for improving fuel cell performance and durability.

Chapter 5

EFFECT OF HIGH ASPECT RATIO ADDITIVES ON MICROSTRUCTURAL AND MASS TRANSPORT PROPERTIES OF THE MICROPOROUS LAYER

Multiwall carbon nanotube (MWCNT) and graphene nanoplatelet (GNP) have been introduced to the conventional acetylene black (AB) microporous layer (MPL). Impact of the additives was evaluated in a bottom-top study from ink level to fuel cell performance level. Additives were employed in 5, 20, and 50% composites with AB. Rheological measurements suggested existence of larger agglomerates in the additive containing inks and a more compact microstructure for the pure carbon black ink. Surface quality of the MPLs was more affected by large particles of graphene, with 50% GNP as the extreme case. It was found that the unique microstructure created by synergy of AB and large aspect ratio particles can reduce both ohmic and mass transport resistances under dry and wet conditions. Critical loading of the additive was found to be 20% and the overall performance of MPLs with MWCNT was superior.

5.1 Experimental

5.1.1 Materials and processing

MPL inks were prepared by mixing desired amounts of carbon materials, 60 wt% PTFE suspension (DISP. 30, Chemours), and a surfactant containing solvent. The overall solid content and PTFE loading were kept constant at 8 wt% and 23 wt%, respectively. Multiwall carbon nanotube (MWCNT, Sigma Aldrich, D×L 110-170 nm × 5-9 µm) and Graphene nanoplatelet (GNP, Graphene Supermarket A-12) were each mixed with Acetylene Black (AB) to form composite powders of 5, 20, and 50% additive content. Water and surfactant as well as PTFE suspension were mixed by sonication for 2 minutes and added to the carbon powder in a 15 mL plastic jar containing 8 zirconia beads of 5 mm diameter. Ink components were mixed by a centrifugal ball milling mixer (Thinky-AR100) at the rotation rate of 2000 rpm for 10 minutes followed by 10 seconds of defoaming. A total of 7 samples was prepared as described in Table 5.1.

Table 5.1: MPL ink composition.

Sample	Carbon powder composition	Solid content (wt% of S.C.)	PTFE loading w.r.t the solid content (wt%)
100% AB	100% Acetylene black	8	23
5% MWCNT	5% MWCNT + 95% Acetylene black	8	23
5% GNP	5% GNP + 95% Acetylene black	8	23
20% MWCNT	20% MWCNT + 80% Acetylene black	8	23
20% GNP	20% GNP + 80% Acetylene black	8	23
50% MWCNT	50% MWCNT + 50% Acetylene black	8	23
50% GNP	50% GNP + 50% Acetylene black	8	23

Toray TGP-H-060 was impregnated with a diluted PTFE suspension of 5 wt% followed by drying at 10°C for 1 hour. MPL ink was coated on the impregnated carbon substrate using a Meyer rod. MPL loading had an average value of 1.78 ± 0.78 mg/cm^2 and the coating thickness, measured with a thickness gauge (Checkline), was found to be 25 ± 5 µm for all the samples. The sintering process to melt down PTFE and remove all surfactants was a multi step heat treatment at 300 and 380°C for 65 minutes, followed by slow cool down to the room temperature. Please refer to the reference [153] for more details.

5.1.2 Characterizations

5.1.2.1 Physical properties of carbon powders

Pure acetylene black, multiwall carbon nanotube and graphene nanoplatelet powders were degassed at 130°C to become fully dried before the measurement. Nitrogen physisorption test was performed at -196°C using a MicroMeritics TriStar II plus surface area and porosity analyzer. Isotherms collected at the relative pressure range of 0.060∼0.30 were subjected to the Brunauer–Emmett–Teller (BET) analysis to determine the specific surface area. Desorption section of the isotherm was used to evaluate average pore diameter and total pore volume via Barrett- Joyner–Halenda (BJH) analysis [154].

5.1.2.2 Particle size distribution and ink stability measurements

Dynamic light scattering (DLS) was used to estimate particle size distribution of the primary aggregate in the MPL inks. DLS analysis requires ink dilution for light transparency, free particle motion, and to avoid multiple scattering [155]. All samples were diluted to 0.02wt% concentration with the respective solvent. Diluted samples were sonicated for 10 minutes in a bath sonicator under low power. It is assumed that this treatment just breaks down the weak Van der Walls bonding between large agglomerates and cannot affect strong bonding of the primary aggregates [112]. Further, DLS measurement in this study is considered as qualitative analysis rather than quantitative due to its concentration limitation [57, 112]. DLS is expected to capture aggregates with a hydrodynamic diameter smaller than

1µm. Hence, large particles of the additives used in this study might not be detectable by DLS or particles might settle down [156]. To evaluate MPL ink stability, particle surface charge known as Zeta (ζ) potential was measured with DLS. ζ-potential can be calculated from particles mobility between two charged electrodes. Positive particles move toward the negative electrode and negatively charged particles move toward the positive electrode. Higher values of the absolute zeta potential indicate higher stability of a suspension [157]. Measurements have been performed in Malvern Zetasizer Pro, and at least three batches of each sample have been tested for data reproducibility.

5.1.2.3 Rheology

NETZSCH rotational rheometer equipped with a roughened 40 mm stainless steel parallel plate geometry was used for the rheological characterizations. MPL ink was loaded on the lower plate while the upper plate lowered down to the gap of 0.50 mm. Temperature was maintained at 25°C during all measurements. Rheological properties of dispersions depend on their microstructure. Thus, flow behavior under shear conditions can be representative of the ink microstructure. In this study viscosity versus shear rate is used to evaluate the general flow behavior of the samples. Further, a three-step shear rate condition, known as thixotropy, was employed to simulate coating condition for the MPL ink and study its microstructure before and after application of the shear force. Prior to all rheological measurements, sample was pre-sheared at 1 s^{-1} for 30 seconds followed by 2 minutes resting to remove any shear history from sample loading. Viscosity measurement was performed in a range of shear rates from 0.001-1000 s^{-1}. Thixotropy measurement was conducted in the following order 1) single shear rate of 0.001 s^{-1} for 1 minute to represent ink at the stationary condition, 2) Shear rate of 500 s^{-1} for 20 seconds to represent coating condition, and 3) shear rate of 0.001 s^{-1} for 10 minutes to evaluate microstructure's recovery in a wet thin film.

5.1.2.4 Surface roughness and electron microscopy

Stylus profiler (Bruker Dektak XT) equipped with a 2 µm probe was used for roughness evaluations. The measurement was performed at various locations of the GDM, and average roughness values are reported. To visualize MPL microstructure, scanning electron microscopy (SEM, Zeiss Gemini) have been performed on both surface and cross section of the GDM. Cross section samples prepared by dipping GDM in liquid nitrogen followed by freeze fracture.

5.1.3 Fuel cell testing

A commercially available Toray TGP-H-060 coated by MPL was used as the anode GDM in a single cell. The studied MPLs were placed at the cathode side to evaluate oxygen transport resistance and fuel cell performance. PTFE gaskets were used to avoid shorting between anode and cathode side and to avoid gas leak. Gasket thickness was controlled to compress GDMs to a strain of 22±1.5%. Commercially available MEA, consists of Nafion NR211 membrane and 0.30 mg/cm^2 of Pt/C loading on each side, was purchased from Ion Power, USA. Straight-parallel flow field, with a cell active area of 2 cm^2 was used to ensure low pressure drop and maintain uniform channel conditions [158].

An automated Greenlight G20 fuel cell test station was used for fuel cell testing. High frequency resistance (HFR) was measured through electrochemical impedance spectroscopy (EIS) using Gamry Reference 3000 with 30k Booster [159]. Ultra-high purity (99.999%) hydrogen, air, and nitrogen gases were used. The flow rates for anode and cathode side were maintained at 0.40 and 2.0 NLPM, respectively. Electrochemically active surface area of the MEAs was measured by H_2/N_2 Cyclic voltammetry (CV), and it was between 35-40 m^2/g_{Pt} for all the cells. Limiting current experiments [120, 160] were performed to measure the oxygen transport resistance (OTR) under both dry and wet conditions. For dry condition (80°C, 64% RH), the cell was operated at four different pressures: 100, 150, 200, 300 kPa, and oxygen dry mole fractions were varied from 1% to 4%. Under wet conditions (70°C, 80% RH, 300 kPa), there was a total of twelve oxygen dry mole fractions ranging between 1% to 21%. Finally, fuel cell performance was evaluated from steady-state polarization curves at 70°C under both dry (64% RH, 100 kPa) and wet (100% RH, 300 kPa) conditions. There was a potentiostatic hold of 10 minutes for recording the steady-state polarization data at each cell voltage.

5.2 Physical properties of carbon materials

Physical properties of the powders are reported in Table 5.2. MWCNT has the highest surface area followed by AB and GNP. A similar trend is observed for total pore volume of the powders, showing MWCNT has the largest pore volume. Considering the particle dimensions, the spherical AB could form much smaller pores compared to MWCNT and GNP [12, 68]. Thus, the composite MPL can take advantage of the hybrid microstructure formed by the synergy of carbon black and large aspect ratio particles [54].

Table 5.2: BET surface area, pore volume and average pore diameter of the raw carbon powders.

Sample	BET surface area (m^2/g)	BJH Total pore volume (cm^3/g)	BJH average pore diameter (nm)
Acetylene black	77.1	0.22	9.7
Multiwall carbon nanotube	111.6	0.55	16.1
Graphene nanoplatelets	44.2	0.15	11.6

5.3 Evaluation of the additive containing microporous layer ink

5.3.1 Ink stability and primary aggregate size distribution

Particle surface charge in a dispersion is an indicator of its stability and is quantified as ζ-Potential [111]. All MPL inks showed similar ζ-Potentials (Table 5.3), with an average value of -26.9 ± 1.5 mV, representing a relatively stable suspension [156].

Table 5.3: Average zeta potential of the studied inks.

Sample	Zeta Potential (mV)
100% AB	-26.9 ± 1.1
5% MWCNT	-25.9 ± 1.8
5% GNP	-26.2 ± 1.0
20% MWCNT	-28.4 ± 1.2
20% GNP	-28.7 ± 0.8
50% MWCNT	-27.5 ± 0.9
20% MWCNT	-24.4 ± 0.3

Particle size distribution of 100% AB compared to its composites with MWCNT is shown in Figure 5.1(a). As mentioned before, there is a size and stability limitation of large aspect ratio particles for DLS measurements. Therefore, a major population of large agglomerates might not be captured in the DLS results. By increasing MWCNT, the ink shows a wider particles size distribution, suggesting existence of agglomerates of various size. The first peak of 20 and 50% MWCNT samples has particle size around 120 nm while the 100% AB has a peak value around 350 nm. This indicates that even smaller carbon black agglomerates could form in mixing with a high aspect ratio carbon. This behavior has been reported for non-aqueous systems, with silica as the spherical particle mixed with additives of GNP and CNT [136]. For CNT, winding effect was introduced as the root cause of the formation of wide agglomerate size of the spherical particle [136]. Figure 5.1(b) compares DLS results for 100% AB versus its composites with GNP. The GNP particles used in this study are above 5 µm, which is out of range for DLS measurements [156]. Hence, the DLS results are close to the 100% AB ink with slightly wider distribution toward smaller particle in the GNP-AB mixture. This suggests formation of smaller AB agglomerates in presence of GNP compared to 100% AB ink.

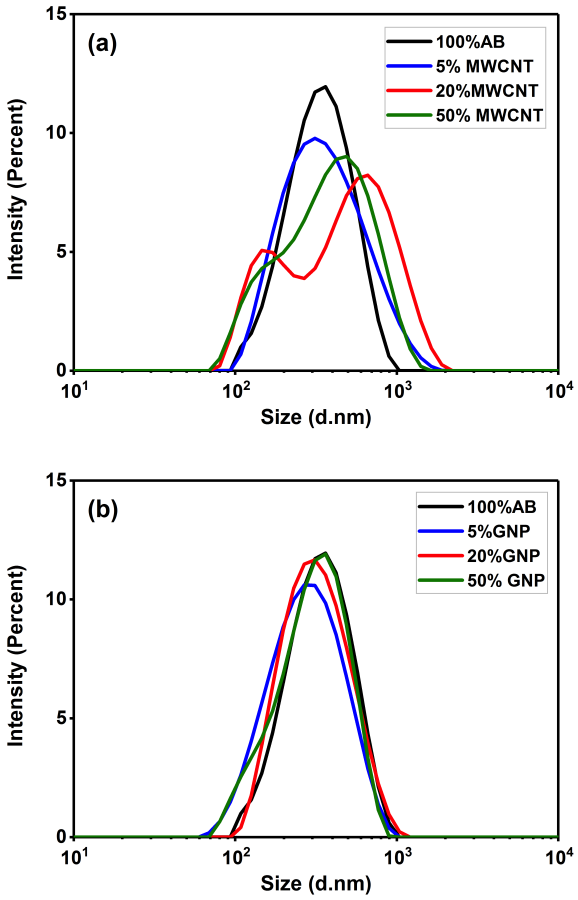

Figure 5.1: Particles size distribution of diluted inks of (a) acetylene black and multiwall carbon nanotube, and (b) acetylene black and graphene nanoplatelet.

5.3.2 Steady flow behavior

General flow behavior of the MPL inks is shown in Figure 5.2. Ink's total carbon content was fixed in the sample design to capture the effect of additives and avoid any change in the solid content. Major change in solid content significantly impacts rheological properties of the suspensions and could hinder the real microstructural properties related to particle aspect ratio, which is the target of this study. All inks showed a three regional flow, consisting of a shear thinning at lower shear rates followed by a transient shear thickening at intermediate shear rate and ended with a second shear thinning flow. This behavior is typical of fractal shaped carbon black agglomerates and still existed in the composite ink. The average viscosity of samples in low shear rate region (shear rate $< 10\ s^{-1}$) is calculated and summarized in Table 5.4. 5% additive containing samples are expected to show close rheological properties to 100% AB ink. However, the low shear viscosity of 5% MWCNT and GNP is smaller than 100% AB. This trend changes with adding more additives to the

ink and the average low shear viscosity of 20 and 50% additive containing inks is higher than 100% AB. This behavior is due to the existence of much larger agglomerates in those inks and the extreme case is 50% GNP. The flow behavior of the 50% GNP ink is not ideal for coating; however, it is studied as an extreme case to evaluate the capacitance of MPL for additive content and how its microstructural and surface properties can impact its role as a diffusion media in the fuel cell.

Table 5.4: Average low shear viscosity of the studied MPL inks, reported values are calculated from shear rate 0.001-10 s^{-1}.

Sample	Average low shear viscosity (Pa.s)
100% AB	154.4
5% MWCNT	94.3
5% GNP	86.4
20% MWCNT	282.5
20% GNP	178.5
50% MWCNT	574.0
50% GNP	1200.0

The onset of the transient shear thickening (shown by dashed line in Figure 5.2) is occurred at a similar shear rate for 100% AB and 5% additive containing samples, indicating dominance of carbon black in the microstructural evolution of these samples. The rise in viscosity occurs as a result of dominance of hydrodynamic forces, which brings the particles close to each other and trigger re-agglomeration [55, 126, 131, 132]. These temporary formed agglomerates break down by further increase of the shear force and a second shear thinning appears. From Figure 5.2(b) and (c), it can be seen that the onset of the transient shear thickening shifts slightly by adding more MWCNT to the ink. On the other hand, the shift is considerably significant for GNP containing samples due to the necessity of higher hydrodynamic forces to bring large agglomerates of GNP or GNP-AB close together. This behavior was also observed in a mixture of activated carbon and GNP, used in capacitive flowable electrodes [129]. Overall, GNP has a more significant effect on the general flow behavior of the composite MPL ink, which at least affects the coating quality and surface roughness of the final MPL.

Slope of shear thinning in the low shear rate region can be quantified with a power law fit and is known as flow index. Flow index below 1 represents a shear thinning material, and the lower it gets the higher is the extent of shear thinning [115]. The calculated values of flow index are shown in Figure 5.3. 100% AB has a more negative flow index than the 5% additive containing samples, indicating existence of larger agglomerates in its ink. 5% MWCNT or 5% GNP might not be high enough to result in formation of large agglomerates of these additives.

On the other hand, DLS results showed that in presence of these additives smaller aggregates of carbon black can be formed. At 20% and 50% MWCNT concentration, the flow index increases significantly due to formation of large entangled MWCNT agglomerates. Effect of GNP on flow index of the ink increases by increasing its concentration. This behavior dictates that the microstructure of the additive containing inks is more agglomerated than the pure Acetylene black ink.

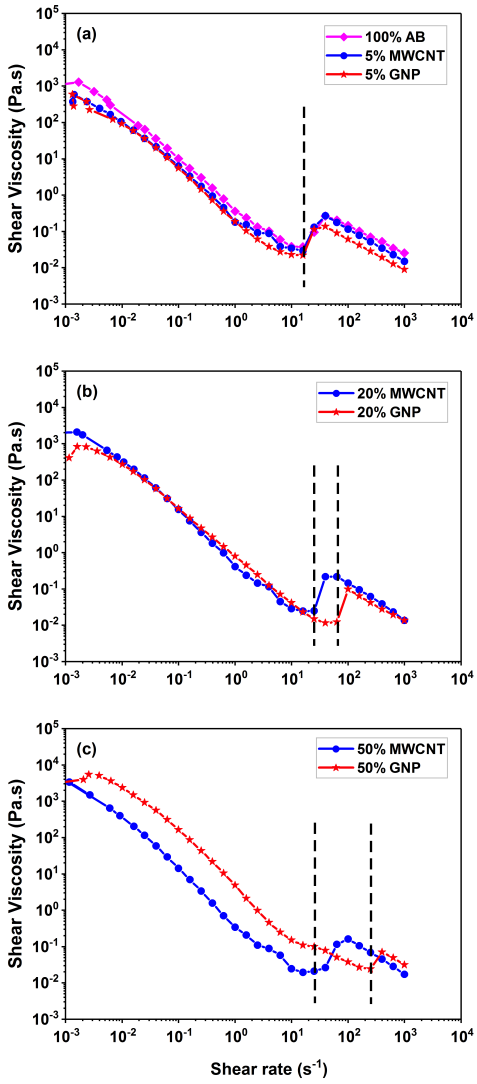

Figure 5.2: Viscosity versus shear rate for (a) 100% AB and 5% additive containing MPLs, (b) 20%, and (c) 50% additive containing MPL inks.

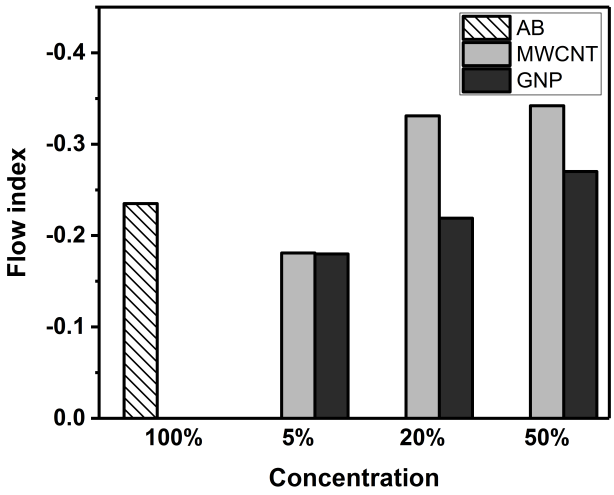

Figure 5.3: Flow index calculated from the fit to the low shear viscosity plots.

5.3.3 High shear flow behavior and ink recovery

Coating process takes place under high shear rates that can influence properties of viscoelastic materials like carbon based slurries. Thixotropy test offers a three-step shear ramp up and down, which allows imitating real coating condition for the ink. Pre-coating condition is assumed as a low shear state for the ink, so its viscosity was monitored at shear rate of 0.001 s^{-1} for 1 minute. Then shear rate ramped up to 500 s^{-1} for 20 seconds to evaluate microstructural evolution under high shear force condition of the coating process. As shown in Figure 5.4, at high shear stage, viscosity drops due to the agglomerate break down and its alignment with the direction of shear force. In the third stage, shear rate was ramped down back to 0.001 s^{-1} to monitor ink's microstructure recovery after coating as a wet thin film. For all samples, the viscosity at the third stage settled at a higher value compared to the first stage. This behavior is as a result of structure built up over time and was observed previously for MPL inks with spherical acetylene black particles [153]. The period when viscosity at third is recovered above 90% of its value at the first stage, is considered as the recovery time. It is calculated by dividing viscosity at time t of the third stage by the average viscosity of the first stage. From Figure 5.5(a), 100% AB revealed the fastest recovery time indicating its fast agglomeration kinetics. This fast agglomeration resulted in higher amount of shear thickening as presented by relative viscosity of the third phase compared to the first phase (Figure 5.5(b)). Microstructure recovery of non-Newtonian suspensions depends on the solid content and particle morphology [129]. In this study, solid content is fixed, so the difference in recovery time should stem from the particle geometry. Additive containing inks showed above 80% higher recovery time than 100% AB. This behavior is attributed to the slow aggregation kinetics of large particles like MWCNT and GNP [129]. 20% MWCNT

showed faster recovery compared to the respective GNP ink (Figure 5.5(a)), which resulted in larger relative viscosity for this sample (Figure 5.5(b)). This behavior has been reported previously and described as carbon nanotubes act like wires that connect agglomerates of AB together and strengthen the microstructure [54, 131, 161]. On the other hand, at high concentrations of MWCNT, like 50% the nano wires become too entangled that can break the connection of AB agglomerates and decrease the rigidity of the microstructure [54] as shown by lower relative viscosity for 50% MWCNT in Figure 5.5(b). 50% GNP is high enough that the big agglomerates of GNP affected the bulk viscosity and resulted in higher relative viscosity for this sample.

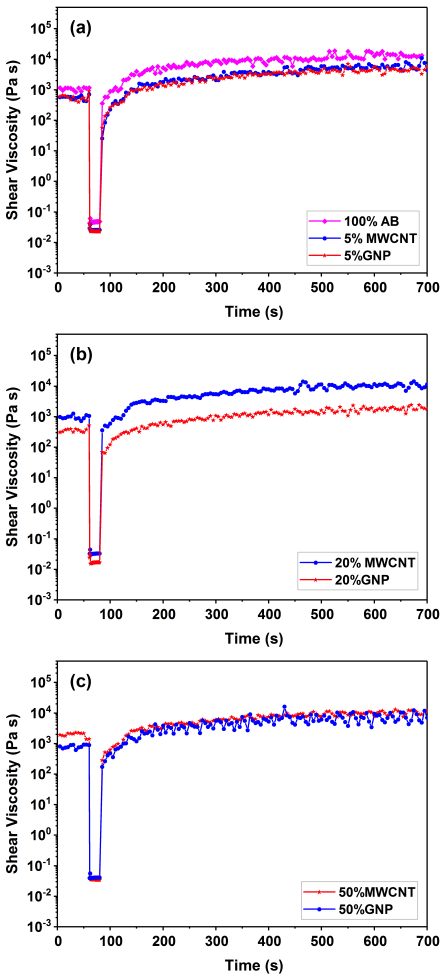

Figure 5.4: Three-step shear rate viscosity versus time, (a) 100% AB and 5% additive containing MPLs, (b) 20%, and (c) 50% additive containing inks.

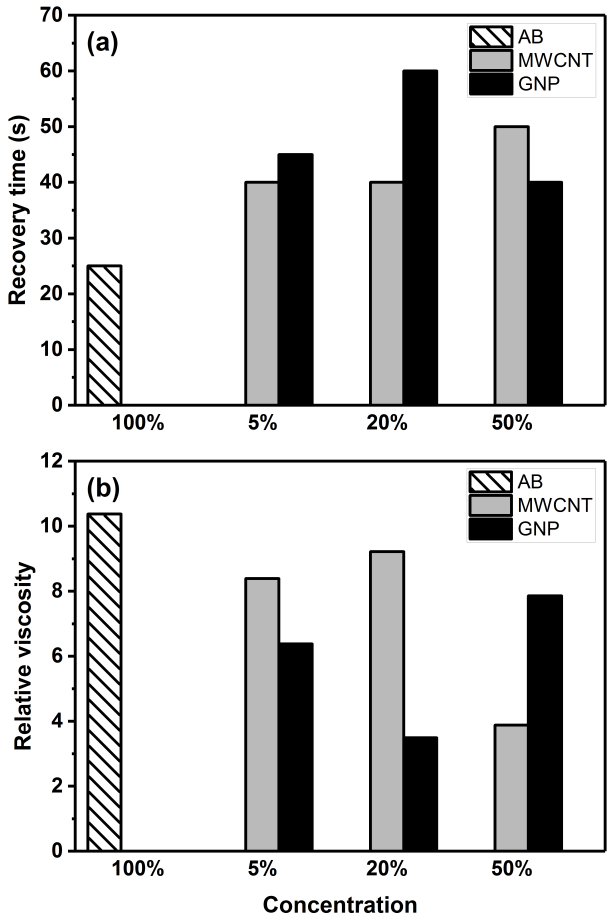

Figure 5.5: Three-phase rebuilt (a) recovery time after removal of coating shear force and (b) Viscosity in third phase relative to the first phase.

5.4 Performance of microporous layer with conductive additives

5.4.1 Coating quality and microstructure

Surface SEM images of the MPLs are shown in Figure 5.6. Comparing 100% AB MPL (Figure 4(a)) with its MWCNT composites (Figure 5.6(b-d)), crack width increases by increasing MWCNT concentration. Wide cracks in a specific composite of AB-MWCNT was reported by Lee at al. [66]. Figure 5.6(e) shows large agglomerates of entangled MWCNT and AB at 50% MWCNT concentration. This agglomerates surface quality is not desired for an optimum MPL-Catalyst layer interface. Some studies reported MWCNT concentration of 50% and above as the optimum composite MPL [72, 162]. However, the studied inks were very diluted and not applicable to all coating methods. In this study, MPL ink solid content is 8 wt%, which gives reasonable viscosity for blade coating on a rough substrate to reach a reasonable thickness. From Figure 5.6(e-f), it can be seen that at concentrations above 20% GNP, the MPL surface becomes rough, and the extreme case is the 50% GNP.

Yoshimune et al. [64] reported rough texture of a mixture of AB and graphite in 1:1 volume ratio. In Figure 5.6(f) a close look of the texture of the 50% GNP is shown. It seems that AB is attached to the surface of GNP and its large 2D surface area served as a nucleation site for the spherical particles [79]. In a study of Mariani et al. [79] similar rough surface for large particles of GNP have been found and using smaller graphene nanoplatelet was recommended for better surface features.

Cross section SEM images are shown in Figure 5.7. Clearly, 100% AB, as showin in Figure 5.7(a), has the most compact microstructure, which was also inferred from its precursor ink rheological behavior. 100% AB ink had the highest relative viscosity and the shortest recovery time in the Thixotropy measurements, indicating properties of a compact microstructure. 5% additive containing samples, as shown in Figure 5.7(b) and (e), showed relatively close microstructure to the 100% AB. However, the presence of high aspect ratio particles seems to provide some larger pores compared to the pure AB system. Increasing the additive content to 20%, resulted in creation of larger pore in both MWCNT and GNP composite MPLs. Increase in the mean pore size by adding large aspect ratio carbon particles to the carbon black have been reported in other studies [64–66, 71–73, 78]. Presence of a variety of pore size in the MPL provides the opportunity of separate pathways for water and gas transport, which is proposed to improve fuel cell performance [45, 62, 64]. One noticeable microstructural feature is nucleation of AB particles on the large surface area of GNP to form regular carbon black clusters (Figure 5.7(e-g)) [79]. Further, strong van der walls force between AB and MWCNT proposed by Vivekanand et al. [163] and findings of Lee et al. [66] suggest higher attraction force between MWCNT and AB rather than AB particles. Carbon nanotubes also interconnect AB (Figure 5.7(c)) particles and could potentially increase mechanical integrity of the microstructure up to a certain concentration [54]. Regarding the 50% additive samples, the large agglomerates of high aspect ratio particles dominated the microstructure. As a result, for the 50% GNP large macroscopic pores can be seen while in the 50% MWCNT high level of nanotube entanglement is achieved.

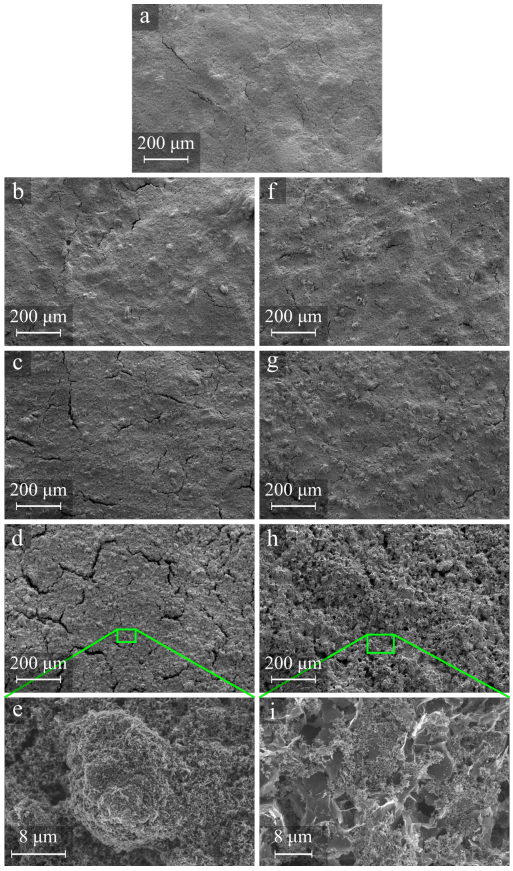

Figure 5.6: Surface SEM images of (a) 100% AB, (b-d) 5, 20, and 50% MWCNT, (f-h) 5, 20, and 50% GNP. High magnification images of agglomerates in (e) 50% MWCNT and (i) 50% GNP.

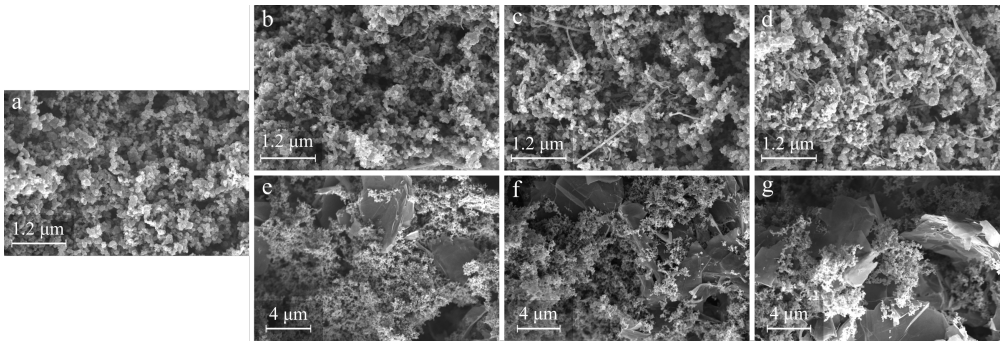

Figure 5.7: Cross section SEM images of the (a) 100% AB, (b-d) 5, 20, and 50% MWCNT, (e-g) 5, 20, and 50% GNP.

5.4.2 Surface roughness

Surface profile of the MPLs are shown in Figure 5.8(a-c). Average roughness values were measured in several scans and reported in figures 5.8(d) and (e). Overall, the average

surface roughness is close for all samples, except for the 50% GNP. Adding 5% additive slightly reduced surface roughness. Rougher surface profile for pure carbon black MPL was reported by Leeuwner et al. [80]. The surface profile of the MPL with 20% additive content shows properties of an agglomerated surface. For 50% MWCNT the profile shows deep valleys indicating existence of cracks, while for the 50% GNP it could stem from both cracks and large agglomerates. It should be noted that high roughness of the 50% GNP can result in water accumulation at the interfacial voids between the MPL and catalyst layer [79, 164, 165].

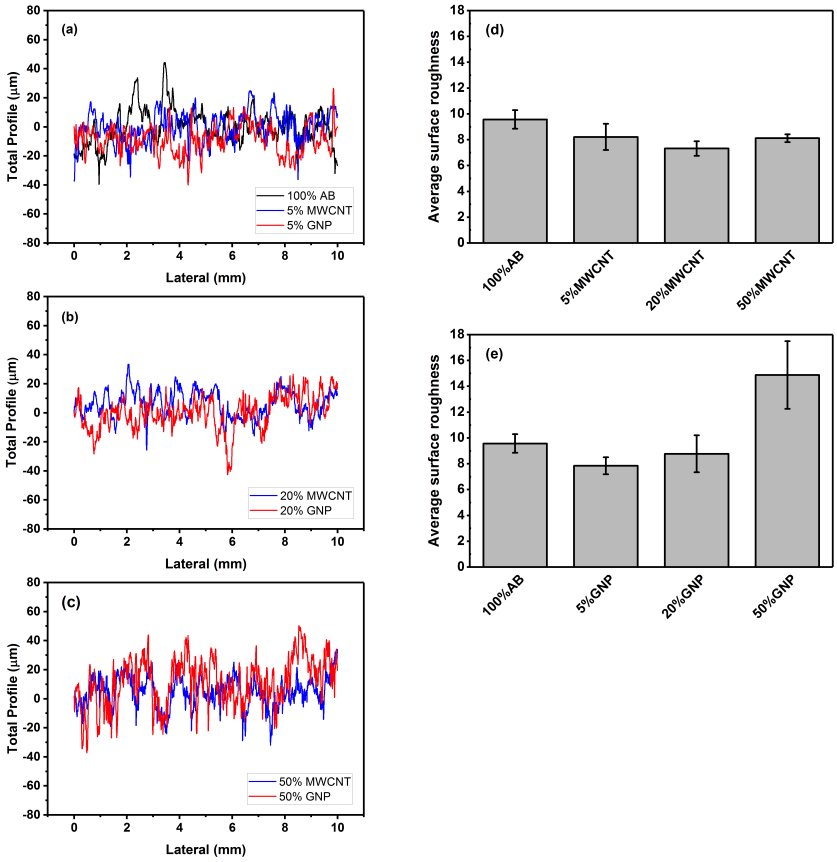

Figure 5.8: (a-c) Surface profile of the MPLs, and average surface roughness for (d) MWCNT and (e) GNP containing MPLs.

5.4.3 Gas transport properties

Limiting current experiments were performed to evaluate oxygen transport resistance (OTR) under dry and wet conditions. The theory and results are provided in the supplementary information. Channel resistance was subtracted from the total OTR to obtain a plot of diffusion media + electrode OTR versus cell operating pressure, as shown in Figure 5.9(a and b). Slope of the dry limiting current data is proportional to the ratio of nominal diffusivity

to effective diffusivity, D/D_{eff} , which is pressure dependent [107]. The intercept represents the pressure independent oxygen transport resistance. Since similar electrode with reliable data reproducibility is used in this study, it is assumed that any change in the pressure independent OTR (R_{others}) can be attributed to the Knudsen diffusion in small pores (below 50 nm in size) of the MPL [109, 122].

From Table 5.5, it can be inferred that the D/D_{eff} is quite close for all GDMs since all cathode diffusion media had been fabricated from a similar macroporous substrate (Toray TGP-H-060). Significant variation in pressure independent OTR, R_{others}, can be observed among the samples. Addition of MWCNT $\leq 20wt\%$ resulted in the formation of effective larger pore sizes and consequently lowering the R_{others}. Park et al. [67] reported higher values of air permeability for MPLs of carbon nanofiber and Vulcan compared to the pure carbon black. In their study, the highest air permeability was for the 25% CNF containing MPL. In this study, both 5% and 20% MWCNT samples have lower R_{others} than 100% AB. However, increasing the concentration of MWCNT to 50% resulted in the formation of large entanglements (Figure 5.9(a)) and consequently increasing the R_{others}. On the other hand, GNP only at the concentration of 20% resulted in lower R_{others} for the corresponding diffusion media. One possible reason is that the 20% GNP sample has more cracks compared to the 5% sample, while its microstructure is less compact than the 50% GNP. GNP particles can have two fold effect on the microstructure: (i) the platelets tend to stack up, which creates a compact structure, (ii) particle geometry can allow formation of large pores [78, 80]. Thus, in terms of gas transport resistance, there would be a trade-off between blockage of the large GNP stacks or transport through the large pores created by the particle geometry.

Table 5.5: Oxygen transport properties under dry condition.

Sample	Dry D/D_{eff}	R_{others} (s/cm)
100% AB	4.4 ± 0.1	0.42
5% MWCNT	4.4 ± 0.1	0.33
5% GNP	4.7 ± 0.1	0.46
20% MWCNT	4.3 ± 0.1	0.27
20% GNP	4.5 ± 0.1	0.25
50% MWCNT	4.1 ± 0.1	0.57
50% GNP	4.3 ± 0.1	0.42

Figure 5.9(c,d) represent the total OTR as a function of limiting current density obtained by varying oxygen dry mole fractions under wet operating conditions. Since current and water generation are intrinsically linked, the change in the oxygen transport resistance at high current densities can be considered as a function of water generation in the cell. The three regional trend of OTR versus limiting current density matches well with standard observations for Toray TGP-H-060, where a dry (≤ 0.65 A/cm^2), transition (ca. 0.65$\sim$1.75

A/cm^2), and wet ($\geq$ 1.75 A/cm^2) region exists [121]. Under wet conditions, the porosity of the DM is decreased, and the tortuosity is increased. In addition, the oxygen molecules need to travel through the liquid water present at the interface between MPL and catalyst layer to reach the triple-phase boundary. Hence, the OTR is increased with the presence of the liquid water at higher oxygen dry mole fractions, or at high limiting current densities.

From Figure 5.9(c), it is found that the dry region is consistent with the corresponding dry limiting current results for 100% AB and MWCNT containing MPLs (Figure 5.9(a)). In the wet region, where high amount of water generation is expected, 5 and 20% MWCNT diffusion media showed the least OTR. Further, these samples show a plateau in their ORT suggesting formation of efficient water pathways [121]. Both 5 and 20% MWCNT samples showed properties of a less compact microstructure compared to 100% AB, and as a result, preferential water pathways in large pores could be a reason for the low OTR at high current densities. On the other hand, the 50% MWCNT showed properties of highly entangled microstructure because of the nanotube bundles. This microstructure had a high dry OTR which clearly gets worse when it comes to two-phase transport in presence of liquid water. Thus, the 50% MWCNT had a relatively large wet OTR.

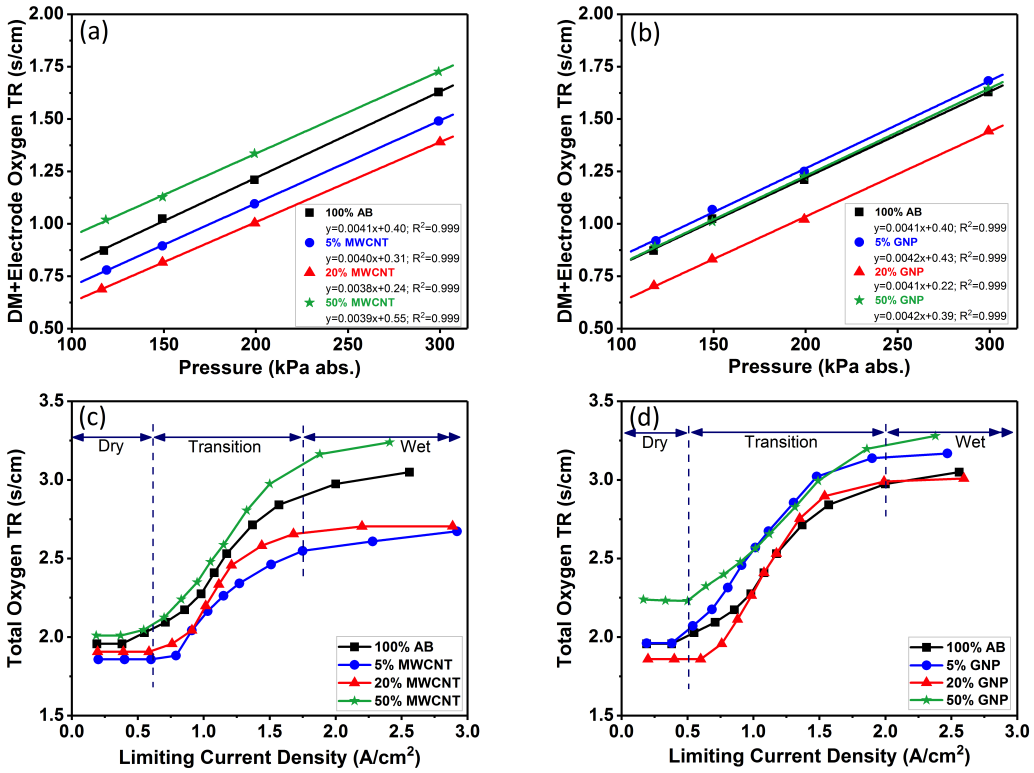

Figure 5.9: Diffusion media and electrode oxygen transport resistance as a function of pressure under dry condition (80°C, 64% RH) for (a) MWCNT and (b) GNP additives. Total oxygen transport resistance as a function of the limiting current density under wet condition (70°C, 80% RH, 300 kPa) for (c) MWCNT and (d) GNP additives.

Wet limiting current result for GNP containing MPL is presented in Figure 5.9(d). 20% GNP revealed the most efficient water management among other GNP containing diffusion media. The wet OTR for 20% GNP is relatively close to 100% AB. However, the wet region plateau for 20% GNP was formed faster (at lower current density) than 100% AB, which implies less oxygen transport resistance in this sample. 5 and 50% GNP containing MPLs showed properties of water accumulation in the pores that resulted in high OTR. 5% GNP had a high dry OTR that clearly can lead to much difficult oxygen transport in presence of liquid water. Regarding the 50% GNP, the OTR in the transition region has a relatively high slope indicating fast water accumulation in the pores. 50% GNP had a very rough surface and water accumulation at its interface with the catalyst layer is expected [79, 164, 165]. Also, from SEM images, it was observed that carbon black tends to nucleate on the surface of GNP to form agglomerates. This means that the small pores of carbon black are effectively blocked by the GNP support and 50% might be a very high extreme as an additive in the MPL.

5.4.4 Fuel cell performance

Fuel cell performance was evaluated under both dry and wet conditions, as shown in Figure 5.10. Three regions can be observed in the $i - V$ curve: activation/kinetic, ohmic, and concentration/mass transport. The activation region for all samples shows no significant variations from each other since similar MEA assemblies were used for all experiments. Under dry condition, samples with 20% additive content showed significantly lower ohmic overpotentials (Figure 5.10(a) and (b)). This behavior indicates that these diffusion media provided a condition of better electron and ion transfer, which is also supported by the electrochemical impedance spectroscopy (EIS) measurements presented in Figure 5.11. Reduction in the ohmic resistance could be via improvement in the electrical conductivity or better reactant gas supply to the catalyst layer. Inherent high electrical conductivity of MWCNT and GNP is well known and lower in-plane resistivity has been reported for MPLs prepared with these materials [65, 76, 78]. However, the measured high frequency resistance (HFR) is not as significant as the observed improvement in the ohmic resistance for 20% additive samples. Dry limiting current tests revealed lower non-Fickian OTR for the 20% additive samples, which agrees with the improvement in both ohmic and mass transport regions of these samples and implies better charge transfer as a result of improvement in gas supply [76].The results of lower ohmic resistance may be attributed to lower interfacial contact resistance of the 20% additive containing samples. [80, 166]. Adding MWCNT to the MPL even by 5% could significantly improve oxygen transport due to the existence of large pores. In the case of GNP additive, the mass transport improvement is mainly observed at 20% concentration.

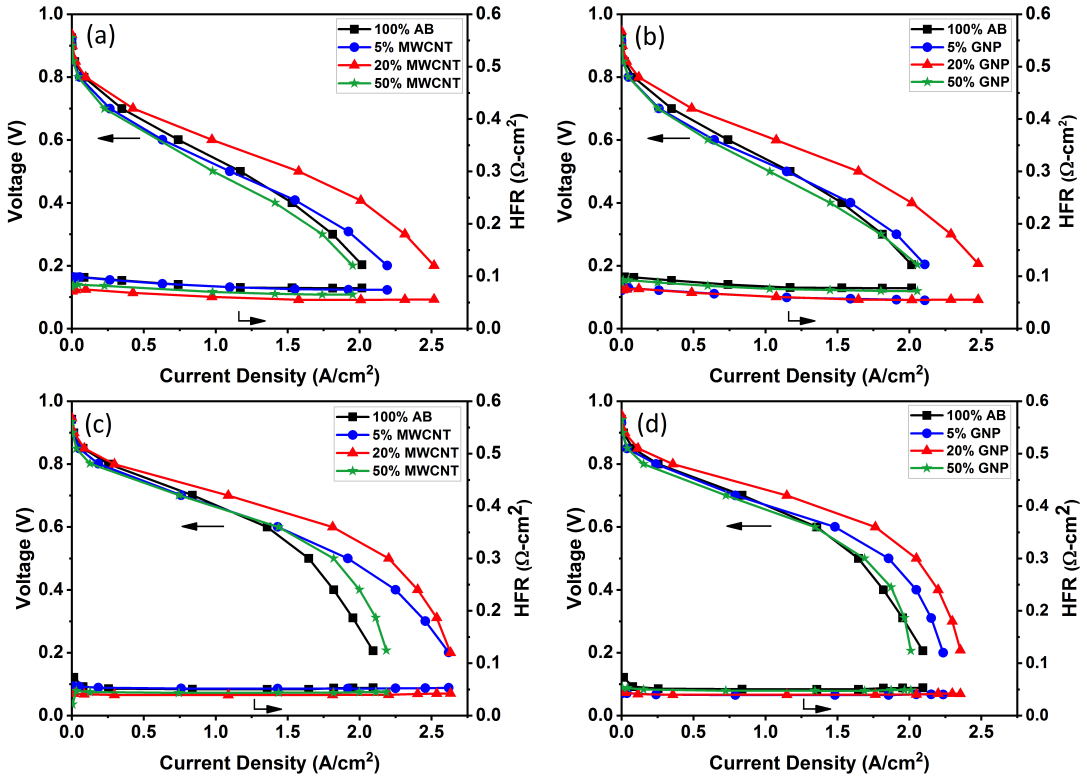

Figure 5.10: Steady-state polarization under dry condition (70°C, 64% RH, 100 kPa) for (a) MWCNT and (b) GNP additive containing diffusion media. Steady-state polarization under wet condition (70°C, 100% RH, 300 kPa) for (c) MWCNT and *d) GNP additive containing diffusion media.

The ohmic resistance under wet condition is lower as compared to the dry condition due to the higher membrane hydration. 20% additive containing samples showed significant improvement in the ohmic region performance, which is also shown by lower impedance in the EIS measurements (Figure 5.11(c) and (d)). In terms of water management in the mass transport region, all MWCNT containing diffusion media performed better than the 100% AB. Up to 20% MWCNT content improved water management and this property was reduced by increasing the concentration to 50%. These results agree well with the wet limiting current data confirming mass transport is the dominant effect. GNP content below 20% improved mass transport resistance compared to the pure AB MPL. Lower performance of the 50% GNP potentially stems from water accumulation in the compressed stacks of GNP [80] as suggested by the wet limiting current results.

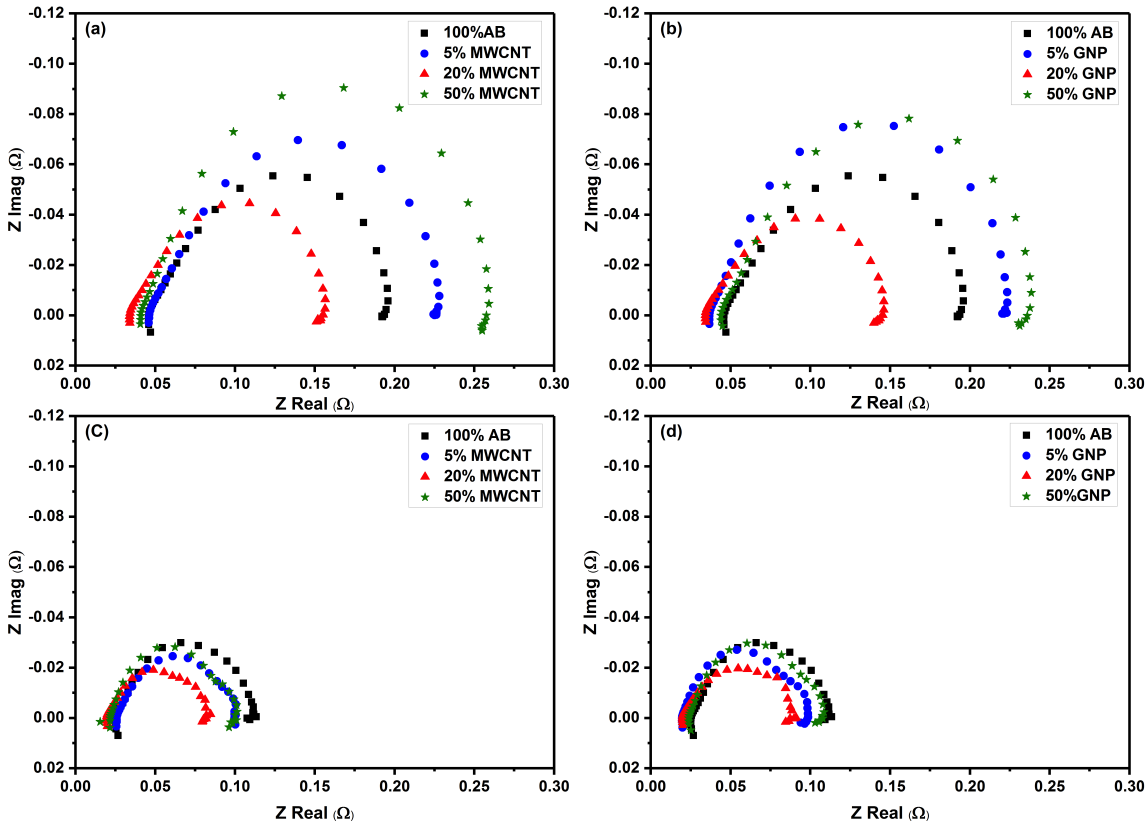

Figure 5.11: EIS measurements at 0.70 V under dry condition (70°C, 64% RH, 100 kPa) for (a) MWCNT and (b) GNP, and under wet condition (70°C, 100% RH, 300 kPa) for (c) MWCNT and (d) GNP.

In addition, the cell performance was also studied by sweeping the relative humidity between 40% RH to 100% RH at 0.30 V, as shown in Figure 5.12. For all samples, performance kept increasing till 80% RH. Performance started to drop as soon as full humidified (i.e., 100% RH) condition was reached due to the water accumulation in the pores. For fully humidified condition and low cell-voltage operation, 5% CNT sample is preferred to be used to the 20% CNT sample.

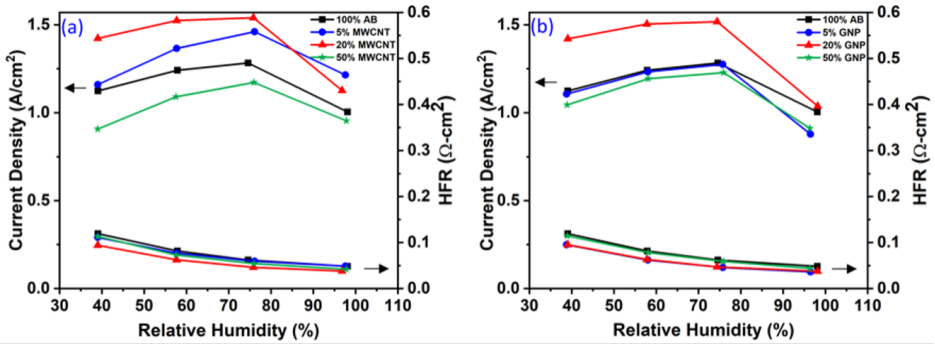

Figure 5.12: RH-Sweep from 40% RH to 100% RH at 80°C under 10-minutes potentiostatic hold at 0.30 V for (a) MWCNT and (b) GNP samples.

5.5 Conclusions

Synergistic effect of incorporating large aspect ratio carbon particles (MWCNT and GNP) in conventional acetylene black (AB) based microporous layer have been studied on the microstructure and mass transport properties of the resulted diffusion media. Other than composite carbon mixtures, all ink variables like solvent, carbon/solvent ratio, and solid content were similar for the studied samples. DLS measurements have shown a relatively stable ink for all composition and bimodal particle size distribution for additive containing samples. Particle size distribution suggested smaller agglomerates of carbon black could form in mixing with large aspect ratio particles. For MWCNT winding effect could be a potential cause of break down of large carbon agglomerates and for GNP, nucleation of carbon black on the graphene platelets.

Three regional flow behavior consists of an overall shear thinning behavior with a transient shear thickening interval was observed for all of the MPL inks. Low shear viscosity of the inks with low additive content (5 wt%) was slightly lower than 100% AB ink. However, by increasing additive content ($\geq$ 20 wt%) viscosity increased due to the existence of large agglomerates in the ink. 50 wt% GNP content with the highest low shear viscosity found to be not suitable in terms of coating quality on a rough carbon fiber surface. Transient shear thickening region was shifted toward higher shear rates by increasing GNP content, suggesting existence of very large agglomerates that needs higher shear force to be broken down. This behavior was less noticeable for MWCNT, which from ink quality perspective gives more bandwidth to use larger amounts of this additive in the ink.

By Comparing relative viscosity before and after applying a high shear force (equivalent to the coating process) it was found that additive containing samples have slower microstructural recovery due to the slower agglomeration kinetics of large additive particles. On the other hand the relative viscosity in the recovery stage was higher for 100% AB ink

suggesting a more compact carbon network as a result of its fast re-agglomeration kinetics. Both rheological results and SEM observations from surface and cross sections confirmed that 50 wt% additive content would end up in low coating quality and very entangled microstructure. On the other hand additive content below 20 wt% results in a microstructure with both properties of large pores (from large additives particles) and small pores (from AB particles).

Oxygen transport resistance (OTR) was evaluated through dry and wet limiting current measurements. MWCNT containing samples at both 5 and 20 wt% content reduced OTR, while just the 20 wt% GNP showed similar effect. Under wet condition, samples with MWCNT$\leq$20 wt% showed both lower OTR and indicators of efficient water pathways formation compare to the 100% AB sample. In case of the GNP containing diffusion media, only the 20% GNP sample was resulted in formation of efficient water pathway. However, the OTR was close to the 100% AB diffusion media. Fuel cell performance results revealed a higher performance under both dry and wet condition for 20% additive content of both MWCNT and GNP as well as 5% MWCNT. The observed improvement for 5% MWCNT was limited to high current densities but for 20% additive containing samples both ohmic and mass transport overpotentials were lower. This behavior stemmed from lower OTR of the 20% additive containing samples, which results in overall better gas supply to the catalyst layer.

Chapter 6

AN INVESTIGATION ON INTERPARTICLE INTERACTIONS IN THE CATALYST INK AND ITS IMPACT ON ELECTRODE NETWORK FORMATION

Understanding complex interparticle interactions in the catalyst ink requires direct assessment of the formulation's effect on the resulting interactions. The ionomer/carbon ratio is one design parameter that can alter catalyst layer microstructure. There is a lack of direct evidence of the effect of I/C ratio on the bulk response of the Pt/C-ionomer network. Hence, this study proposes a novel methode to understand interactions in the ink and ionomer coverage via the microstructure response to the external mechanical and alternative current perturbation. Therefore, a combination of rheology and conductivity evaluations of the catalyst ink is used as direct evidence of the agglomerated network's properties. The findings are supported by cryo-TEM imaging and in-situ fuel cell characterizations. It was found that I/C=0.75 is the critical amount below and above which very different configuration and ionomer coverage can be expected in the catalyst layer.

6.1 Experimental

6.1.1 Sample preparation

Desired amount of 40% Pt/C(Johnson Matthey HiSPEC 4000) catalyst powder and ionomer dispersion (D2020, 1000 EW at 20 wt%, IonPower) were mixed in a water-IPA solvent (IPA/Water=0.3) to prepare catalyst inks. In this study, carbon to solvent ratio was fixed at 0.06 to eliminate the effect of solvent-carbon interaction and narrow down the focus of the study to the ionomer-carbon-catalyst interactions. Five levels of Ionomer/carbon ratio (0,0.25,0.5,0.75, and 1) were chosen to deconvolute interparticle interactions and cover the typical range of I/C targeted in recent studies. Ionomer dispersion and solvents were mixed in a vial using bath sonication and then added to the catalyst powder in a plastic jar with eight zirconia beads of 5mm diameter. Liquid and solid components were mixed via centrifugal ball milling (Thinky mixer) at 2000 rpm for 3 minutes. I/C=0 and 0.25 are not very practical for fuel cell application, but they were chosen to better clarify role of ionomer in the microstructure formation of catalyst ink and catalyst layer. Thus, just the samples

with I/C=0.5,0.75, and 1 were subjected to further fuel cell testing. To prepare membrane electrode assemblies, catalyst ink was coated on a virgin PTFE substrate and air dried. The catalyst layer was then transferred to a Nafion 211 membrane (Ion Power) via hot pressed decal transfer at T=132 °C and P=300 Psi.

6.1.2 Rheology and Rheo-Impedance

Viscosity measurements were carried out using the NETZSCH Instruments. Rheometer with standard roughened parallel plate geometries (40 mm diameter). The instrument was adapted to in-house geometries for simultaneous rheological and electrochemical impedance spectroscopy measurements. Part drawings are presented in A.1. The in-house geometries were insulated from the rheometer's body to enable parallel rheological and impedance measurements. Schematics of the resulted setup is shown in Figure 6.1. Upper and lower geometries (40mm diameter) were machined from a 304 stainless steel rod followed by surface sandblasting A.2 to provide reasonable surface roughness and impede particle slip during the applied shear force. The upper plate rotates, and the lower plate is stationary. A Teflon attachment was used to insulate the upper plate from the rheometer's body (Figure 6.2a), which was proven to provide reasonable alignment. For maintaining electrical connection to the upper geometry with minimum friction, a liquid metal (Gallium Indium Eutectic, EGAIN,Sigma Aldrich)[167] was used in the solvent trap attached to the upper geometry. A stainless steel needle was dipped into the solvent trap and connected to the power supply (CH Instrument 750E). Further calibration results indicated that this assembly provides reasonable electrical connection and has low friction, not interfere with the applied torque from the rheometer. The lower stainless steel plate was attached to a peak geometry for electrical insulation. Therefore, the metallic upper and lower geometries were the two electrodes with catalyst ink as the electrolyte between them. Figure 6.2b shows the entire setup and connections.

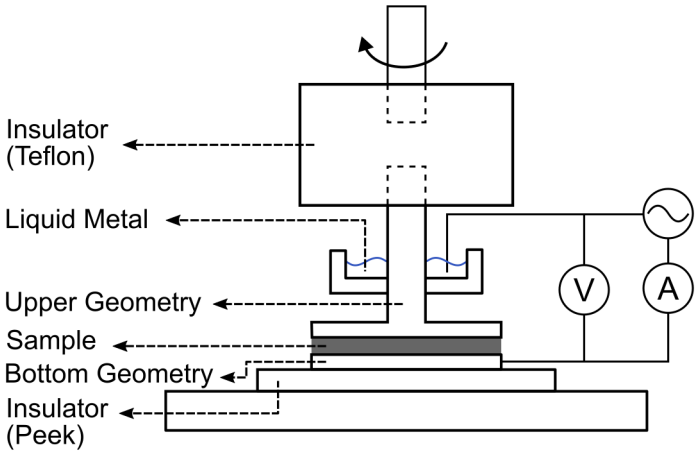

Figure 6.1: Schematics of the Rheo- Impedance setup consisted of two metallic geometris, one solvent trap containing liquid metal and two electical insulation from the upper and lower body of the Rheometer.

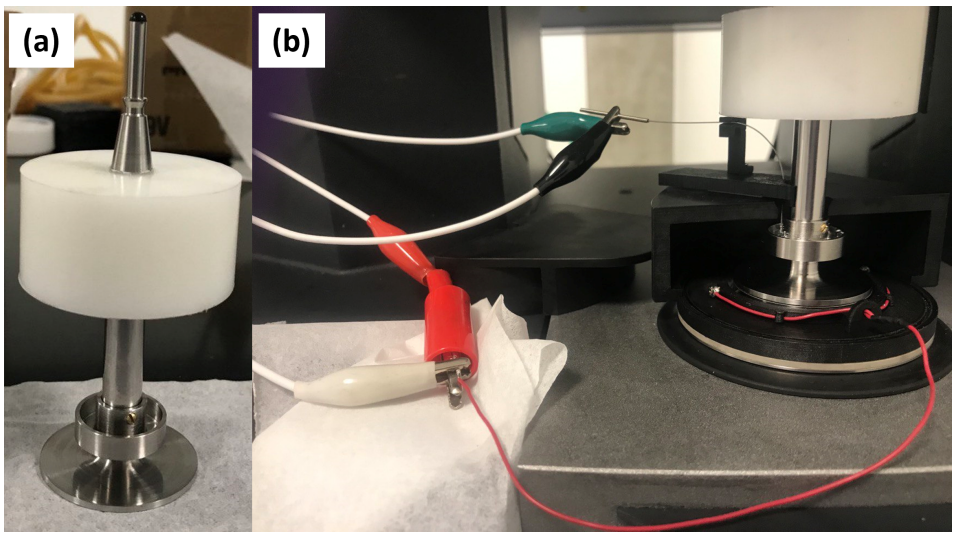

Figure 6.2: a) Upper geometry electrically insulated from rheometer's body, and b) Rheo-Impedance setup with all connections.

6.1.2.1 Rheo-Impedance setup calibration

Due to the drastic changes in the in-house setup compared to the standard geometries, it was necessary to ensure mechanical stability and accuracy of the applied shear forces to the sample. Therefore, a Newtonian standard calibration oil with a known viscosity was tested in the setup for the desired range of shear rates. As shown in Figure 6.3 the setup could perfectly and accurately pass the standard oil test. The working gap between geometries was 0.3mm, which is aimed for the catalyst ink characterizations.

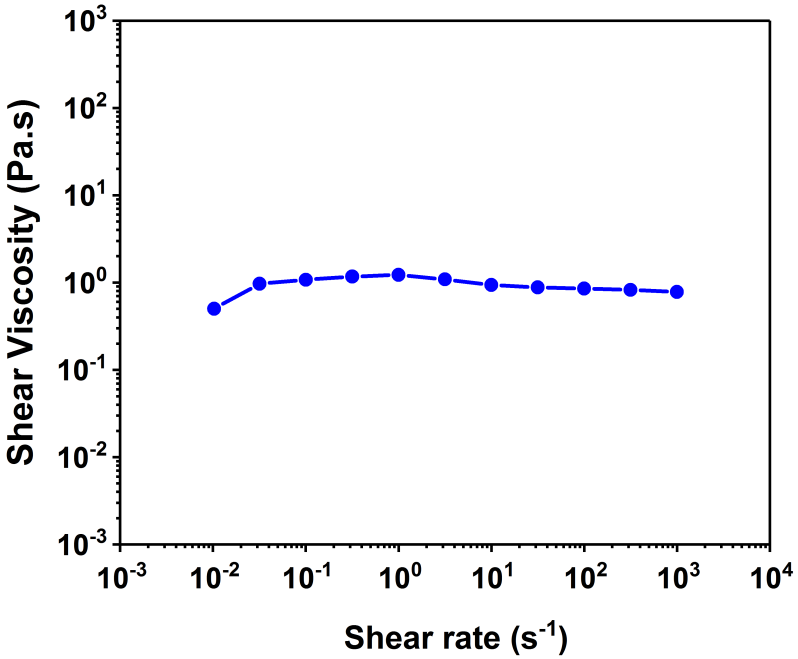

Figure 6.3: Viscosity versus shear rate of the standard oil to calibrate Rheo-EIS setup.

The next set of calibrations was electrical. It is important to evaluate the empty setup's impedance as a function of frequency. Open/short circuit calibration was performed by EIS measurements at voltage amplitude of 50 mV and at frequency range 0.01-10^5 Hz (Figure 6.4).

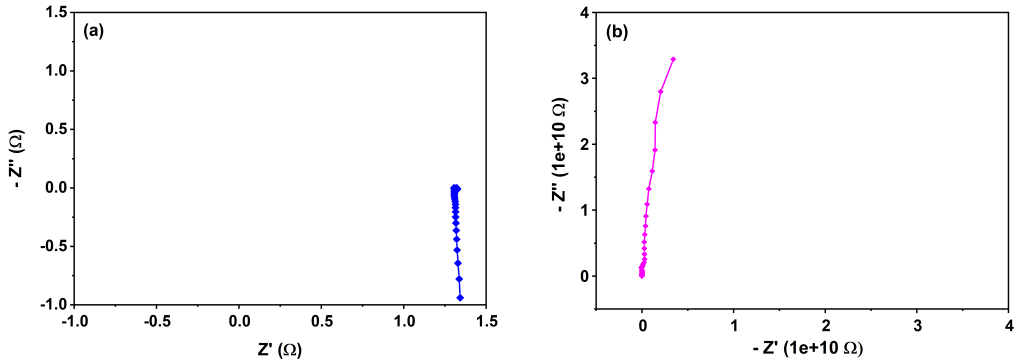

Figure 6.4: a) short circuit and b) open circuit impedance of the Rheo-EIS setup without any sample. Short circuit was measured by closing the gap and open circuit was measured at the working gap of 0.3 mm.

The sample impedance can be corrected with the setup's short and open circuit resistance, using equation 6.1 [168]. Where Z^*_M is the total system impedance including the

studied sample, Z_O^* and Z_S^* are the open and short circuit impedance, respectively. The idea is that the measured impedance is parallel with a resistor and in series with a capacitor, all applied from the instrument. The presented open circuit results in Figure 6.4b declare that the capacitance is too large to be considered in calibration. The setup resistance is also small, enabling more accurate receiving signals from sample impedance. The setup's open/short circuit impedance was measured at the beginning of each experiment.

equation

$$Z_{Corr}^* = \frac{(Z_M^* - Z_S^*)}{(1 - \frac{(Z_M^* - Z_S^*)}{Z_O^*})} \tag{6.1}$$

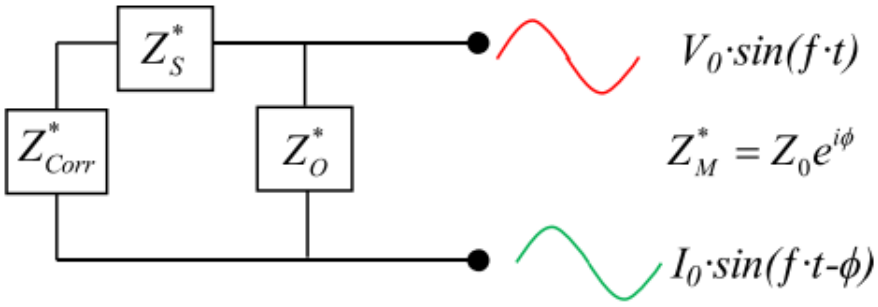

Figure 6.5: Equivalent circuit model for the open and short circuit resistances in a Rheo-Electric setup [168].

The AC voltage perturbation required for EIS measurements should be chosen from the sample's linear range of the I-V curve. Thus, linear sweep voltammetry was measured in the range of -0.2-0.2 V at a high (0.1 V/s) and low (0.01 v/s) scan rate. This measurement was performed with a catalyst ink sample loaded in the Rheo-EIS geometry and in the stationary mode. Considering the results shown in Figure 6.6, 50 mV was picked as the right AC voltage amplitude for the EIS measurements.

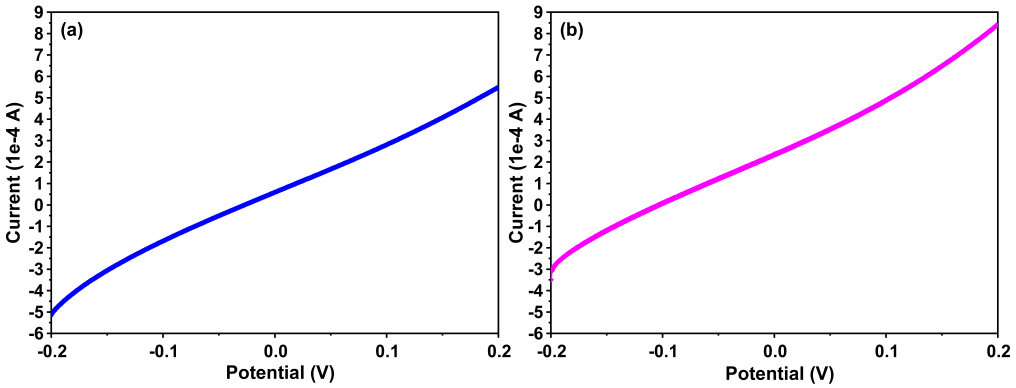

Figure 6.6: Linear sweep voltammetry of the catalyst ink loaded in the Rheo-EIS setup under stationary condition and at voltage scan rates of a) 0.1 V and b) 0.01 V.

It is well known that impedance increases with increasing electrode distance (in this case, geometry gap) [169]. To rule out effect of working gap on sample's impedance, EIS measurements were performed on a catalyst ink sample at various geometry gaps and in the stationary mode. Measurements were performed at gaps of 0.25, 0.30, 0.40, and 0.50 mm at voltage amplitude 50 mV and frequency range 0.01-10^5 Hz. From Figure 6.7, and the total resistances measured from the fitted equivalent circuit (Figure A.3), it is clear that impedance linearly increases with the gap. On the other, from the rheological standpoint, a gap ten times higher than the largest particle in the sample is appropriate for measurements [115]. Catalyst ink agglomerates are typically below 1 µm [170], so any gap larger than 0.25 mm is appropriate for the measurement. Our setup showed better torque-related stability at a gap of 0.3 mm. Therefore, for the rheo-EIS measurements working gap of 0.3mm was decided, which is large enough for the rheological measurements and small enough to reduce the impedance induced by the electrode distance.

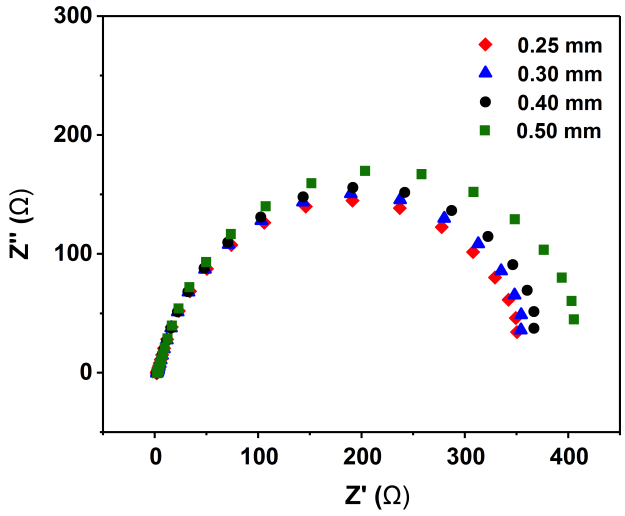

Figure 6.7: EIS measurements of a catalyst ink in the Rheo-EIS setup (stationary mode) at various electrode gaps of 0.25,0.3,0.4, and 0.5 mm. Measurements were taken at the voltage amplitude of 50 mV and frquency range of 0.01-10^5 Hz.

6.1.2.2 Rheo-Impedance parameters to evaluate catalyst ink microstructure

Two sets of Rheo-Impedance experiments were performed, a) simultaneous three-phase rebuilt and single frequency EIS measurements, and b) Full range EIS measurement before and after a high shear force resembling coating/processing condition on the ink. Prior to any rheological test, the ink was pre-sheared at 1 s^{-1} followed by 2 minutes resting to remove any prior shear history and give all samples a similar starting point. For the three-phase rebuilt measurements, the sample was held at shear rate 0.1 s^{-1} for 200s to provide pre-coating (storage) conditions for the ink. After that, shear rate was ramped up to 1000 s^{-1} (simulating high shear coating condition for the ink) and held there for 200s. Finally, shear rate was ramped back up to the 0.1 s^{-1} to simulate after coating condition for the ink (as a wet thin film). To allow microstructural to recover, measurements were taken at this condition for 720s. Parallel to all rheological measurements, single frequency (0.5 HZ) impedance test at a voltage amplitude 50 mV was carried out to record the overall resistivity of the sample under shear conditions. The dwell time of 200 s is needed to ensure the required stability for EIS measurements.

The second set of Rheological and electrical characterizations was sequential rather than simultaneous. A full frequency range EIS (f=0.01-10^5 Hz) at a voltage amplitude of 50 mV was measured in the stationary mode before further shearing the sample. Then, a pre-shear of 1000s^{-1} was applied for 200s, and EIS was measured after 2 minutes of rest. The result could give information on the microstructure percolation before and after applying processing shear forces. The electrical circuit shown in Figure 6.8 was used to fit the

EIS data. This equivalent circuit represents a parallel electronic (R_1) and ionic resistances (R_2) provided by carbon support agglomerate network and dissolved ions (e.g. H^+) in the solution respectively. The constant phase element (CPE,Q) is due to the capacitor effect of ion accumulation on the electrode (geometry) surface. The intermediate frequency region of the EIS impedance showed curve depression (45° region), indicating some properties of charge diffusion resistance on the electrode surface that could be fitted using a Warburg (w) element. However, explaining it requires advanced modeling [171] that is beyond the scope of this work and it will be shown not to be the main contributor to the overall impedance of the slurries. In general, it is expected that effect of I/C ratio and all interparticle interactions are reflected in the microstructure of Pt/C particles, which can be studied through its impact on the electrical resistance of the catalyst ink.

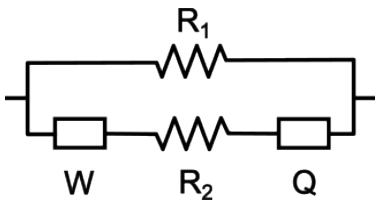

Figure 6.8: Equivalent circuit used to interpret EIS measurements of a catalyst ink in frequency range of 0.01-10^5 Hz and at voltage amplitude of 50 mV.

6.1.3 Cryogenic transmission electron microscopy

Catalyst ink samples with I/C=1 and 0.5 were diluted with IPA due to the transparent vitreous ice that can be achieved by IPA. This process can break down the large agglomerates in ink, but it cannot affect the primary aggregates due to their strong bonding[112]. Sample preparation was performed in Vitrobot. 3μL of the suspension was deposited on a carbon-coated copper grid (300 mesh, Tedpella) and turned into vitreous ice using liquid ethane in Vitrobot. The sample was stored in liquid nitrogen and transferred to the TEM (Talos F200C G2) for imaging at an operating voltage of 200 kV.

6.1.4 In-situ fuel cell characterization

A proper MEA should contain enough ionomer in the catalyst layer to transfer proton, so I/C ratios of 0 and 0.25 are not very practical for fuel cell characterizations. Studying these samples was necessary to unravel ionomer-Pt/C interaction by reducing/eliminating ionomer from ink. Hence, MEAs with I/C=0.5,0.75, and 1 proceeded to fuel cell testing. Toray TGP-H-060 with a microporous layer overcoat was used as the anode and cathode gas diffusion media. Catalyst electrochemical active surface area (ECSA, proton transfer resistance, oxygen transport resistance, and fuel cell performance were evaluated for the

designed MEAs with 2 cm^2 active area using an automated Greenlight G20 fuel cell test station. To evaluate ECSA, cyclic voltammetry was performed under H_2/N_2 flow and at the scan rate of 50 mV/s. Limiting current tests were performed under both dry (80°C, 64% RH) and wet conditions (70°C, 80% RH, 300 kPa). Under dry conditions, measurements were taken at cell pressures of 100, 150, 200, 300 kPa, and oxygen dry mole fraction varied between 1-4%. Fuel cell performance was assessed through polarization curves at T=70°C, RH= 64%, and pressure 100 kPa. To rule out membrane resistance or any contact resistance in the cell, high frequency impedance of the cell was measured via EIS using Gamry Reference 3000 with 30k Booster [159]. Relative humidity sweep test was employed to evaluate the current density generated by the cell at a low voltage of 0.3 V. RH was swept between 20-100%, with a potentiostatic hold of 13 minutes at each RH. Proton transfer resistance in membrane and cathode catalyst layer was evaluated through EIS measurement under H_2/N_2 flow at RH of 40, 70, and 100%. Details of the testing condition is provided in Table 6.1.

Table 6.1: Fuel cell test conditions for membrane electrode assemblies with cathode catalyst layers containing I/C=0.5, 0.75, and 1.

Test Name	Cell Temp. (°C)	Inlet RH (%)	Pressure (kPa abs.)	Flow rate (An/Ca) (NLPM)	Load Control (V)	Step scan rate/hold time
Cyclic Voltammetry	30	100	100	0.02/0.04	0.10 V to 1.20 V	50 mV/s
Break-in (16 cycles)	70	100	150	10/10 (Stoich)	OCV, 0.85, 0.70, 0.60, 0.40 V	Ca. 7 mins at each potential
Cell Performance Measurement	70	60	100	0.40/2.00	0.90 to 0.20 V	6 mins at each potential
RH Sweep	70	20, 40, 60, 80, 100	100	0.40/2.00	0.30 V	20 mins at each RH
Limiting Current	80	64	100, 150, 200, 300	0.40/2.00	0.30 to 0.09 V	2 mins at each potential
Sheet Resistance Measurement	70	40, 70, 100	300	0.10/0.10	0.20 V DC, 10 mV AC	EIS data every 10 mins

6.2 Rheological and electrochemical impedance study of the catalyst ink

6.2.1 Catalyst ink viscosity

Viscosity of the catalyst ink reveals its microstructure-driven flow resistance as a function of the applied shear force. Besides the microstructural information that can be extracted from a flow curve, the viscosity at high shear rates (e.g.$>$ 500 s$^-$1) is close to that of the ink under actual depositing shear forces, which forms a catalyst layer. Flow curve of catalyst inks with constant carbon/solvent ratio and various ionomer/carbon ratios is shown in Figure 6.9. Samples show the carbon-based inks' typical shear thinning behavior, with transient shear thickening at intermediate shear rates. At low shear rates (< 0.1 s^{-1}), most

samples show similar viscosity except for the I/C=1, which has the highest ionomer content in ink. Similar low shear viscosity of the samples indicates a major effect of carbon/solvent ratio on the catalyst ink flow behavior, which was kept constant in this study to limit the interactions to ionomer-Pt/C and ionomer-solvent. Low shear viscosity of the samples and shear thinning index (Chapter 4) are summarized in Table 6.2. Sample with I/C=1 had the lowest shear thinning index, indicating faster agglomerate breakdown in this sample. At low shear rates, shear thinning is due to the breakdown of large agglomerates connected with weak van der Waals forces. Thus, Pt/C agglomerates in the sample with I/C=1 might have weaker bonding due to the thicker ionomer coverage. As discussed in previous chapters (Chapters 4 and 5), the viscosity rise in intermediate shear rates is a result of the dominance of hydrodynamic forces and transient particle growth. The onset of this behavior is shown by arrows in Figure 6.9, and it is shifted toward lower shear rates by increasing the sample I/C ratio. Easier particle breakdown at low shear rates provides condition of an increase in particle volume at lower shear rates, so a smaller hydrodynamic force is required to push aggregates close to each other for hydro cluster formation [172, 173]. Finally, at high shear rates, where agglomerates are potentially broken down to the primary aggregates, the sample with I/C=0 ended up having the highest viscosity. Thus, carbon-carbon interaction in the absence of ionomer is much stronger. Ionomer seems to shield carbon-carbon interactions, resulting in a less percolated carbon network.

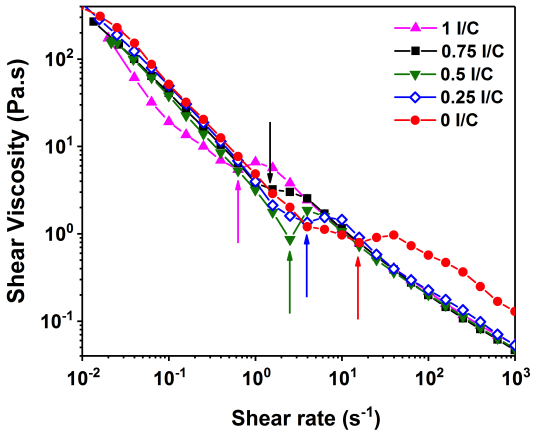

Figure 6.9: Viscosity versus shear rate of the catalyst inks with I/C=0, 0.25, 0.5, 0.75, and 1.

Table 6.2: Low shear viscosity and shear thinning index of catalyst inks with various Ionomer/Carbon ratios, reported values are calculated from shear rate 0.01-0.1 s^{-1}.

I/C ratio	Low shear viscosity @ 0.1 s^{-1} (Pa.s)	Shear thinning index (shear rate < 0.1 s^{-1})
0.00	51.41	0.126
0.25	49.55	0.078
0.50	37.95	0.053
0.75	40.78	0.056
1.00	19.16	-0.378

6.2.2 Simultaneous viscosity and electrochemical impedance evolution under coating condition

Catalyst layer fabrication from its precursor ink can involve three steps of applied shear forces. 1) Ink in the storage, considered low shear/stationary condition, 2) ink under high shear coating process and 3) back to the low shear/stationary condition during post coating recovery. To evaluate ink's microstructural evolution to form a thin film, three steps of low-high-low shear were applied to the catalyst ink in parallel with electrochemical impedance measurements. Figure 6.10a shows viscosity versus time under three-step shear condition, while Figure 6.10b contains information on the corresponding sample impedance with small AC perturbation at the frequency of 0.5 Hz. In the first step (low shear), viscosity of all samples is relatively close as was expected from previous viscometry results (Figure 6.9). However, sample impedance increases by increasing I/C ratio due to either ionomer coverage around agglomerates or presence of free ionomer in the ink [174]. By switching to high shear rates (second step), viscosity drops due to agglomerate break down to the primary aggregates and their alignment with the shear flow direction. On the other hand, impedance showed an overshoot in the onset of shear ramp up (6.10b, t=200s) due to the sudden interruption in the conductive paths [55]. This impedance rise remains constant or slightly decreases over time for samples with I/C=1 and 0.75. However, the impedance diminishes under high shear for samples with I/C $<$ 0.75. Over time, by breaking down more agglomerates and increasing total particle volume, interparticle distance decreases and results in lower impedance. However, this effect is less significant for samples with high ionomer content (I/C=1 and 0.75), confirming existence of thick ionomer coverage around aggregates, which disrupts conductivity.

In the third step, upon sudden shear rate ramp down to the initial value (first step), samples with I/C $<$ 0.75 experience an overshoot in the viscosity, indicating more elastic behavior due to the faster aggregation kinetics and low inter-particle repulsive forces [175] . In contrast, samples with I/C $\geq$ 0.75 showed more of a damping effect in response to the particle collision due to potentially higher repulsive forces from ionomer coverage. The

viscosity overshoot decreases over time due to particle interpenetration. Viscosity in the third stage is normalized by the average viscosity in the first stage to assess microstructure transformation in response to high shear force (Figure 6.11). It can be seen that samples with high ionomer content could not recover the microstructure due to the lower particle interaction, while samples with lower ionomer could not only recover the microstructure but also build a stronger one in the extreme case of I/C=0. This behavior indicates that by increasing ink's ionomer content, carbon-carbon attraction is more hindered by repulsive forces from ionomer coverage, and a less dense microstructure is formed after removal of shear force. This effect is verified by minimal change in the impedance of samples with I/C=0.75 and 1. On the other hand, samples with lower ionomer content benefited from carbon-carbon attraction, and after breaking down to smaller aggregates at high shear rates, particles could build a denser network resulting in lower impedance, as can be seen in Figure 6.10b.

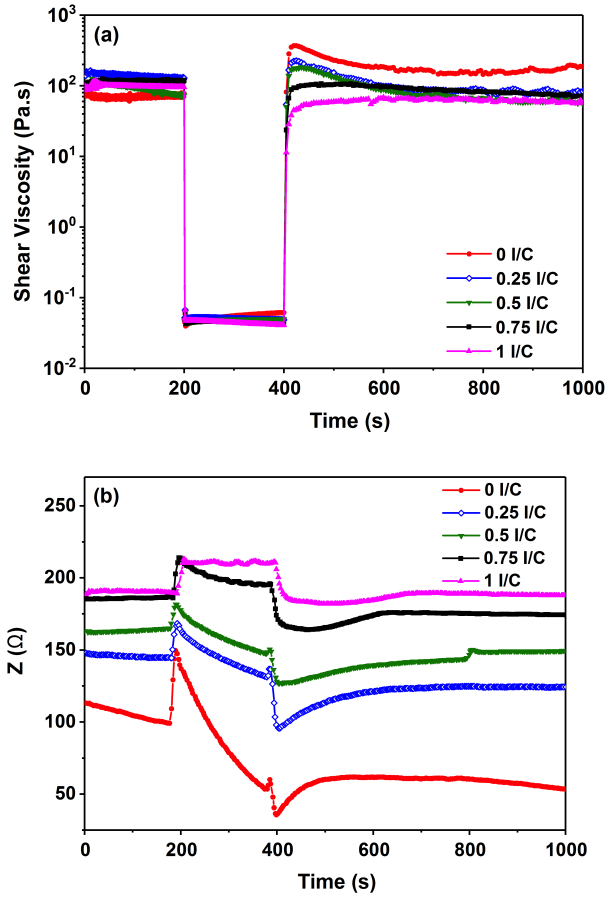

Figure 6.10: Simultaneous three phase rebuilt analysis and single frequency (0.5 Hz) EIS measurement of catalyst ink. Three steps of the applied shear rate were i) 0.1 s^{-1} for 200 s, ii)1000 s^{-1} for 200 s, and iii) 0.1 s^{-1} for 720 s.

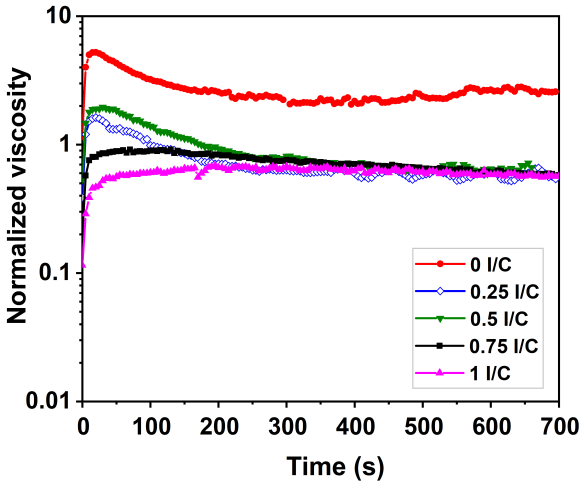

Figure 6.11: Catalyst ink viscosity at the recovery stage (post shear) normalized by its initial value (pre-shear). Plot is based on data presented in Figure 6.10.

6.2.3 Micorstructure impedance of catalyst ink before and after coating shear forces

Single frequency impedance cannot capture all the suspension's ionic and electronic resistance information. Thus, a full range frequency EIS measurement was performed on samples in the steady state condition before and after applying a high shear rate (Figure 6.12. Radius of the semicircle represents sample impedance, which is the smallest in the absence of ionomer (I/C=0). An equivalent circuit presented in Figure 6.8 was used to fit the EIS data. At high frequencies, the intercept of the EIS with the x-axis represents parallel ionic and electronic resistances in ink, while the low-frequency intercept shows the electronic resistance provided by the conductive carbon network in ink. The low-frequency (electronic) resistance in the equivalent circuit was found to be the major contributor to the impedance of catalyst inks. Sample electronic resistivity as a function of I/C ratio under both conditions of no applied shear force and after a pre-shear is shown in Figure 6.13. With increasing I/C ratio, the resistivity increases linearly up to I/C=0.75, and at higher values, it reaches a plateau. Thus, the agglomerated network gets weaker (loose gel) and consequently less conductive by increasing ionomer content. At a critical I/C (0.75), the thickness of the ionomer around Pt/C is large enough that adding more ionomer does not significantly affect the microstructure. Regarding post-shear EIS measurements, it can be seen that in samples with I/C $<$ 0.75, resistance significantly decreases after applying a high shear force to the ink. Resistance stays the same for I/C=0.75 and slightly increases for I/C=1, similar to the observations in the previous section. It can be inferred that I/C=0.75 is the highest value below which Pt/C could build up a percolated cohesive

network and above which ionomer coverage induces a repulsive force between particles and hinders formation of compact interconnected agglomerates. Thus, less dense and locally less conductive microstructure is expected for catalyst layers with I/C $\geq$ 0.75 in the formulation. Further, it is expected that sample with I/C=1 contains free ionomer aggregates that could participate in the overall high resistance of the ink [155].

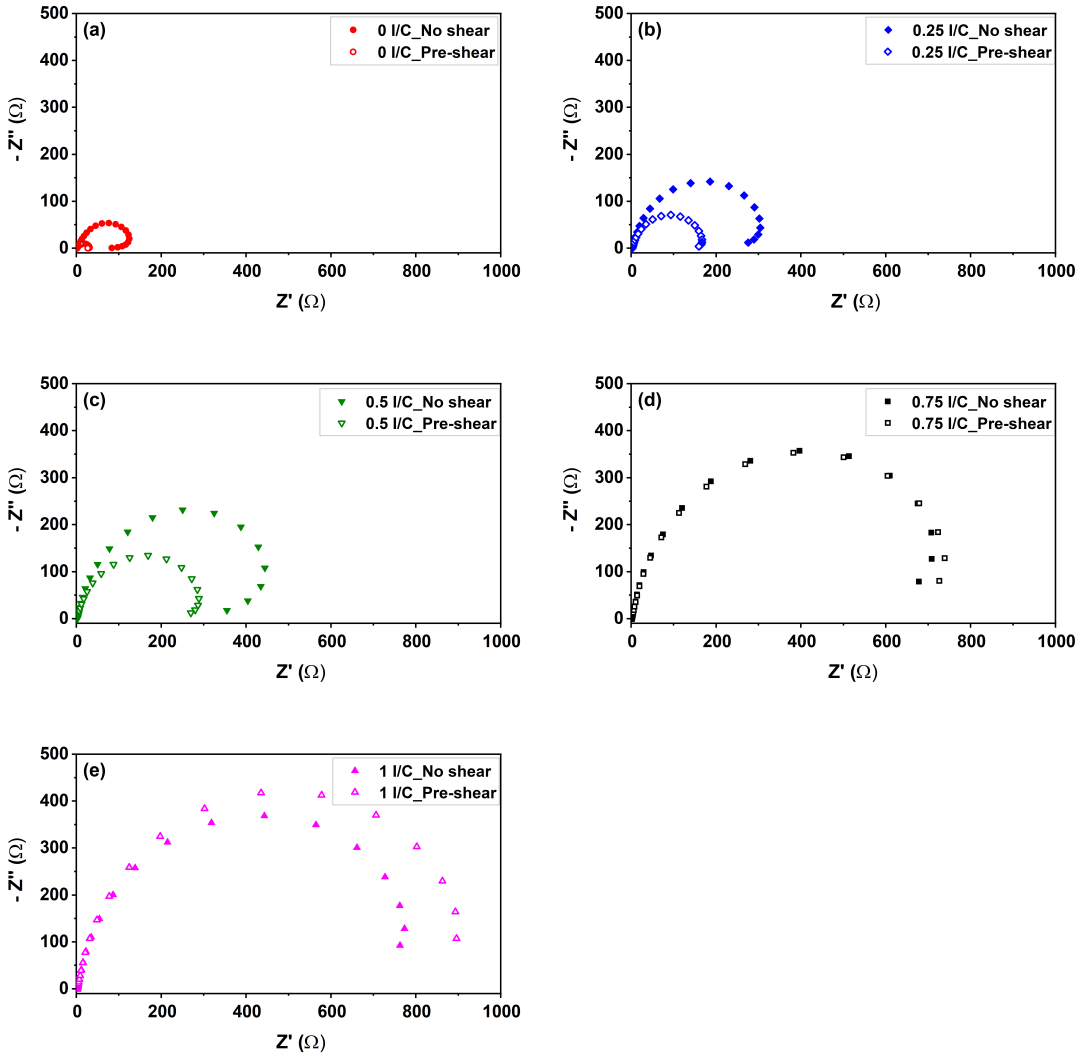

Figure 6.12: Full range (f=0.01-10^5 Hz) EIS measurement of the inks in the Rheo-EIS setup before and after applying pre-shear of 1000 s^{-1} for 200 s.

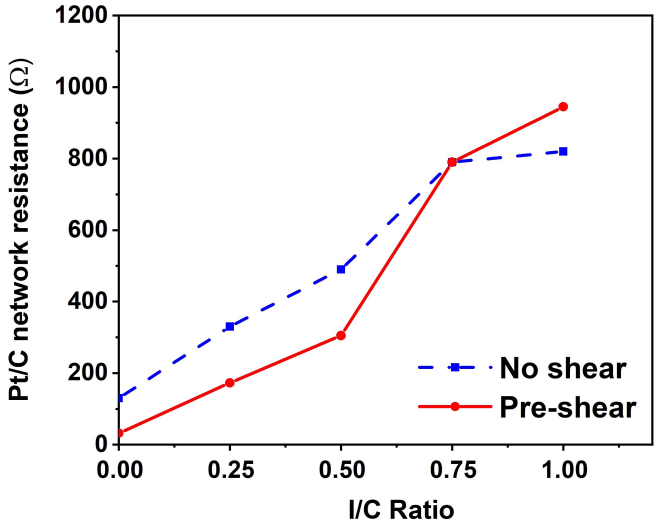

Figure 6.13: Electronic resistance of the Pt/C network measured from the fitted equivalent circuit on the EIS plots in Figure 6.12.

6.2.4 Electrochemical impedance and rheology of carbon ink

Equivalent carbon inks with no Platinum were prepared to further decouple inter-particle interactions in the catalyst ink. It is well known that Pt has more interaction with ionomer [57, 92, 176], so a major part of ionomer consumed in Pt-ionomer bonding. When a similar recipe of the catalyst ink was used in the preparation of pure carbon (Vulcan XC-72) ink, viscosity drastically dropped. This behavior confirms that a considerable amount of ionomer interacts with Pt, such that when Pt is removed, ionomer covers all carbon particles and impedes formation of interconnected microstructure. Thus sample flows like a Newtonian fluid at high shear rates [57] (Figure 6.14). Electrochemical impedance of the carbon ink with I/C=1 before and after employment of a high shear force is shown in Figure 6.15. Lack of a conductive carbon network in this ink caused a high impedance dominated by ionic conductivity, which is small in this sample. Thus a semicircle does not show in the Nyquist plot [173]. Still the equivalent circuit used for the catalyst ink sample can be used to fit the data, and the resulted electronic resistance was more than one order of magnitude higher than the corresponding catalyst ink. Another carbon ink made with I/C=0.5 showed the exact same viscosity and impedance plot suggesting the overall ionomer content of catalyst ink is high for a corresponding carbon ink. Further investigation of carbon inks required recipe adjustment, which was not an apple-to-apple comparison with the studied catalyst inks.

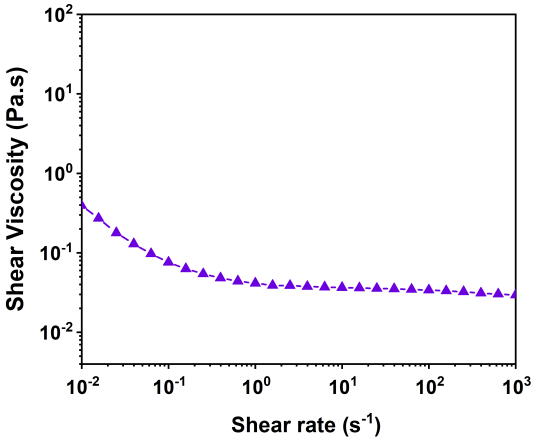

Figure 6.14: Viscosity versus shear rate for carbon ink with I/C=1.

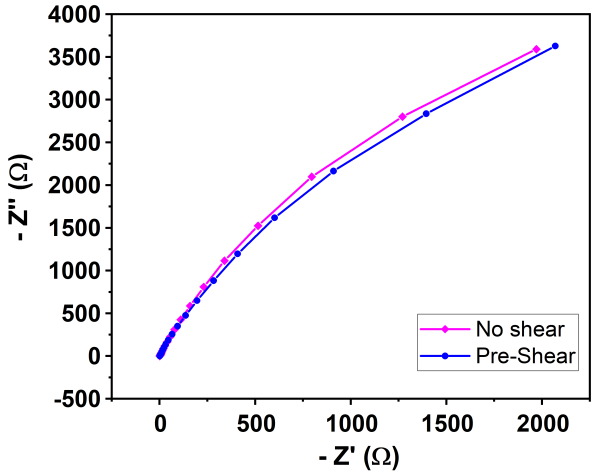

Figure 6.15: Carbon ink EIS measurement at voltage amplitude 50 mV and frequency range 0.01-10^5 Hz. measurements were taken before and after applying shear rate of 1000 s^{-1} for 200 s.

6.3 Cryogenic transmission electron microscopy of catalyst aggregates

Ink samples were diluted by IPA since this solvent is more appropriate for cryo-imaging and creates more transparent vitreous ice. Catalyst inks with I/C=0.5 and 1 were chosen as a viable lower and upper limit for a functional catalyst layer in the fuel cell. From Figure 6.16a, it can be seen that the sample with I/C=1 has an open fractal shape aggregate with a clear thick layer of ionomer coverage (marked on the figure). Rheological and electric resistivity of this sample suggested a loose structure, which can be expected from the expanded shape of the primary aggregates. On the other hand, primary aggregates of the sample with I/C=0.5 were found to be more spherical (Figure 6.16b) and compact.

This shape is due to the higher carbon-carbon interactions suggested by this sample's low resistivity and high microstructural strength in the Rheo-EIS results. Figure 6.17 provides more cryo-TEM images of the studied samples.

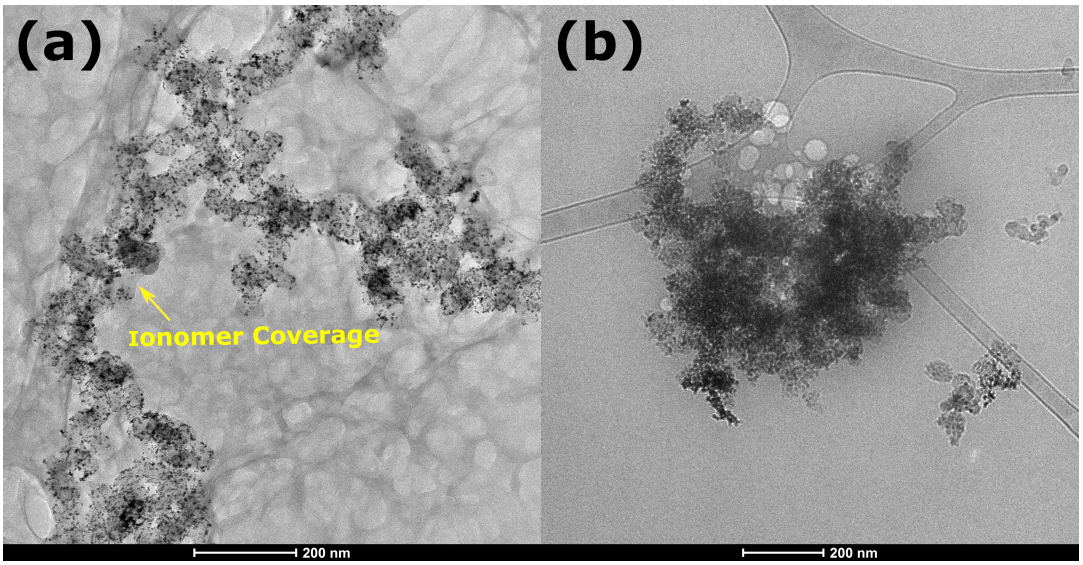

Figure 6.16: Cryo-TEM images of the diluted catalyst inks with a) I/C=1, and b) I/C=0.5.

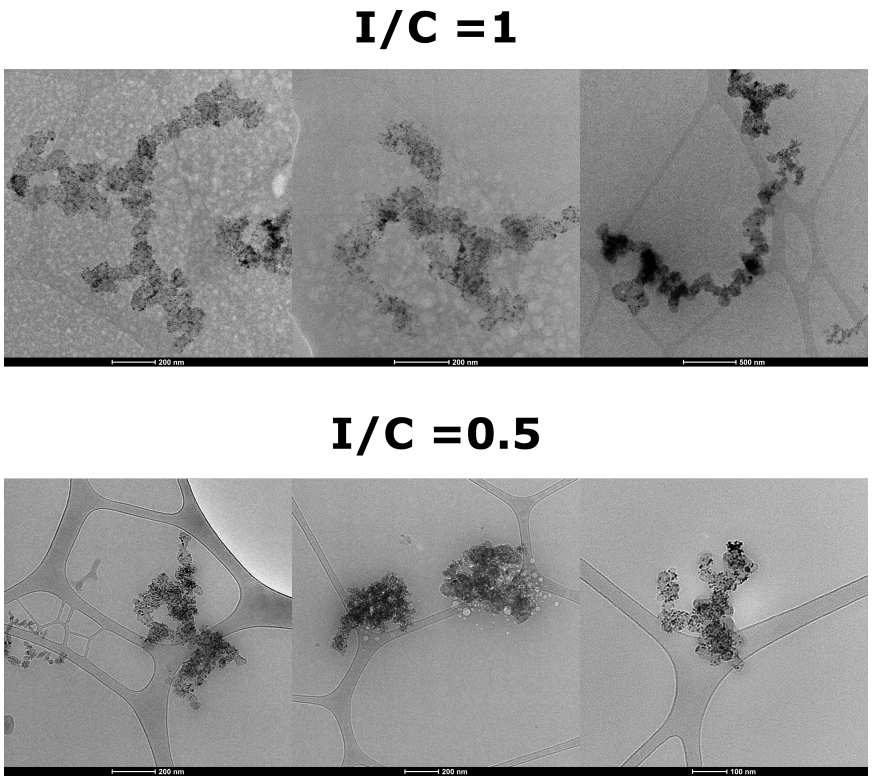

Figure 6.17: Additional Cryo-TEM images of the diluted catalyst inks (I/C ratio is marked for each group in the figure).

6.4 Characterization and performance of the catalyst layer

6.4.1 Oxygen transport resistance in the cell

Oxygen transport resistance (OTR) can be evaluated at the limiting current, which is the highest current density generated by a cell before it shuts down due to its high mass transport resistances. At high current density, maximum water generation occurs in the cell, which can block the pores in the catalyst layer and diffusion media, followed by limiting reactant supply to the catalyst. Hence, limiting current at various oxygen partial pressure with the assumption of zero reactant concentration in the cathode catalyst layer is being used as fundamental of the measurement(chapter3). Limiting current test under dry conditions provides information regarding the overall OTR of the porous electrode (catalyst layer) and diffusion media in the absence of liquid water. The porous media's total OTR, including both catalyst layer and diffusion media, is shown in Figure 6.18. The slope of this plot represents the Fickian diffusion (pressure dependent), which is diffusion in large pores of the diffusion media. The intercept with the Y-axis is related to Knudson diffusion in small pores of the microporous layer and catalyst layer. Since similar diffusion media is used for all samples, the Fickian diffusion, which is proportional to the ratio of nominal diffusivity to effective diffusivity, D/D_{eff} is about the same in all designed MEAs (Table 6.3). R_{others} in Table 6.3 represents the non-Fickian diffusion, which in this case can be attributed to the pores in the catalyst layer. The catalyst layers with I/C=0.5 and 0.75 have close R_{others}. However, R_{others} increased in the sample with I/C=1. The relatively thick ionomer in the sample with I/C=1 could cover Pt surface and hinder oxygen diffusion to its surface [109, 155, 177].

Table 6.3: Oxygen transport resistance under dry condition.

Cell cathode catalyst I/C ratio	D/D_{eff}	R_{others} (s/cm)
0.5	3.3	0.2486
0.75	3.23	0.2476
1	3.09	0.31

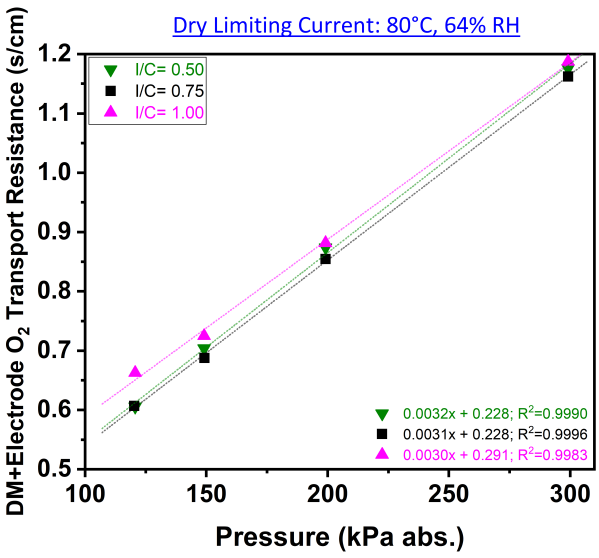

Figure 6.18: Diffusion media and electrode oxygen transport resistance as a function of pressure under dry condition (80°C, 64% RH) for the studied membrane electrode assemblies with various ionomer/carbon ratio in the cathode catalyst layer.

6.4.2 Fuel cell performance evaluation

The electrochemical active surface area (ECSA) in a catalyst layer can be assessed through cyclic voltammetry and calculation of the area under hydrogen adsorption/desorption peak. The ECSAs measured at 100%RH were 15.58, 17.55, and 19.46 m^2_{Pt}/g_{Pt}, for the catalyst layers with I/C=0.5, 0.75, and 1, respectively. The increase in ECSA with increasing catalyst layer's ionomer content has been attributed to sufficient proton conductive pathways due to high ionomer coverage [178]. Fuel cell performance is assessed via the I-V polarization curve as shown in Figure 6.19a. The voltage losses with the increase in current density are attributed to kinetic, ohmic, and mass transport barriers, respectively. The kinetic voltage loss is similar for all samples, as seen in the very low current densities. Ohmic losses from membrane ion transport and any interfacial resistances can be quantified by reading high-frequency resistance in the hybrid EIS measurement. The results are shown in the right Y-axis of the polarization curve (Figure 6.19a). HFR was found to be similar for all samples. However, in the intermediate current densities (dominated by ohmic loss), lower performance is achieved by the sample with I/C=0.5. Overall the sample with I/C=0.75, showed the highest performance followed by I/C=1 and 0.5. Similar ohmic region performance in samples with I/C=0.75 and 1 suggests a possible lack of proton conductive pathways in the sample with I/C=0.5. The lower high current density performance in the sample with I/C=1 is mainly in the mass transport region, which is aligned with its high oxygen transport resistance from limiting current data (Figure 6.18).

Due to the high impact of relative humidity on cell performance and increase in the mass transport resistances at high current density, RH sweep test at high current density (Voltage = 0.3 V) was performed (Figure 6.19b). At all relative humidities, performance of the sample with I/C=0.75 is superior followed by I/C=1 and 0.5.

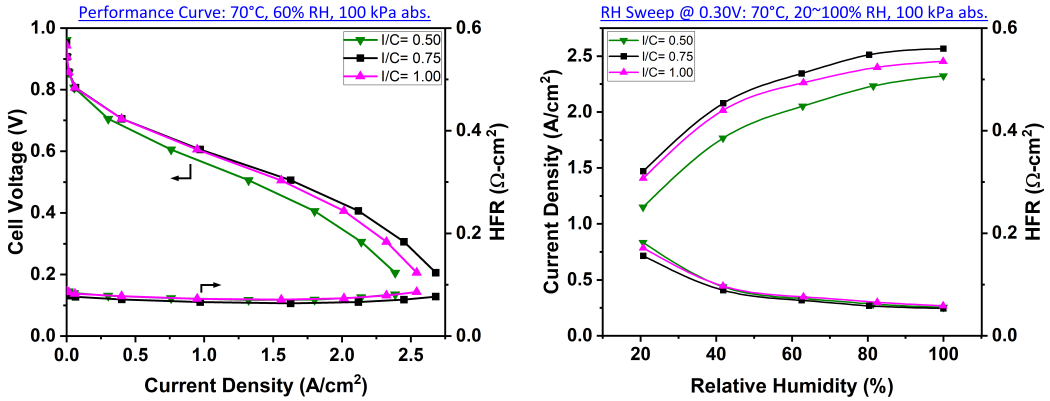

Figure 6.19: a) Steady-state polarization under dry condition (70°C, 64% RH, 100 kPa), and b) Current density versus relative humidity at 80°C, under 10-minutes potentiostatic hold at 0.30 V.

Proton transport resistance in the ionomer pathways of the catalyst layers can be evaluated through electrochemical impedance spectroscopy under H_2/N_2 flow at the anode/-cathode. The method is adapted to measure the ionomer transport resistance [179]. From proton resistivity data in Table 6.4, it can be seen that the sample with I/C=0.5 has the highest proton transport resistance due to the insufficient ionomer coverage on the catalyst. On the other hand sample with I/C=1 exhibits the lowest proton transport resistance, followed by the sample with I/C=0.75. Combination of minimum ionomer coverage required for effective proton transport and the increase in mass transport resistance due to a thick ionomer coverage suggests that the optimum amount of I/C is close to 0.75. This critical I/C was perfectly identified with the Rheo-EIS microstructural evaluation and endorsed by its superior fuel cell performance.

Table 6.4: Proton transport resistance in the cathode catalyst layer under 70°C, 70% RH, 300 kPa abs. at 0.20V DC and 10mV AC.

Catalyst layer I/C ratio	Proton resistivity ($m\Omega.cm^2$)	Corresponding high frequency resistance (HFR,($m\Omega.cm^2$))
0.5	109.23	53.68
0.75	42.63	48.79
1	31.62	53.1

6.5 Conclusion

Electrochemical reactions in PEMFC are limited to the locations in the catalyst layer where three pathways of electron conduction, proton conduction, and gas supply are provided (triple phase boundary). Carbon network, formed by the attraction between carbon support particles, provides electronic conductivity. Proton transport is feasible through ionomer coverage around platinum-carbon (Pt/C). Further, the required porous media for gas transport is formed upon assembly of the ionomer-covered Pt/C agglomerates. Therefore, interactions between Pt/C and ionomer can drastically affect triple phase boundary and even local mass transport resistances, eventually impacting fuel cell performance. Most of the ionomer-Pt/C interactions occur in catalyst ink processing, mainly the formulation. Ionomer to carbon ratio is well known as a key contributor to the interparticle interactions in ink. However, its optimum amount and its effect on the microstructure of the catalyst ink is still vague. In this work, for the first time, a new approach is introduced for microstructural analysis of catalyst ink from both a fluid mechanics point of view and electrochemical impedance in ink. Thus, combined rheological and mainly electronic resistance of the Pt/C agglomerate network was employed to study effect of I/C ratio on the microstructure of the catalyst ink. The standard parallel plate geometry of the rheometer was adapted to in-house rheo-EIS geometry, with electric isolation from the rheometer's body. The new setup successfully passed electric and rheologic calibration. First, viscosity of the catalyst ink was measured with the standard geometry, and it was found that the sample with I/C=1 had low viscosity at low shear rates, while the sample with I/C=0 showed the highest viscosity even at highs shear rates, suggesting a strong percolated microstructure. Simultaneous three-step viscometry with single frequency impedance was performed to assess microstructural evolution under applied shear forces from the coating process. In the absence of ionomer (I/C=0), the post-shear microstructure was even more entangled than the pre-shear one. On the other hand, by adding ionomer, it was found that microstructure cannot fully recover due to high shear force, and the magnitude of recovery decreases by increasing ink's I/C ratio. Hence, increasing ink's I/C ratio is expected to result in a looser carbon network. Simultaneous single frequency impedance measurements indicated a decrease in microstructure resistance in post-shear conditions, while this amount was less significant for samples with I/C$\geq$0.75. Full range impedance spectroscopy before and after applying high shear force was performed to further elucidate nature of the impedance in the microstructure. It was found that the electronic conductivity of the carbon network is the major contributor to the total impedance, and it can be used to assess the inter-connectivity of the ink microstructure, which can be interrupted by ionomer coverage. Electronic resistance of the ink increased significantly by increasing I/C ratio suggesting thicker ionomer coverage induces repulsive forces among

carbon. This answers the origin of lower post-shear recovery and the loose microstructure found in three-step shear tests. Impedance spectra taken in post shear condition were remarkably detected I/C=0.75 as the turning point were at values below this, the impedance decreases as a result of high shear force and break down of the agglomerates to smaller pieces. In contrast, impedance (mainly electronic resistance) increased in post-shear conditions for samples with I/C>0.75. This result greatly signals that the carbon network connection will significantly scarify at I/C> 0.75. Further cryo-TEM imaging of the samples with a low and high I/C ratio (0.5 and 1) revealed more open and expanded primary aggregates in the case of high ionomer content versus compact and spherical primary aggregates for low I/C. Thick ionomer coverage was detectable for I/C=1 in cryo-TEM. The inks formulated with I/C=0.5, 0.75, and 1 were fabricated as catalyst layers in the membrane electrode assembly (MEA) to evaluate their fuel cell performance and oxygen transport resistance. More significant oxygen transport resistance was found for the sample with I/C=1, while I/C=0.75 showed resistances close to I/C=0.5. This result was further validated by significant mass transport loss in performance of the sample with I/C=1 and superiority of the sample with I/C=0.75. The low limit of I/C=0.5 suffered from proton resistivity, contributing to its low performance. Thus, I/C =0.75 was found to be the optimum I/C ratio, which provides: a) proper ionomer coverage for low proton resistivity, b) allows sufficient carbon-carbon interaction for a network capable of electron conduction, and c) reduces local oxygen transport resistance induced by ionomer thickness around the catalyst.

Chapter 7

CONCLUSIONS AND FUTURE WORK

7.1 Conclusion

This study is divided into three main projects aiming to address various microstructure related challenges in the porous media of the proton exchange membrane fuel cell (PEMFC). The porous structure of the microporous layer (MPL) and catalyst layer is built upon assembly of carbon-based agglomerates in the precursor ink material. There is a lack of understanding of the effect of formulation and shear forces from coating process on the kinetics of agglomeration and its evolution during the process, which determines the final properties of the resulted porous media.

The first study investigates carbon network/ gel formation in the MPL as a function of two formulation variables and high shear forces from thin film deposition. The study aimed to correlate the carbon network's microstructure in ink to the properties of the casted thin film in the fuel cell and to propose the optimum amount of the formulation variables. MPL ink is composed of carbon black, PTFE, and a solvent. In this study, solid content and PTFE loading were the optimization targets. Rheology was employed as a tool to study the compactness of the carbon network within ink as a function of the shear forces applied during the coating process and formulation. Interactions between solid-liquid and solid-solid in ink determine kinetics of aggregation, agglomerate size, and percolation of the final network. Due to the discrepancy in the literature for an optimum formulation of the MPL ink, we chose a range of solid content and PTFE loading that could cover most of the studied inks in the literature. Further, this study bridged the gap between ink microstructure and the final porous structure of the MPL, as well as its performance and mass transport resistance in the fuel cell. As a result, MPL ink with solid content and PTFE loading of 10 and 25wt%, respectively, was proposed as the optimum composition resulting in a low oxygen transport resistance in the fuel cell by formation of permanent water pathways under high humidity conditions. This study contains a detailed rheological investigation of the carbonaceous slurries, which provides a foundation for our following projects and valuable information that can be used in other energy materials areas like flow batteries dealing with similar suspensions.

In the second project, we used the optimum MPL formulation found in the first project as a baseline and aimed to further enhance its mass transport properties. Thus, we introduced high aspect ratio carbonaceous additives to the typical carbon black-based MPL to introduce a gradient of large and small pores to the porous media to tailor its microstructure. The challenge was that the configuration of the carbon black agglomerates in the presence of these additives is unknown, and the amount of additive could drastically affect this configuration. On the other hand, among the two proposed additives, multi-wall carbon nanotube (MWCNT) and graphene nanoplatelet (GNP), the latter is less hydrophobic than the carbon black and could result in water accumulation in the cell. However, the hypothesis is based on the different pore geometry due to having larger particles in the composition. It is assumed that due to the low capillary force of the large pores, water could easily intrude there and leave the small hydrophobic pores, formed by the agglomerates of carbon black, free for gas transport. A range of additive content was used, and it was found that MWCNT is the most impactful additive in reducing oxygen transport resistance in the cell. Surprisingly both GNP and MWCNT at 20 wt% resulted in MPLs with lower oxygen transport resistance than the baseline and consequently higher fuel cell performance resistance. Additive amounts higher than 20 wt% revealed a compact microstructure, which had a feature of entangled bundles for MWCNT and compact stacks for the GNP. Overall, GNP particles are less hydrophobic than carbon black and tend to stack up, which forms a mass transport barrier. Hence the best additive which can introduce pore size diversity in the MPL is MWCNT, and the optimum amount is 20 wt%.

The third study is focused on the most complicated complex fluid and the resulted microstructure, which is participated in both mass transport and electrochemical reactions in the fuel cell. Membrane electrode assembly (MEA) is the core of the PEMFC, and it is composed of an anode and cathode catalyst layer with a proton conductive membrane in between. The precursor material of the catalyst thin films are slurries composed of carbon-supported catalyst (platinum, Pt), ionomer (proton conductive polymer), and a solvent. Due to the impact of ionomer on both microstructure of the catalyst layer, its proton conductivity, and local oxygen transport resistance, we invented a new method to study catalyst ink microstructure as a function of ionomer/carbon ratio (I/C) in ink. The new technique included both rheological and electrochemical impedance spectroscopy of the ink. Since ionomer is just proton conductive, its interaction with the electron conductive Pt/C network could successfully be captured in the impedance signal from the ink. The main impedance in ink was found to be electronic as a result of Pt/C- ionomer network. By increasing ionomer, conductivity of the ink was reduced and its microstructure could not recover after applying

processing shear forces. A thick ionomer coverage was found to hinder carbon-carbon attraction and result in the formation of a less interconnected and loose microstructure. It was found that the I/C ratio of 0.75 is the critical amount, below which the ionomer coverage may not be enough and above which it is too thick, causing local mass transport resistance.

7.2 Future work

The current study provided a foundation to systematically design optimized porous media in the fuel cell and study their mass transport properties. Due to the complex nature of catalyst ink, future studies will focus on understanding and optimizing its microstructure to reduce catalyst loading without scarifying performance. In terms of understanding interaction in the catalyst layer, several formulation factors are left to be studied with the Rheo-EIS technique.

1. Effect of carbon support on ionomer-catalyst interactions: A porous carbon support like high surface area carbon interacts differently with ionomer than solid spherical carbon support with all Platinum on its surface. Ionomer is relatively viscous and has large molecules, so it may not penetrate into the mesopores of a porous carbon substrate. This behavior defines a very different microstructure for the corresponding ink, which should reflect in both rheological and Rheo-EIS characterizations.

2. Effect of ink solvent on the interparticle and solid-liquid interactions in the ink: In our previous studies, we found a significant signal of microstructure difference between water reach and IPA reach catalyst inks. Ionomer conformation is a strong function of solvent composition, and EIS measurement can help understand its behavior in various dispersing media. This study can start with simple ionomer solvent solutions and expand to the catalyst ink.

3. Ionomer type: Short and long-side chain ionomers can interact differently with both solvent and Pt/C. The resulting ink can show different rheology and impedance, which can help to understand the nature of interactions in the ink and properties of the resulting catalyst layer. Nafion and Aquivion can be studied as two of the most common and acceptable ionomers in PEMFC industry.

All of the proposed ink studies will be coupled with in-situ fuel cell characterizations of the corresponding membrane electrode assembly (MEA) to better bridge the gap between catalyst ink properties and performance of the catalyst layer in MEA.

In order to optimize the catalyst layer microstructure, we intend to extend our findings from mass transport enhancement by introducing high aspect ratio additives to the porous

microstructure of the catalyst layer. Hence, small amounts of MWCNT will be added to the catalyst layer to improve its microstructure and reduce platinum loading. However, the interparticle interactions in the catalyst ink would become complicated, and we should first study ionomer-MWCNT interaction without any catalyst.

APPENDIX A

A.1 Rheo-Impedacne setup information

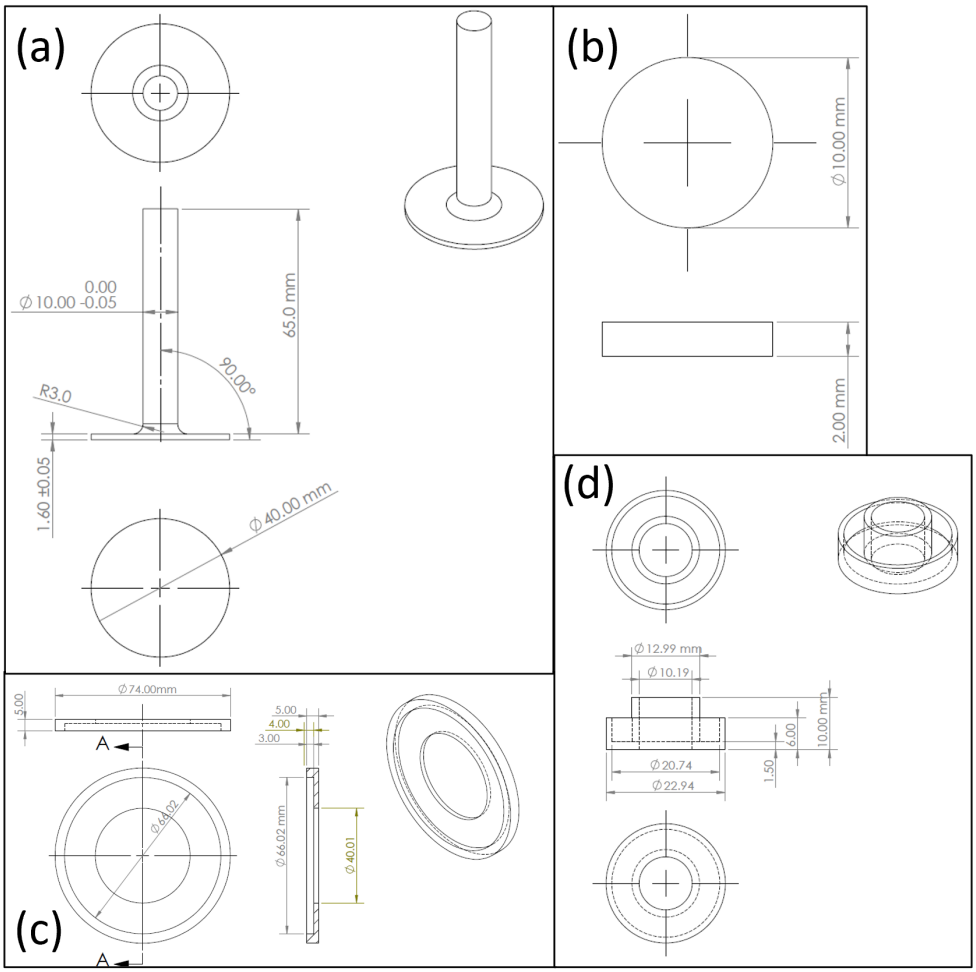

Figure A.1: Part layout for the machined and 3D printed parts of the Rheo-Impedance setp. a) stainless steel upper geometry, b)stainless steel lower plate, c)3D printed center guide used to install lower plate on the Peek geometry, and c) solvent trap installed on the upper geometry to be filled with liquid metal

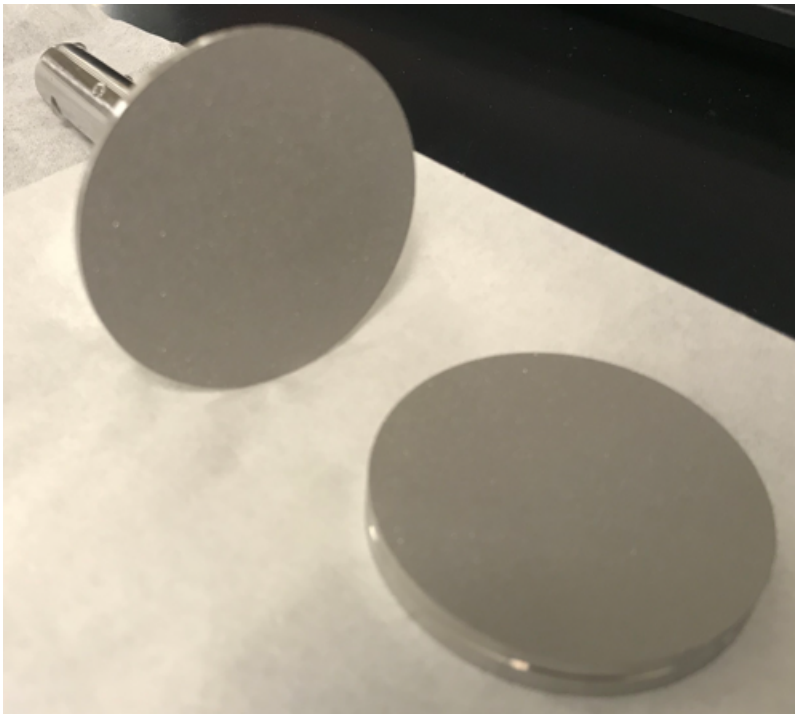

Figure A.2: Sand blasted upper and lower plate

A.2 Catalyst ink conductivity at various electrode gap in the Rheo-EIS setup

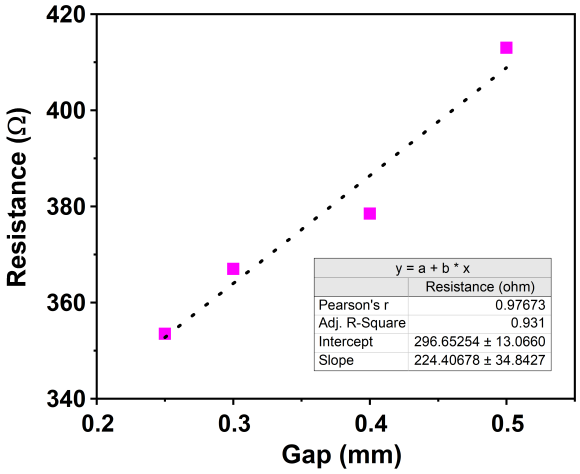

Figure A.3: Catalyst ink resistance measured from equivalent circuit fitted on Figure6.7 data.

Bibliography

[1] *Sources of Greenhouse Gas Emissions*. URL: https://www.epa.gov/ghgemissions/sources-greenhouse-gas-emissions.

[2] *DOE Projects Zero Emissions Medium- and Heavy-Duty Electric Trucks Will Be Cheaper than Diesel-Powered Trucks by 2035*. 2022. URL: https://www.energy.gov/articles/doe-projects-zero-emissions-medium-and-heavy-duty-electric-trucks-will-be-cheaper-diesel.

[3] Alin C Fărcaş and Petru Dobra. "Adaptive control of membrane conductivity of PEM fuel cell". In: *Procedia Technology* 12 (2014), pp. 42–49.

[4] Jon P Owejan et al. "Water management studies in PEM fuel cells, Part I: Fuel cell design and in situ water distributions". In: *International Journal of Hydrogen Energy* 34.8 (2009), pp. 3436–3444.

[5] Chunzhi He et al. "PEM fuel cell catalysts: Cost, performance, and durability". In: *The electrochemical society Interface* 14.3 (2005), p. 41.

[6] SJ Botelho and A Bazylak. "Impact of polymer electrolyte membrane fuel cell microporous layer nano-scale features on thermal conductance". In: *Journal of Power Sources* 280 (2015), pp. 173–181.

[7] Adnan Ozden et al. "A review of gas diffusion layers for proton exchange membrane fuel cells—With a focus on characteristics, characterization techniques, materials and designs". In: *Progress in Energy and Combustion Science* 74 (2019), pp. 50–102.

[8] Chang Sun Kong et al. "Influence of pore-size distribution of diffusion layer on mass-transport problems of proton exchange membrane fuel cells". In: *Journal of Power Sources* 108.1-2 (2002), pp. 185–191.

[9] MF Mathias et al. "Diffusion media materials and characterisation". In: *Handbook of fuel cells—fundamentals, technology and applications* 3.Part 1 (2003), pp. 517–537.

[10] Mehdi Andisheh-Tadbir, Francesco P Orfino, and Erik Kjeang. "Three-dimensional phase segregation of micro-porous layers for fuel cells by nano-scale X-ray computed tomography". In: *Journal of Power Sources* 310 (2016), pp. 61–69.

[11] Jeff T. Gostick et al. “On the role of the microporous layer in PEMFC operation”. In: *Electrochemistry Communications* 11.3 (2009), pp. 576–579.

[12] Zhigang Qi and Arthur Kaufman. “Improvement of water management by a microporous sublayer for PEM fuel cells”. In: *Journal of Power Sources* 109.1 (2002), pp. 38–46.

[13] Chung Jen Tseng and Shih Kun Lo. “Effects of microstructure characteristics of gas diffusion layer and microporous layer on the performance of PEMFC”. In: *Energy Conversion and Management* 51.4 (2010), pp. 677–684.

[14] Ugur Pasaogullari and Chao Yang Wang. “Two-phase transport and the role of microporous layer in polymer electrolyte fuel cells”. In: *Electrochimica Acta* 49.25 (2004), pp. 4359–4369.

[15] Dusan Spernjak, Ajay K. Prasad, and Suresh G. Advani. “Experimental investigation of liquid water formation and transport in a transparent single-serpentine PEM fuel cell”. In: *Journal of Power Sources* 170.2 (2007), pp. 334–344.

[16] Anthony Thomas et al. “Thermal and water transfer in PEMFCs: investigating the role of the microporous layer”. In: *International Journal of Hydrogen Energy* 39.6 (2014), pp. 2649–2658.

[17] Derek W. Fultz and Po Ya Abel Chuang. “The property and performance differences between catalyst coated membrane and catalyst coated diffusion media”. In: *Journal of Fuel Cell Science and Technology* 8.4 (2011), pp. 1–6.

[18] Adam Z Weber and John Newman. “Effects of microporous layers in polymer electrolyte fuel cells”. In: *Journal of the Electrochemical Society* 152.4 (2005), A677.

[19] Takumi Kusano et al. “Structural evolution of a catalyst ink for fuel cells during the drying process investigated by CV-SANS”. In: *Polymer journal* 47.8 (2015), pp. 546–555.

[20] E. H. Majlan et al. “Electrode for proton exchange membrane fuel cells: A review”. In: *Renewable and Sustainable Energy Reviews* 89.March (2018), pp. 117–134.

[21] D. Papageorgopoulos. *Fuel cell RD overview, DOE Hydrogen and Fuel Cells Program Annual Merit Review and Peer Evaluation Meeting, U.S. Department of Energy*. Tech. rep. 2019.

[22] Dustin Banham and Siyu Ye. “Current status and future development of catalyst materials and catalyst layers for proton exchange membrane fuel cells: an industrial perspective”. In: *ACS Energy Letters* 2.3 (2017), pp. 629–638.

[23] Neil J Vickers. "Animal communication: when i'm calling you, will you answer too?" In: *Current biology* 27.14 (2017), R713–R715.

[24] Jun Huang, Zhe Li, and Jianbo Zhang. "Review of characterization and modeling of polymer electrolyte fuel cell catalyst layer: The blessing and curse of ionomer". In: *Frontiers in Energy* 11.3 (2017), pp. 334–364.

[25] Kunal Karan. "PEFC catalyst layer: Recent advances in materials, microstructural characterization, and modeling". In: *Current Opinion in Electrochemistry* 5.1 (2017), pp. 27–35.

[26] Nada Zamel. "The catalyst layer and its dimensionality–A look into its ingredients and how to characterize their effects". In: *Journal of Power Sources* 309 (2016), pp. 141–159.

[27] Shinichi Takahashi et al. "Analysis of the Microstructure Formation Process and Its Influence on the Performance of Polymer Electrolyte Fuel-Cell Catalyst Layers". In: *ChemElectroChem* 2.10 (2015), pp. 1560–1567.

[28] Zhong Xie et al. "Fuel cell cathode catalyst layers from "green" catalyst inks". In: *Energy & Environmental Science* 1.1 (2008), pp. 184–193.

[29] Alin Orfanidi et al. "Ink solvent dependence of the ionomer distribution in the catalyst layer of a PEMFC". In: *Journal of The Electrochemical Society* 165.14 (2018), F1254.

[30] Jong-Hyeok Park, Mun-Sik Shin, and Jin-Soo Park. "Effect of dispersing solvents for ionomers on the performance and durability of catalyst layers in proton exchange membrane fuel cells". In: *Electrochimica Acta* 391 (2021), p. 138971.

[31] Chao Lei et al. "Impact of catalyst ink dispersing solvent on PEM fuel cell performance and durability". In: *Journal of The Electrochemical Society* 168.4 (2021), p. 044517.

[32] De-Chin Huang et al. "Effect of dispersion solvent in catalyst ink on proton exchange membrane fuel cell performance". In: *Int. J. Electrochem. Sci* 6.7 (2011), pp. 2551–2565.

[33] Ahmet Kusoglu and Adam Z Weber. "New insights into perfluorinated sulfonic-acid ionomers". In: *Chemical reviews* 117.3 (2017), pp. 987–1104.

[34] C Jeffrey Brinker and George W Scherer. *Sol-gel science: the physics and chemistry of sol-gel processing*. Academic press, 2013.

[35] Emanuela Zaccarelli. "Colloidal gels: equilibrium and non-equilibrium routes". In: *Journal of Physics: Condensed Matter* 19.32 (2007), p. 323101.

[36] Kourosh Malek et al. “Self-organization in catalyst layers of polymer electrolyte fuel cells”. In: *The Journal of Physical Chemistry C* 111.36 (2007), pp. 13627–13634.

[37] Jeffrey J Richards et al. “Clustering and percolation in suspensions of carbon black”. In: *Langmuir* 33.43 (2017), pp. 12260–12266.

[38] Jung-Shiun Jiang et al. “Percolation behaviors of model carbon black pastes”. In: *Soft Matter* 14.48 (2018), pp. 9786–9797.

[39] Larry L Hench and Jon K West. “The sol-gel process”. In: *Chemical reviews* 90.1 (1990), pp. 33–72.

[40] Kelsey B Hatzell et al. “Understanding inks for porous-electrode formation”. In: *Journal of Materials Chemistry A* 5.39 (2017), pp. 20527–20533.

[41] Donglei Yang. *Understanding the Formation-Structure-Functionality Relationship of the Catalyst Layer in a Proton Exchange Membrane Fuel Cell*. University of California, Merced, 2021.

[42] Sehkyu Park, Jong Won Lee, and Branko N. Popov. “A review of gas diffusion layer in PEM fuel cells: Materials and designs”. In: *International Journal of Hydrogen Energy* 37.7 (2012), pp. 5850–5865.

[43] L. R. Jordan et al. “Diffusion layer parameters influencing optimal fuel cell performance”. In: *Journal of Power Sources* 86.1 (2000), pp. 250–254.

[44] E. Antolini, R. R. Passos, and E. A. Ticianelli. “Effects of the carbon powder characteristics in the cathode gas diffusion layer on the performance of polymer electrolyte fuel cells”. In: *Journal of Power Sources* 109.2 (2002), pp. 477–482.

[45] Xiaoli Wang et al. “Micro-porous layer with composite carbon black for PEM fuel cells”. In: *Journal of Electrochimica Acta* 51 (2006), pp. 4909–4915.

[46] Orogbemi et al. “Through-plane gas permeability of gas diffusion layers and microporous layer: Effects of carbon loading and sintering”. In: *Journal of the Energy Institute* 91 (2017).

[47] Haolin Tang et al. “Porosity-graded micro-porous layers for polymer electrolyte membrane fuel cells”. In: *Journal of Power Sources* 166.1 (2007), pp. 41–46.

[48] Dusan Spernjak et al. “Enhanced Water Management of Polymer Electrolyte Fuel Cells with Additive-Containing Microporous Layers”. In: *ACS Applied Energy Materials* 1.11 (2018), pp. 6006–6017.

[49] Francois Lapicque et al. “A critical review on gas diffusion micro and macroporous layers degradations for improved membrane fuel cell durability”. In: *Journal of Power Sources* 336 (2016), pp. 40–53.

[50] M. Han, S. H. Chan, and S. P. Jiang. “Development of carbon-filled gas diffusion layer for polymer electrolyte fuel cells”. In: *Journal of Power Sources* 159.2 (2006), pp. 1005–1014.

[51] Sehkyu Park, Jong Won Lee, and Branko N. Popov. “Effect of PTFE content in microporous layer on water management in PEM fuel cells”. In: *Journal of Power Sources* 177.2 (2008), pp. 457–463. ISSN: 03787753.

[52] Reza Omrani and Bahman Shabani. “Gas diffusion layer modifications and treatments for improving the performance of proton exchange membrane fuel cells and electrolysers: A review”. In: *International Journal of Hydrogen Energy* 42.47 (2017), pp. 28515–28536.

[53] P. Antonacci et al. “Balancing mass transport resistance and membrane resistance when tailoring microporous layer thickness for polymer electrolyte membrane fuel cells operating at high current densities”. In: *Electrochimica Acta* 188 (Jan. 2016), pp. 888–897.

[54] Mohamed Youssry et al. “Aqueous dispersions of carbon black and its hybrid with carbon nanofibers”. In: *RSC Advances* 8.56 (2018), pp. 32119–32131.

[55] Aditya Narayanan, Frieder Mugele, and Michael H.G. Duits. “Mechanical History Dependence in Carbon Black Suspensions for Flow Batteries: A Rheo-Impedance Study”. In: *Langmuir* 33.7 (2017), pp. 1629–1638.

[56] Yuji Aoki. “Rheology of carbon black suspensions. IV. Effect of suspending media on the sol-gel transition behavior”. In: *Rheologica Acta* 50.9-10 (2011), pp. 779–785.

[57] Sunilkumar Khandavalli et al. “Rheological Investigation on the Microstructure of Fuel Cell Catalyst Inks”. In: *ACS Applied Materials and Interfaces* 10.50 (2018), pp. 43610–43622.

[58] Min Wang et al. “Impact of Catalyst Ink Dispersing Methodology on Fuel Cell Performance Using in-Situ X-ray Scattering”. In: *ACS Applied Energy Materials* 2.9 (2019), pp. 6417–6427.

[59] Paola Gallo Stampino et al. “Effect of different substrates, inks composition and rheology on coating deposition of microporous layer (MPL) for PEM-FCs”. In: *Catalysis Today* 147.SUPPL. (2009), pp. 30–35.

[60] Saverio Latorrata et al. “Novel superhydrophobic microporous layers for enhanced performance and efficient water management in PEM fuel cells”. In: *International Journal of Hydrogen Energy* 39.10 (2014), pp. 5350–5357.

[61] L. Cindrella et al. “Gas diffusion layer for proton exchange membrane fuel cells-A review”. In: *Journal of Power Sources* 194.1 (2009), pp. 146–160.

[62] Wei Mon Yan et al. “Optimal microporous layer for proton exchange membrane fuel cell”. In: *Journal of Power Sources* 195.17 (2010), pp. 5731–5734.

[63] Jeong Hwan Chun et al. “Development of a porosity-graded micro porous layer using thermal expandable graphite for proton exchange membrane fuel cells”. In: *Renewable Energy* 58 (2013), pp. 28–33.

[64] Wataru Yoshimune et al. “Managing the Pore Morphologies of Microporous Layers for Polymer Electrolyte Fuel Cells with a Solvent-Free Coating Technique”. In: *ACS Sustainable Chemistry Engineering* (2021).

[65] Rüdiger Schweiss et al. “Enhancement of proton exchange membrane fuel cell performance by doping microporous layers of gas diffusion layers with multiwall carbon nanotubes”. In: *Journal of Power Sources* (2012), pp. 79–83.

[66] J. Lee et al. “Multiwall Carbon Nanotube-Based Microporous Layers for Polymer Electrolyte Membrane Fuel Cells”. In: *Journal of The Electrochemical Society* 164.12 (2017), F1149–F1157.

[67] Gu Gon Park et al. “Adoption of nano-materials for the micro-layer in gas diffusion layers of PEMFCs”. In: *Journal of Power Sources* 163.1 SPEC. ISS. (2006), pp. 113–118.

[68] Amin Taheri Najafabadi et al. “Electrochemically Produced Graphene for Microporous Layers in Fuel Cells”. In: *ChemSusChem* 9.13 (2016), pp. 1689–1697.

[69] Jaeyeon Kim et al. “Carbon nanotube sheet as a microporous layer for proton exchange membrane fuel cells”. In: *Energy* 227 (2021), p. 120459.

[70] Saverio Latorrata et al. “Development of an optimal gas diffusion medium for polymer electrolyte membrane fuel cells and assessment of its degradation mechani”. In: *International Journal of Hydrogen Energy* 40.42 (2015), pp. 14596–14608.

[71] A. M. Kannan, P. Kanagala, and V. Veedu. “Development of carbon nanotubes based gas diffusion layers by in situ chemical vapor deposition process for proton exchange membrane fuel cells”. In: *Journal of Power Sources* 192.2 (2009), pp. 297–303.

[72] Arunachala M. Kannan and Lakshmi Munukutla. "Carbon nano-chain and carbon nano-fibers based gas diffusion layers for proton exchange membrane fuel cells". In: *Journal of Power Sources* 167.2 (2007), pp. 330–335.

[73] Rui Lin et al. "Detailed optimization of multiwall carbon nanotubes doped microporous layer in polymer electrolyte membrane fuel cells for enhanced performance". In: *Applied Energy* 274.June (2020), p. 115214.

[74] Tatsumi Kitahara, Hironori Nakajima, and Kosuke Okamura. "Gas diffusion layers coated with a microporous layer containing hydrophilic carbon nanotubes for performance enhancement of polymer electrolyte fuel cells under both low and high humidity conditions". In: *Journal of Power Sources* 283 (2015), pp. 115–124.

[75] T. Tanuma, M. Kawamoto, and S. Kinoshita. "Effect of Properties of Hydrophilic Microporous Layer (MPL) on PEFC Performance". In: *Journal of The Electrochemical Society* 164.6 (2017), F499–F503.

[76] Sanying Hou et al. "Enhanced performance of proton exchange membrane fuel cell by introducing nitrogen-doped CNTs in both catalyst layer and gas diffusion layer". In: *Electrochimica Acta* 253 (2017), pp. 142–150.

[77] M. J. Leeuwner, D. P. Wilkinson, and E. L. Gyenge. "Novel Graphene Foam Microporous Layers for PEM Fuel Cells: Interfacial Characteristics and Comparative Performance". In: *Fuel Cells* 15.6 (2015), pp. 790–801.

[78] Adnan Ozden et al. "Assessment of graphene as an alternative microporous layer material for proton exchange membrane fuel cells". In: *Fuel* 215.December 2017 (2018), pp. 726–734.

[79] Marco Mariani et al. "Characterization of novel graphene-based microporous layers for Polymer Electrolyte Membrane Fuel Cells operating under low humidity and high temperature". In: *International Journal of Hydrogen Energy* 45.11 (2020), pp. 7046–7058.

[80] M. Jeanette Leeuwner et al. "Graphene and reduced graphene oxide based microporous layers for high-performance proton-exchange membrane fuel cells under varied humidity operation". In: *Journal of Power Sources* 423.March (2019), pp. 192–202.

[81] Tatyana Soboleva et al. "On the micro-, meso-, and macroporous structures of polymer electrolyte membrane fuel cell catalyst layers". In: *ACS applied materials & interfaces* 2.2 (2010), pp. 375–384.

[82] Zhepeng Tang et al. “Recent progress in the use of electrochemical impedance spectroscopy for the measurement, monitoring, diagnosis and optimization of proton exchange membrane fuel cell performance”. In: *Journal of Power Sources* 468 (2020), p. 228361.

[83] Steven Holdcroft. “Fuel cell catalyst layers: a polymer science perspective”. In: *Chemistry of materials* 26.1 (2014), pp. 381–393.

[84] Jennifer Peron, Zhiqing Shi, and Steven Holdcroft. “Hydrocarbon proton conducting polymers for fuel cell catalyst layers”. In: *Energy & Environmental Science* 4.5 (2011), pp. 1575–1591.

[85] Haoran Yu et al. “Influence of the ionomer/carbon ratio for low-Pt loading catalyst layer prepared by reactive spray deposition technology”. In: *Journal of Power Sources* 283 (2015), pp. 84–94.

[86] Apichai Therdthianwong, Panuwat Ekdharmasuit, and Supaporn Therdthianwong. “Fabrication and performance of membrane electrode assembly prepared by a catalyst-coated membrane method: effect of solvents used in a catalyst ink mixture”. In: *Energy & fuels* 24.2 (2010), pp. 1191–1196.

[87] Rafael Nogueira Bonifácio et al. “Catalyst layer optimization by surface tension control during ink formulation of membrane electrode assemblies in proton exchange membrane fuel cell”. In: *Journal of Power Sources* 196.10 (2011), pp. 4680–4685.

[88] Yuqing Guo et al. “The controllable design of catalyst inks to enhance PEMFC performance: A review”. In: *Electrochemical Energy Reviews* 4.1 (2021), pp. 67–100.

[89] Xiao-Zi Yuan et al. “A review of functions, attributes, properties and measurements for the quality control of proton exchange membrane fuel cell components”. In: *Journal of Power Sources* 491 (2021), p. 229540.

[90] Rajkamal Balu et al. “Evolution of the interfacial structure of a catalyst ink with the quality of the dispersing solvent: a contrast variation small-angle and ultrasmall-angle neutron scattering investigation”. In: *ACS applied materials & interfaces* 11.10 (2019), pp. 9934–9946.

[91] Makoto Uchida et al. “New preparation method for polymer-electrolyte fuel cells”. In: *Journal of The Electrochemical Society* 142.2 (1995), p. 463.

[92] Fan Xu et al. “Investigation of a catalyst ink dispersion using both ultra-small-angle X-ray scattering and cryogenic TEM”. In: *Langmuir* 26.24 (2010), pp. 19199–19208.

[93] S-J Shin et al. “Effect of the catalytic ink preparation method on the performance of polymer electrolyte membrane fuel cells”. In: *Journal of power sources* 106.1-2 (2002), pp. 146–152.

[94] Kenji Kudo, Ryosuke Jinnouchi, and Yu Morimoto. “Humidity and temperature dependences of oxygen transport resistance of nafion thin film on platinum electrode”. In: *Electrochimica Acta* 209 (2016), pp. 682–690.

[95] P Aldebert et al. “Rod like micellar structures in perfluorinated ionomer solutions”. In: *Journal De Physique* 49.12 (1988), pp. 2101–2109.

[96] Pierre Aldebert, Bernard Dreyfus, and Michel Pineri. “Small-angle neutron scattering of perfluorosulfonated ionomers in solution”. In: *Macromolecules* 19.10 (1986), pp. 2651–2653.

[97] Jinfeng Wu et al. “Diagnostic tools in PEM fuel cell research: Part II: Physical/chemical methods”. In: *International Journal of Hydrogen Energy* 33.6 (2008), pp. 1747–1757.

[98] Tatyana Soboleva et al. “PEMFC catalyst layers: the role of micropores and mesopores on water sorption and fuel cell activity”. In: *ACS applied materials & interfaces* 3.6 (2011), pp. 1827–1837.

[99] Fan Yang et al. “Investigation of the interaction between nafion ionomer and surface functionalized carbon black using both ultrasmall angle X-ray scattering and cryo-TEM”. In: *ACS applied materials & interfaces* 9.7 (2017), pp. 6530–6538.

[100] Kourosh Malek and Marc-Olivier Coppens. “Knudsen self-and Fickian diffusion in rough nanoporous media”. In: *The Journal of chemical physics* 119.5 (2003), pp. 2801–2811.

[101] O Geier, S Vasenkov, and J Kärger. “Pulsed field gradient nuclear magnetic resonance study of long–range diffusion in beds of NaX zeolite: evidence for different apparent tortuosity factors in the Knudsen and bulk regimes”. In: *The Journal of chemical physics* 117.5 (2002), pp. 1935–1938.

[102] Tasleem Muzaffar, Thomas Kadyk, and Michael Eikerling. “Tipping water balance and the Pt loading effect in polymer electrolyte fuel cells: a model-based analysis”. In: *Sustainable Energy & Fuels* 2.6 (2018), pp. 1189–1196.

[103] Stanley J Normile et al. “Direct observations of liquid water formation at nano-and micro-scale in platinum group metal-free electrodes by operando X-ray computed tomography”. In: *Materials today energy* 9 (2018), pp. 187–197.

[104] Yu-Tong Mu et al. "Mesoscopic modeling of transport resistances in a polymer-electrolyte fuel-cell catalyst layer: analysis of hydrogen limiting currents". In: *Applied Energy* 255 (2019), p. 113895.

[105] Gen Inoue and Motoaki Kawase. "Understanding formation mechanism of heterogeneous porous structure of catalyst layer in polymer electrolyte fuel cell". In: *International Journal of Hydrogen Energy* 41.46 (2016), pp. 21352–21365.

[106] Ryosuke Jinnouchi et al. "Molecular dynamics simulations on O2 permeation through nafion ionomer on platinum surface". In: *Electrochimica Acta* 188 (2016), pp. 767–776.

[107] Md Azimur Rahman et al. "Development of 1-D multiphysics PEMFC model with dry limiting current experimental validation". In: *Electrochimica Acta* 320 (2019), p. 134601.

[108] Po-Ya Abel Chuang et al. "The interactive effect of heat and mass transport on water condensation in the gas diffusion layer of a proton exchange membrane fuel cell". In: *Journal of Power Sources* 480 (2020), p. 229121.

[109] Nobuaki Nonoyama et al. "Analysis of oxygen-transport diffusion resistance in proton-exchange-membrane fuel cells". In: *Journal of The Electrochemical Society* 158.4 (2011), B416.

[110] Linchao Zeng et al. "Integrated Paper-Based Flexible Li-Ion Batteries Made by a Rod Coating Method". In: *ACS Applied Materials and Interfaces* 11.50 (2019), pp. 46776–46782.

[111] Sourav Bhattacharjee. "DLS and zeta potential - What they are and what they are not?" In: *Journal of Controlled Release* 235 (2016), pp. 337–351.

[112] S. Shukla et al. "Experimental and Theoretical Analysis of Ink Dispersion Stability for Polymer Electrolyte Fuel Cell Applications". In: *Journal of The Electrochemical Society* 164.6 (2017), F600–F609.

[113] Shaojie Du et al. "Effects of ionomer and dispersion methods on rheological behavior of proton exchange membrane fuel cell catalyst layer ink". In: *International Journal of Hydrogen Energy* xxxx (2020).

[114] Ehsan Raee, Arezoo Avid, and Babak Kaffashi. "Effect of compatibilizer concentration on dynamic rheological behavior and morphology of thermoplastic starch/polypropylene blends". In: *Journal of Applied Polymer Science* 137.22 (2020), p. 48742. ISSN: 0021-8995.

[115] Tharwat F. Tadros. *Rheology of Dispersions: Principles and Applications*. 2010.

[116] F Mojica et al. "Experimental Study of Three Channel Designs with Model Comparison in a PEM Fuel Cell". In: *Fuel Cells* (2020). ISSN: 1615-6846.

[117] Mohammad Mahdi Barzegari et al. "Performance prediction and analysis of a dead-end PEMFC stack using data-driven dynamic model". In: *Energy* 188 (2019), p. 116049.

[118] Mirollah Hosseini et al. "Energy analysis of a proton exchange membrane fuel cell (PEMFC) with an open-ended anode using agglomerate model: A CFD study". In: *Energy* 188 (2019), p. 116090.

[119] Yeping Peng et al. "A transient heat and mass transfer CFD simulation for proton exchange membrane fuel cells (PEMFC) with a dead-ended anode channel". In: *International Communications in Heat and Mass Transfer* 115 (2020), p. 104638.

[120] Daniel R. Baker et al. "Measurement of Oxygen Transport Resistance in PEM Fuel Cells by Limiting Current Methods". In: *Journal of The Electrochemical Society* 156.9 (2009), B991.

[121] D. R. Baker and D. A. Caulk. "Limiting Current as a Tool to Study Oxygen Transport in PEM Fuel Cells". In: *ECS Transactions* 50.2 (2013), pp. 35–45.

[122] David A. Caulk and Daniel R. Baker. "Modeling Two-Phase Water Transport in Hydrophobic Diffusion Media for PEM Fuel Cells". In: *Journal of The Electrochemical Society* 158.4 (2011), B384.

[123] Vuk Uskoković. "Dynamic light scattering based microelectrophoresis: main prospects and limitations". In: *Journal of dispersion science and technology* 33.12 (2012), pp. 1762–1786.

[124] FuelCellStore. *Teflon™ PTFE DISP 30 Fluoropolymer Dispersion*. Cited 2021. URL: https://www.fuelcellstore.com/teflon-disp30.

[125] Ulf Nobbmann. "PDI from an individual peak in DLS". In: *Malvern Instruments* (2015), p. 1. URL: http://www.materials-talks.com/blog/2015/03/31/pdi-from-an-individual-peak-in-dls/.

[126] Mohamed Youssry et al. "Non-aqueous carbon black suspensions for lithium-based redox flow batteries: Rheology and simultaneous rheo-electrical behavior". In: *Physical Chemistry Chemical Physics* 15.34 (2013), pp. 14476–14486.

[127] Mohamed Youssry, Dominique Guyomard, and Bernard Lestriez. "Suspensions of carbon nanofibers in organic medium: Rheo-electrical properties". In: *Physical Chemistry Chemical Physics* 17.48 (2015), pp. 32316–32327.

[128] Masami Kawaguchi, Maki Okuno, and Tadaya Kato. "Rheological properties of carbon black suspensions in a silicone oil". In: *Langmuir* 17.20 (2001), pp. 6041–6044.

[129] Bilen Akuzum et al. "Percolation Characteristics of Conductive Additives for Capacitive Flowable (Semi-Solid) Electrodes". In: *ACS Applied Materials and Interfaces* 12.5 (2020), pp. 5866–5875.

[130] Jeffrey J. Richards et al. "Clustering and Percolation in Suspensions of Carbon Black". In: *Langmuir* 33.43 (2017), pp. 12260–12266.

[131] Sayantan Majumdar, Rema Krishnaswamy, and A. K. Sood. "Discontinuous shear thickening in confined dilute carbon nanotube suspensions". In: *Proceedings of the National Academy of Sciences of the United States of America* 108.22 (2011), pp. 8996–9001. DOI: 10.1073/pnas.1018685108.

[132] Shuangbing Li et al. "Giant Rheological Effect of Shear Thickening Suspension Comprising Silica Nanoparticles with No Aggregation". In: *Journal of Materials Science and Technology* 33.3 (2017), pp. 261–265.

[133] Paul F. Luckham and Michael A. Ukeje. "Effect of particle size distribution on the rheology of dispersed systems". In: *Journal of Colloid and Interface Science* 220.2 (1999), pp. 347–356.

[134] Brian R Solomon et al. "Enhancing the Performance of Viscous Electrode-Based Flow Batteries Using Lubricant-Impregnated Surfaces". In: *ACS Applied Energy Materials* 1.8 (Aug. 2018), pp. 3614–3621.

[135] Adrian Hill and Steve Carrington. "Understanding the links between rheology and particle parameters". In: *American Laboratory* 38.21 (2006), p. 22.

[136] Xiaofei Sha et al. "Shear thickening behavior of nanoparticle suspensions with carbon nanofillers". In: *Journal of Nanoparticle Research* 15.7 (2013).

[137] C. L. Barrie et al. "Rheology of aqueous carbon black dispersions". In: *Journal of Colloid and Interface Science* 272.1 (2004), pp. 210–217.

[138] Christopher W Macosko. "Rheology Principles". In: *Measurements and Applications* (1994).

[139] Lixin Liu et al. “Highly conductive graphene/carbon black screen printing inks for flexible electronics”. In: *Journal of Colloid and Interface Science* 582 (2021), pp. 12–21.

[140] Guillaume Ovarlez et al. “Rheopexy and tunable yield stress of carbon black suspensions”. In: *Soft Matter* 9.23 (2013), pp. 5540–5549.

[141] Chinedum O. Osuji, Chanjoong Kim, and David A. Weitz. “Shear thickening and scaling of the elastic modulus in a fractal colloidal system with attractive interactions”. In: *Physical Review E - Statistical, Nonlinear, and Soft Matter Physics* 77.6 (2008), pp. 8–11.

[142] Ajay Singh Negi and Chinedum O. Osuji. “New insights on fumed colloidal rheology - Shear thickening and vorticity-aligned structures in flocculating dispersions”. In: *Rheologica Acta* 48.8 (2009), pp. 871–881.

[143] Marm B. Dixit et al. “Catalyst Layer Ink Interactions That Affect Coatability”. In: *Journal of The Electrochemical Society* 165.5 (2018), F264–F271.

[144] Raven Fournier et al. “Combined Infrared Thermography, X-ray Radiography, and Computed Tomography for Ink Drying Studies”. In: *ACS Applied Energy Materials* 1.11 (2018), pp. 6101–6114.

[145] Naomi Kumano. “Controlling cracking formation in fuel cell catalyst layers Naomi”. In: (2020).

[146] Jin Young Kim et al. “Crack formation and prevention in colloidal drops”. In: *Scientific Reports* 5 (2015), pp. 1–9.

[147] Monica Schneider et al. “Suppressing Crack Formation in Particulate Systems by Utilizing Capillary Forces”. In: *ACS Applied Materials and Interfaces* 9.12 (2017), pp. 11095–11105.

[148] Jeong Hwan Chun et al. “Improvement of the mechanical durability of micro porous layer in a proton exchange membrane fuel cell by elimination of surface cracks”. In: *Renewable Energy* 48 (2012), pp. 35–41.

[149] Hiroshi Ito et al. “Application of a self-supporting microporous layer to gas diffusion layers of proton exchange membrane fuel cells”. In: *Journal of Power Sources* 342 (2017), pp. 393–404.

[150] Min Wang et al. “Impact of Microporous Layer Roughness on Gas-Diffusion-Electrode-Based Polymer Electrolyte Membrane Fuel Cell Performance”. In: *ACS Applied Energy Materials* 2.11 (2019), pp. 7757–7761.

[151] F. E. Hizir et al. “Characterization of interfacial morphology in polymer electrolyte fuel cells: Micro-porous layer and catalyst layer surfaces”. In: *Journal of Power Sources* 195.11 (2010), pp. 3463–3471.

[152] Daniel R. Baker et al. “The Use of Limiting Current to Determine Transport Resistance in PEM Fuel Cells”. In: *ECS Transactions* 3.1 (2019), pp. 989–999.

[153] Shirin Mehrazi et al. “A rheological approach to studying process-induced structural evolution of the microporous layer in a proton exchange membrane fuel cell”. In: *Electrochimica Acta* (2021), p. 138690.

[154] Guangfu Li et al. “New insights into evaluating catalyst activity and stability for oxygen evolution reactions in alkaline media”. In: *Sustainable Energy & Fuels* 2.1 (2018), pp. 237–251.

[155] Hong Ren et al. “Ionomer network of catalyst layers for proton exchange membrane fuel cell”. In: *Journal of Power Sources* 506.June (2021), p. 230186.

[156] Vuk Uskoković. “Dynamic Light Scattering Based Microelectrophoresis: Main Prospects and Limitations”. In: *Journal of Dispersion Science and Technology* 33.12 (2012), pp. 1762–1786.

[157] Malvern Instruments. “Zeta potential: An Introduction in 30 minutes, Zetasizer Nano Serles Technical Note”. In: *MRK654-01* 1 (2011), p. 8.

[158] Felipe Mojica et al. “Study of converging-diverging channel induced convective mass transport in a proton exchange membrane fuel cell”. In: *Energy Conversion and Management* 237 (2021), p. 114095.

[159] Dietmar Gerteisen et al. “Effect of operating conditions on current density distribution and high frequency resistance in a segmented PEM fuel cell”. In: *international journal of hydrogen energy* 37.9 (2012), pp. 7736–7744.

[160] David A. Caulk and Daniel R. Baker. “Heat and Water Transport in Hydrophobic Diffusion Media of PEM Fuel Cells”. In: *Journal of The Electrochemical Society* 157.8 (2010), B1237.

[161] Mahla Zabet et al. “Anisotropic Nanoparticles Contributing to Shear-Thickening Behavior of Fumed Silica Suspensions”. In: *ACS Omega* 2.12 (2017), pp. 8877–8887.

[162] Sheng Yan Lin and Min Hsing Chang. “ffect of microporous layer composed of carbon nanotube and acetylene black on polymer electrolyte membrane fuel cell performance”. In: *International Journal of Hydrogen Energy* 40.24 (2015), pp. 7879–7885.

[163] Vivekanand V Gobre and Alexandre Tkatchenko. "Scaling laws for van der Waals interactions in nanostructured materials". In: *Nature communications* 4.1 (2013), pp. 1–6. ISSN: 2041-1723.

[164] J. Lee et al. "Microporous layer to carbon fibre substrate interface impact on polymer electrolyte membrane fuel cell performance". In: *Journal of Power Sources* 422.November 2018 (2019), pp. 113–121.

[165] Christoph Simon, Frédéric Hasché, and Hubert A. Gasteiger. "Influence of the Gas Diffusion Layer Compression on the Oxygen Transport in PEM Fuel Cells at High Water Saturation Levels". In: *Journal of The Electrochemical Society* 164.6 (2017), F591–F599.

[166] Tushar Swamy, E. C. Kumbur, and M. M. Mench. "Characterization of Interfacial Structure in PEFCs: Water Storage and Contact Resistance Model". In: *Journal of The Electrochemical Society* 157.1 (2010), B77.

[167] Ahmed Helal, Thibaut Divoux, and Gareth H McKinley. "Simultaneous rheoelectric measurements of strongly conductive complex fluids". In: *Physical Review Applied* 6.6 (2016), p. 064004.

[168] Jeffrey J Richards, Norman J Wagner, and Paul D Butler. "A strain-controlled RheoSANS instrument for the measurement of the microstructural, electrical, and mechanical properties of soft materials". In: *Review of Scientific Instruments* 88.10 (2017), p. 105115.

[169] Nikolaus Doppelhammer et al. "Moving Electrode Impedance Spectroscopy for Accurate Conductivity Measurements of Corrosive Ionic Media". In: *ACS sensors* 5.11 (2020), pp. 3392–3397.

[170] Daozeng Yang et al. "Control of Cluster Structures in Catalyst Inks by a Dispersion Medium". In: *ACS omega* 6.48 (2021), pp. 32960–32969.

[171] Tyler J Petek et al. "Characterizing slurry electrodes using electrochemical impedance spectroscopy". In: *Journal of The Electrochemical Society* 163.1 (2015), A5001.

[172] Alessandro Brilloni et al. "Improving the electrical percolating network of carbonaceous slurries by superconcentrated electrolytes: an electrochemical impedance spectroscopy study". In: *ACS applied materials & interfaces* 13.11 (2021), pp. 13872–13882.

[173] Mentallah Meslam, Ahmed A Elzatahry, and Mohamed Youssry. "Promising aqueous dispersions of carbon black for semisolid flow battery application". In: *Colloids and Surfaces A: Physicochemical and Engineering Aspects* (2022), p. 129376.

[174] Hong Ren et al. “Ionomer network of catalyst layers for proton exchange membrane fuel cell”. In: *Journal of Power Sources* 506 (2021), p. 230186.

[175] Hooin Lee and Sangkyun Koo. “Analysis of fractal aggregates in a colloidal suspension of carbon black from its sedimentation and viscosity behavior”. In: *Korea-Australia Rheology Journal* 28.4 (2016), pp. 267–273.

[176] Shinichi Takahashi et al. “Observation of ionomer in catalyst ink of polymer electrolyte fuel cell using cryogenic transmission electron microscopy”. In: *Electrochimica Acta* 224 (2017), pp. 178–185.

[177] Atsushi Ohma, Kazuyoshi Fushinobu, and Ken Okazaki. “Influence of Nafion® film on oxygen reduction reaction and hydrogen peroxide formation on Pt electrode for proton exchange membrane fuel cell”. In: *Electrochimica Acta* 55.28 (2010), pp. 8829–8838.

[178] Katsuyoshi Kakinuma et al. “Evaluation of ionomer distribution on electrocatalysts for polymer electrolyte fuel cells by use of a low acceleration voltage scanning electron microscope”. In: *Journal of The Electrochemical Society* 168.5 (2021), p. 054510.

[179] Ruichun Jiang, Cortney K Mittelsteadt, and Craig S Gittleman. “Through-plane proton transport resistance of membrane and ohmic resistance distribution in fuel cells”. In: *Journal of the Electrochemical Society* 156.12 (2009), B1440.